POLITECNICO DI MILANO

Facoltà di Ingegneria Industriale e dell'Informazione

Corso di Laurea Magistrale in
Ingegneria Aeronautica

Optimal feedback control of plane channel flow over porous walls

Relatore: Prof. Maurizio QUADRIO

Co-relatore: Prof. Luca CORTELEZZI

Tesi di Laurea di:

Luca CIRROTTOLA Matr. 782839

Anno Accademico 2012 - 2013

Lo scrittore racconta la sua storia,
(ha solo senso
quando un altro legge)

e impareremo da una sua memoria
ch'egli forse
perde.

Lui sopporta
la nostra disistima:

coraggioso a commuoversi e spogliarsi
dirige le sue orchestre
e lascia in pasto quel suo io egoistico.

E un giorno dalla prosa:
in un "rumore bianco" che somiglia
a un passare di lente baleniere

salirà un filo puro,
detto poesia,
da quel suo golfo mistico.

- Ignoto -

Abstract

Optimal control of plane channel flow, aiming at reducing skin friction or increasing flow rate with a net power saving, is usually studied assuming a continuous distribution of zero-net-flux blowing-suction actuators at walls. This work investigates the macroscopic effects of the wall-distributed actuator pores on the controller synthesis by modeling solid walls as rigid layers of homogeneous porous materials. Porous regions are described by the Volume Averaged Navier-Stokes equations, while the coupling between flow in the channel and porous regions is modeled by the Ochoa-Tapia interface conditions.

A multidomain spectral discretization is specifically studied to numerically approximate the linearized dynamical system without the occurrence of any spurious eigenvalue which could spoil the dynamical analysis.

An *optimize-then-discretize* approach is used to overcome the additional mathematical difficulties caused by the flow coupling through the interfaces.

In order to compute the Linear Quadratic Regulator (LQR) gains to be applied in the nonlinear Direct Numerical Simulation (DNS) of the coupled flow system, the minimum energy controller design technique introduced by Bewley, Pralits and Luchini has been extended to the continuous adjoint approach. The Adjoint of the Direct-Adjoint (ADA) technique has been used to evaluate the feedback gains for higher degrees of controller authority.

Results show that the actuator modeling could affect the robustness properties of LQRs for plane channel flow when applied in a real control setup.

Key words

Linear Quadratic Regulator - Volume Averaged Navier-Stokes Equations - Multidomain spectral methods - Continuous adjoint - Differential-Algebraic Equations

Sommario

Il controllo ottimo della corrente in un canale piano, finalizzato alla riduzione della resistenza d'attrito o all'incremento della portata con un risparmio netto di potenza, è generalmente studiato assumendo una distribuzione continua di getti sintetici (a portata netta nulla) sulle pareti. Questo lavoro studia gli effetti macroscopici indotti dalla distribuzione di pori degli attuatori a parete modellando le pareti rigide come strati di materiale poroso omogeneo. Le regioni porose sono descritte dalle equazioni di Navier-Stokes mediate nel volume (Volume Averaged Navier-Stokes equations - VANS), e l'accoppiamento tra le correnti nel canale e nelle regioni porose è modellato attraverso le condizioni di interfaccia di Ochoa-Tapia.

Una discretizzazione spettrale multidominio è appositamente studiata per l'approssimazione numerica del sistema dinamico linearizzato evitando l'insorgere di autovalori spurii che possano inficiare l'analisi dinamica. L'approccio *ottimizzare-poi-discretizzare* è impiegato per superare le difficoltà matematiche introdotte dall'accoppiamento tra correnti attraverso le interfacce.

Per calcolare i guadagni del controllore ottimo (Linear Quadratic Regulator - LQR) da applicare nella simulazione numerica diretta della corrente nel canale con pareti porose, la tecnica per il controllore a minima energia introdotta da Bewley, Pralits e Luchini è stata estesa all'approccio dell'aggiunto continuo. La tecnica dell'aggiunto del diretto aggiunto (ADA) è stata utilizzata per calcolare i guadagni per autorità di controllo più elevate.

I risultati mostrano che la modellazione degli attuatori può influenzare le proprietà di robustezza dei controllori ottimi per la corrente in un canale piano.

Parole chiave

Linear Quadratic Regulator - Volume Averaged Navier-Stokes Equations - Metodi spettrali multidominio - Aggiunto continuo - Equazioni algebrico-differenziali

Estratto della tesi

Il controllo ottimo della corrente in un canale piano è un classico banco di prova per lo studio di algoritmi di controllo in retroazione di correnti di interesse industriale e aeronautico (condotte, corpi aerodinamici) allo scopo di ridurre la resistenza di attrito, con conseguenti benefici in termini energetici ed economici.
Il calcolo dell'azione di controllo attraverso la retroazione di opportune misure consente al sistema di avere una capacità di autoregolazione, in grado di garantire il buon funzionamento del controllo anche in condizioni operative che si discostano dalle condizioni di progetto. Il recente sviluppo di sistemi micro-elettromeccanici consente lo studio e la fabbricazione di dispositivi in grado di operare alle piccole scale spaziali dei fenomeni turbolenti; tra questi, attuatori che implementano getti sintetici consentono di interagire con la corrente che lambisce una parete solida attraverso l'aspirazione ed il soffiaggio di piccole quantità di fluido.
La complessità del problema richiede la sintesi di diverse discipline, la capacità di comprendere il fenomeno fisico e di gestire l'implementazione (e la futura manutenzione) di impianti di controllo pratici ed efficaci. Perciò, il controllo di correnti aerodinamiche è tipicamente affrontato scomponendo il problema nelle sue componenti di comprensione fisica del fenomeno (*Su cosa deve agire il controllo, e come?*), di modellazione matematica (*Come si può calcolare?*), e di implementazione sperimentale (*Come può essere costruito il sistema di controllo?*).
Questo lavoro di occupa della fase di modellazione matematica e di calcolo di una legge di controllo ottimo.
Nella costruzione di modelli per il calcolo di controllori e osservatori ottimi per la corrente in un canale piano, una distributione continua di getti sintetici sulle pareti è generalmente assunta. La ragione di questa ipotesi è la sua semplicità, ma chiaramente gli effetti delle dimensioni finite dei singoli attuatori vengono completamente trascurati. Questo lavoro introduce una prima modellazione degli effetti macroscopici di una distribuzione di attuatori sulle pareti, e della loro influenza nella sintesi di un controllore ottimo. Poiché la presenza degli attuatori

altera la superficie delle pareti introducendo una distribuzione di pori attraverso i quali il fluido viene soffiato ed aspirato, la sostituzione della parete impermeabile con uno strato poroso è un primo passo verso l'inclusione di un modello di attuatore nella sintesi del controllo.

Gli strati porosi sono stati modellati con le equazioni di Navier-Stokes mediate nel volume (Volume Averaged Navier-Stokes equations - VANS) completate dalle condizioni di interfaccia di Ochoa-Tapia per modellare l'accoppiamento tra la corrente nel canale e nello strato poroso. Questo approccio consente di calcolare le proprietà della corrente su una scala spaziale sufficientemente piccola rispetto alle dimensioni del canale, ma allo stesso tempo sufficientemente grande rispetto alle scale dei singoli pori, evitando le difficoltà computazionali di una modellazione geometrica completa del materiale poroso ed un livello di dettaglio eccessivo dal punto di vista ingegneristico.

Il problema di controllo ottimo (Linear Quadratic Regulator - LQR) è stato quindi risolto per il sistema multidominio costituito da un canale piano compreso tra due strati porosi, sotto i quali è stata imposta l'azione di controllo attraverso getti sintetici. Un'opportuna discretizzazione spaziale delle equazioni di governo in ciascun dominio, linearizzate intorno ad una soluzione di equilibrio, ha permesso la costruzione di un modello algebrico lineare su cui applicare gli algoritmi classici del controllo ottimo. Queste tecniche, tuttavia, sono nate nell'ambito di sistemi *discreti* e la loro applicazione sulla *discretizzazione* di un sistema *continuo* può causare delle inconsistenze numeriche tali da inficiare il calcolo e richiedere lo sviluppo di tecniche di discretizzazione che siano consistenti anche per il problema *aggiunto discreto*, su cui si basa la soluzione del controllo ottimo. Per essere sicuri della consistenza dei risultati, quindi, si è preferito adottare l'approccio alternativo in cui il problema di controllo è risolto tramite la derivazione analitica del problema *aggiunto continuo*, e solo successivamente discretizzato per averne una approssimazione numerica.

Poiché l'obiettivo è l'utilizzo di un modello linearizzato del sistema per un unico calcolo dei guadagni da applicare alla simulazione del sistema nonlineare o nell'impianto sperimentale, è necessario adottare tecniche di ottimizzazione finalizzate al calcolo diretto della matrice dei guadagni, senza poter utilizzare la classica equazione di Riccati. Una di queste tecniche è stata sviluppata per il controllore a minima energia [16], ed in questo lavoro è stata estesa all'utilizzo del'aggiunto continuo. Così si è potuto valutare l'effetto della porosità sul calcolo dei guadagni per il controllore ottimo con il minimo livello di autorità. I risultati sono stati estesi a valori maggiori di autorità di controllo attraverso la tecnica dell'aggiunto del diretto-aggiunto (ADA) [90].

L'analisi dell'effetto della porosità sui guadagni del controllore evidenzia l'importanza della modellazione degli effetti indotti dalla geometria degli attuatori nelle procedure di sintesi del controllo. Assumendo che la permeabilità sia un modello del sistema fisico migliore rispetto ad una distribuzione continua di attuatori, non è possibile ricavare risultati conclusivi riguardo alla robustezza di questo tipo di controllori (sia ricavati da un modello impermeabile, che da un modello permeabile) in un'applicazione sperimentale; in ogni caso, le considerazioni sulla robustezza a fronte delle incertezze di modello andranno riviste nell'ottica della sintesi di un osservatore ottimo e della necessità di una procedura di recupero di robustezza (Loop Transfer Recovery - LTR). La permeabilità come modello per la distribuzione di attuatori può permettere di avere una procedura di calcolo del controllo adattabile alle caratteristiche dello specifico impianto di controllo; ulteriori studi sono necessari per valutare gli effetti di questo modello per un'elevata autorità del controllore e per correlare le proprietà del materiale poroso con le caratteristiche dell'impianto di controllo.

Contents

List of Figures

List of Algorithms

List of Tables

1

Introduction

This work is aimed to the development of a linear quadratic regulator for the incompressible flow in a plane channel with porous walls. Porosity is used as a macroscopic model for the finite-size blowing-suction actuators placed at walls.
This chapter provides the framework necessary to state the problem which will be analyzed in the rest of this thesis.

1.1 Background: Flow control and porous media

Flow control is an emerging discipline of fluid dynamics, whose aim is to alter the natural development of a fluid flow. The control can be applied to both wall-bounded or free-shear flows to alter the intensity and distribution of pressure and shear stress generated by the flow, in order to achieve engineering goals such as drag reduction, lift enhancement, transition or separation delay, noise suppression. Other objectives can be the increase of heat transfer or mixing enhancement in applications such as HVAC, internal combustion engines, chemical reactors or pollutant dispersion.

Studies of drag reduction techniques in wall-bounded flows are motivated by the huge potential fuel saving in aeronautical and naval transportation, which could lead to both economical and ecological benefits. Among the various forms of drag, skin friction accounts for about 50 % to 90% of the total drag of, respectively, subsonic aircraft and underwater vehicles [33]. Similarly, drag reduction can lead to substantial power saving in water, oil or gas pipelines[1].

According to the means involved and the energy spent to achieve the objective, two main control strategies can be identified (figure 1.1). Active control, in which some energy is spent to modify the fluid flow (for example, by means of blowing

---

[1] For a complete review of flow control strategies and their implementation issues, the reader is referred to the book of Gad-el-Hak [33].

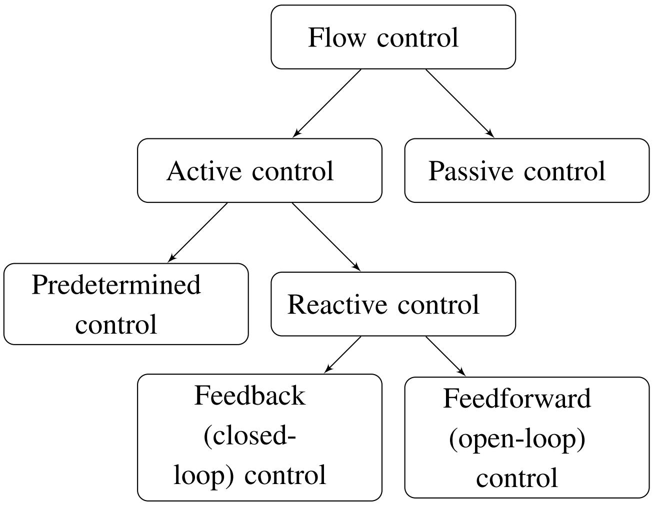

Figure 1.1: Basic classification of control techniques.

and suction of fluid through the walls or prescribed wall movement), and passive control, in which no additional energy is spent and flow properties are altered by an appropriate design of a rigid wall shape or the mechanical properties of a compliant wall. Another basic distinction in active control techniques can be made between feedback control techniques, in which the instantaneous actuation is related to the present or past measurements of some flow properties, and feedforward control techniques, in which some deeper knowledge of the fluid flow phenomenon is exploited to develop an a priori control law to be applied regardless of the current flow state.

Net power saving, weight and complexity are key aspects to be considered in the evaluation of the performance of a control scheme. For a drag reduction technique to be energetically convenient, the power spent to drive the actuators must be less than the power saved thanks to drag reduction. In order to be exploited on transportation vehicles, the additional power required due to the control plant weight must be taken into account. Finally, manufacturing and maintenance complexity is the last obstacle to be climbed over by an energetically efficient control scheme to be physically implemented.

Although important results have been achieved, both in numerical simulations and experimental investigations, complexity often prevents promising control techniques from being implemented in practical control systems.

Feedback control techniques rely on the arrangement of large arrays of sensors and actuators along the flow boundaries. Measurements are used to estimate the deviations of the flow system from the nominal operating conditions, and the con-

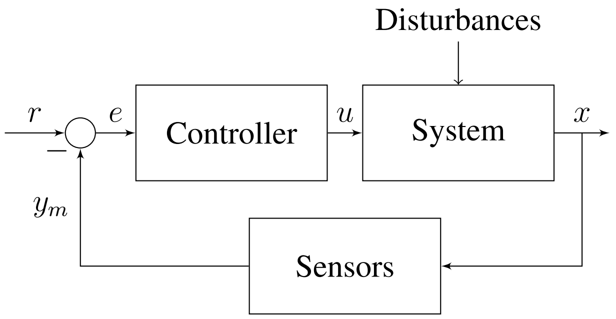

Figure 1.2: Conceptual representation of a feedback control system.

trol action is updated according to a flow model in order to keep the flow near a reference condition and achieve the desired performances (figure 1.2). Although these techniques have proven to provide effective means of reducing turbulent skin friction drag, manufacturing and maintenance difficulties related to the arrangement of large arrays of sensors and actuators often prevent promising techniques from being fully exploited. Feedback control strategies will be the subject of section 1.1.1.

Feedforward control techniques can substantially reduce the complexity of control schemes, but still rely on the arrangement of arrays of actuators. Recently, numerical simulations and experimental measurements have proven that forcing a channel or pipe flow with streamwise-traveling waves of spanwise wall velocity, imposed by the walls motion, can lead to significant drag reduction in a specified range of wavelengths and phase speeds [93]. Moreover, a positive power budget has been demonstrated in the same range of wavelengths and phase speeds in which the drag reduction is the most considerable.
Due to the difficulty to convert this results into a practical implementation, passive control techniques can provide energetically convenient, manufacturing simpler strategies to reduce drag. A classical example of these techniques are riblets, which have been successfully applied both in experimental and full aerodynamic configurations [38]. Tiny longitudinal grooves aligned with the flow direction inhibit spanwise velocity fluctuations. The drag reduction is proportional to the grooves height and spacing up to an optimal size of the order of ten wall units, when near-wall quasi-two-dimensional spanwise vortices form, leading to a drag increase. Such a limitation in the grooves dimensions lead to manufacturing and maintenance issues in many flows of engineering interest, with consequent additional costs which limit the applicability of this technique.

Classical, idealized flow cases, due to the rich flow phenomena they are able to capture despite their simplicity, have been used as a benchmark for control strategies. All of these models consider flows with one or more spatially invariant directions. Plane channel flow, two-dimensional cylinder wake, the Burgers equation and the Lorenz flow system are among them. Simple models are fundamental to assess the efficacy of the control schemes before complicating the physical model with the introduction of further details.

1.1.1 Model-based linear feedback control

The application of standard state-space linear control theory[2] requires the use of a suitable linearized flow model. The *linear* controller is then applied to the *nonlinear* flow system. If the controller is successful in driving the system towards the reference state, then the validity of the linearized model is guaranteed by feedback, which prevents the system from drifting too far away from the desired trajectory [106]. So, the model does not need to be an accurate description of the complete dynamics of the physical system. The model is required to accurately represent only the input-output dynamics, at least in a small neighbourhood of the reference state. Moreover, the ability of feedback to compensate disturbances and to deal with measurement noise can be exploited to handle design uncertainties, making the controller suitable to be used slightly outside its design conditions.

This is the reason for the wide application of linear feedback controllers in industry and for the great attention their application to fluid dynamics has received [12, 62]. The advent of micro-electro-mechanical systems (MEMS) has provided the technology to implement large arrays of sensors and actuators on the flow boundaries, though a practical implementation (in terms of costs, maintenance and modeling of the actuators) is still an open issue [60].

Moreover, compensators for spatially invariant systems with a suitable degree of autority are localized in space. The amount of information that each actuator needs from the surrounding sensors decays exponentially in space [5]. This property is expected, as the actuator influence on the flow will decay in space, and allows to relax the nonphysical assumption of spatially invariance of the flow:

---

[2] The reader is referred to the books of Friedland [35], Skogestad and Postlethwaite [106], Zhou, Doyle and Glover [114] for treatments of classical state-space methods, multivariable feedback control and modern optimal and robust control.
Reviews of the application of linear feedback control theory to fluid dynamics can be found in the works of Bewley [12] and Kim and Bewley [62].

Hopes are that a highly localized compensator should be effective also when applied in a less idealized setup.

1.1.1.1 Laminar flow control

In the last decade, the application of multiple-input, multiple-output optimal and robust control to delay transition to turbulence in a plane channel started to be investigated [14, 27]. Most of the works considered a continuously distributed actuation, by means of zero net mass flux blowing and suction at walls, and distributed wall measurements of shear stress and pressure.

Stability analysis of laminar flows is traditionally performed using a linearization of the Navier-Stokes equations around the laminar base flow, and application of linear control is a logical extension of stability analysis.

From a technical viewpoint, the Navier-Stokes equations for incompressible flows form a system of differential-algebraic equations (DAE); pressure plays the role of a Lagrange multiplier necessary to enforce the incompressibility constraint, and lacks of an evolution equation. The resulting system is singular, and classical methods for optimal control are difficult to apply. Several techniques exist to reduce the DAE system to normal form, i.e. a set of purely ordinary differential equations (ODE) suitable to standard control methods. They basically consist in projecting the system on a divergence-free manifold; a new set of variables is chosen so that the incompressibility constraint is implicitly satisfied. Velocity-vorticity formulations and the pressure Schur complement technique are among them (this issue will be further developed in chapter 3).

Once a state-space representation of the system is available, optimal and robust control is a standard choice to efficiently manage the abundance of design parameters available in the multiple input-multiple output setting. Full compensators are computed leveraging the separation theorem. The optimal control and estimation problems can be studied separately, and the resulting compensator will still be optimal.

The linearized model for plane channel flow resulted to be stabilizable (but not controllable) and detectable (but not observable), with both these properties degrading with increasing Reynolds number and transition to turbulence [14, 62]. Optimal and robust compensators have proven to be effective in reducing the system $\mathcal{H}_2$ and $\mathcal{H}_\infty$ norms and in delaying transition to turbulence [14, 54, 53], although the estimation phase has shown to be the most critical.

The effectiveness of these controllers has been explained with their ability to reduce the system nonnormality [14], which is deemed to play an important role in transition to turbulence. Nonnormality can explain the inability of spectral analysis to predict transition to turbulence [108], since eigenvalues are able to explain only the long-time behaviour of a linear systems, while the transient behaviour of a nonnormal linear system is characterized by large transient energy growth (due to constructive interference of the eigenfunctions) which could trigger nonlinear effects. Pseudospectra and singular value decomposition (SVD) are better tools to study systems characterized by a high level of directionality [108], as it has been recognized in the control community also [106].

1.1.1.2 Turbulent flow control

The motivation behind the application of linear control theory to turbulent flows, beyond simplicity, can be found in the evidences of the importance of linear processes in near-wall turbulence. The linear coupling term in the Orr-Sommerfeld and Squire equations plays a great role in enhancing nonnormality and sustaining turbulence production [63], and turbulence decays without this term. Controllers derived from objective functionals directly targeting this term have been successfully employed through gain-scheduling techniques [55].

The best attainable result in terms of power consumption in transpiration-controlled channel flows is relaminarization of the turbulent flow [13]. Techniques leading to sublaminar drag (as that found in [81]) would spend more power for the control system than that saved thanks to drag reduction.

Early attempts in turbulence feedback control aimed at directly targeting the near-wall structures (the *opposition control* [26]) or used iterative, computationally expensive optimization techniques on the nonlinear system to test the effects of different objective functional on drag reduction and power consumption [15].

The attractiveness of state-space methods, which allow the computation of control and estimation gains in a one-time offline procedure, led to the application of the same compensators derived for laminar plane channel flow to the turbulent case. Effectiveness in drag reduction depends on the choice of the base flow for linearization (and the use of fixed or scheduled gains), the objective functional, and the amount of information about the flow available to the controller.

Högberg, Bewley and Henningson [54] reported that a full-information controller computed using the laminar velocity profile and the energy norm was not able to relaminarize the flow once transition had occurred, while Cavaglieri [25] reported successful relaminarization using the same controller. The reason for these discrepancies has been suggested in the different accuracy attained in the solution of the algebraic Riccati equation; direct methods (based on the Schur factorization) used in the former work are known to produce inaccurate results when the Hamiltonian spectrum is close to the imaginary axis, while iterative (Newton-Kleinman) methods used in the latter allow to specify an arbitrary tolerance on the results accuracy. Cavaglieri also investigated the use of other norms (the dissipation and the enstrophy norms) which could be more appropriate in targeting turbulence.

A gain-scheduling technique, in which the full-information control gains were recomputed at fixed times from a model linearized around the current turbulent mean velocity profile, has proven to be successful in relaminarizing the flow [55]. The use of the mean turbulent profile for linearization has been studied by Martinelli [77], which investigated the use of second order statistics for the characterization of the noise structure in the estimation problem proposing a frequency based approach (the Wiener-Hopf filter) to include the noise time structure also. The resulting estimator, however, did not outperform significantly the previously used linear time-invariant estimators, since the inability to seize the nonlinear energy redistribution among different time and space scales remains a fundamental limitation of linear estimators (which are decoupled in wavenumber space).

A unified framework for the evaluation of drag reduction techniques in turbulent flows has been proposed in [36]; it has been observed that drag reduction mechanism in wall-bounded flows is related to forcing the near-wall velocity fluctuations towards axisymmetry. Linear feedback controllers, however, seem not to respect this trend [77], and the effects of these controllers show more similarities with those of opposition control [26]. With increasing Reynolds number, it has been shown [78] that there is no significant loss of performance in skin friction reduction, while the efficacy of full-information controllers in reducing turbulent kinetic energy degrades.

1.1.2 Flow control through porous media

Flow through porous media occurs in a variety of situations. Applications range from geophysical fluid dynamics (flow over river and sea beds, through permeable rocks, over forests) to bio-fluid dynamics (flow in blood vessels, lungs, kidneys, gastrointestinal system), industrial processes (filtration, papermaking) and aeronautical and energetical applications (transpiration cooling of rocket nozzles, transition and turbulence control, petroleum engineering).

Porous media have been used for boundary layer suction in wind tunnels [8] and on aircraft wings [58], and for delaying transition to turbulence in hypersonic boundary layers by means of passive coatings [74, 104, 19]. Specific flow control techniques have been investigated for oil recovery enhancement applications [3, 41, 42].

Traditionally, most efforts in active control of plane channel flow have focused on control techniques based on zero-net-mass-flux distributed blowing and suction of fluid through the walls. In numerical simulations, the blowing-suction distribution is usually assumed to be continuous, neglecting the details of the actuators and sensors geometry. Although this idealized setting is sufficient for a preliminary assessment of control strategies effectiveness, more refined models should be introduced to investigate the effects of finite-sized actuators. The implementation of MEMS actuators would require the lining of channel walls with small pores, through which fluid should be injected or removed. A simulation of the interaction between a single zero-net-mass-flux actuator (modeled as a cavity driven by an oscillating membrane) with channel flow has been proposed in [12]; much work is in progress in the low-dimensional modeling of synthetic jets [96, 37], but a detailed simulation of a complete array of actuators is computationally challenging.

Due to the tiny dimensions of MEMS actuators and sensors, a first step towards the modeling of the macroscopic effects of the distributed control configuration could be the replacement of impermeable channel walls with permeable layers, and the imposition of the control law beneath them. This approach should allow to assess the global effects of finite-sized actuators, still neglecting the influence of every single pore, and will be pursued here.

1.1.2.1 Governing equations for incompressible flows through porous media

The incompressible flow through a porous medium is governed by the Navier-Stokes momentum and continuity equations

$$\begin{aligned} \frac{\partial \mathbf{u}}{\partial t} - \nu \nabla^2 \mathbf{u} + \mathbf{u} \cdot \boldsymbol{\nabla} \mathbf{u} + \frac{1}{\bar{\rho}} \boldsymbol{\nabla} P = 0 \\ \boldsymbol{\nabla} \cdot \mathbf{u} = 0 \end{aligned} \tag{1.1}$$

provided with suitable initial and boundary conditions. Their solution, however, would require a complete geometrical characterization of the porous medium and would lead to an amount of results which would be often unnecessary in the engineering practice. Although a simplified geometrical description of the porous medium (modeled as an array of rigid cylinders or constricted channels) has been considered in some works [41, 42, 113, 70], the traditional and the most widespread approach has focused on the description of the porous medium at a macroscopic level.

One of the first constitutive laws for flows through porous media has been derived by Darcy (1856), who studied water filtration through beds of sand [28]. Darcy considered the steady parallel incompressible flow through a homogeneous porous medium bounded by impermeable walls. Based on the experimental evidence that these flows experience an adverse pressure gradient proportional to the flow rate, the conservation of momentum leads to the Darcy's law

$$\mathbf{q} = -\frac{k}{\mu}\boldsymbol{\nabla}P \tag{1.2}$$

where $\mathbf{q}\left[\frac{l}{t}\right]$ is the *Darcy's flux*, which represents the (vector) flow rate per unit area, $\mu\left[\frac{m}{lt}\right]$ is the dynamic viscosity of the fluid and $k\ \ [l^2]$ is the *permeability* of the medium, i. e. a measure of the propensity of the porous material for being passed through by a fluid flow.
Defining the *porosity* as the fluid fraction of a porous material

$$\epsilon \equiv \frac{V_f}{V} \tag{1.3}$$

the *pore velocity* can be introduced

$$\mathbf{U} \equiv \frac{\mathbf{q}}{\epsilon} \tag{1.4}$$

accounting for the fact that only a small amount of the material volume is available for fluid flow, so the fluid velocity in the pores must be higher than the Darcy's flux. The Darcy's law can now be rewritten as

$$\mathbf{U} = -\frac{k}{\mu\epsilon}\boldsymbol{\nabla}P \tag{1.5}$$

The flow model considered by Darcy allows to derive a simple and effective constitutive law for flows through porous media, but it neglects unsteadiness, viscous drag, inertial effects and directional properties of the medium. Several improvements to the model have been proposed; the permeability tensor accounting for the directional properties, the Forchheimer correction for nonlinear effects and the Brinkman correction for viscous effects being some of them [111].
A unified framework for these models has been proposed by Whitaker [111] with the Volume Averaged Navier-Stokes equations (VANS), which provide a more rigorous and comprehensive macroscopic description of an incompressible flow through porous media. Analogously to the approach undertaken in Large Eddy Simulation (LES) [89], the Navier-Stokes equations can be volume-averaged on a space scale much larger than the characteristic length scale of the pores, but still

much smaller than the macroscopic geometrical scale of the medium.
To this purpose, it is necessary to introduce two different average operators. The *superficial average*, acting on a vector function $\mathbf{f}(\mathbf{x},t)$ and defined as

$$\langle \mathbf{f}\rangle(\mathbf{x},t) \equiv \frac{1}{V}\int_{V_f} \mathbf{f}(\mathbf{x},t)\,\mathrm{d}V \tag{1.6}$$

and the *intrinsic average*

$$\langle \mathbf{f}\rangle^f(\mathbf{x},t) \equiv \frac{1}{V_f}\int_{V_f} \mathbf{f}(\mathbf{x},t)\,\mathrm{d}V \tag{1.7}$$

Superficial and intrinsic averages are directly related thanks to the definition of porosity

$$\langle \mathbf{f}\rangle = \epsilon\langle \mathbf{f}\rangle^f \tag{1.8}$$

The motivation behind these two different definitions is that the superficial average velocity is solenoidal, so it is the preferred representation of the macroscopic velocity field, while pressure measurements are usually available in form of intrinsic averages. Velocity and pressure can be decomposed into an average and a perturbation term

$$\begin{aligned} \mathbf{u} &= \langle \mathbf{u}\rangle + \mathbf{u}' \\ P &= \langle P\rangle^f + P' \end{aligned} \tag{1.9}$$

As for the Reynolds Averaged Navier-Stokes equations (RANS) and the LES equations, the averaging process gives rise to a closure problem for perturbations. Whitaker showed that the Darcy permeability tensor and the Forchheimer correction term arise from the modeling of velocity and pressure perturbations in terms of average velocity and average pressure, while the averaging process naturally leads to the definition of the Brinkman term. Macroscopic inertial terms are usually negligible, while microscopic inertial effects can be relevant. Spatial variations of porosity can be neglected if regions of highly varying porosity are modeled by means of the Ochoa-Tapia momentum transfer conditions [84, 85, 86] to be described in the next section. The final form of the volume-averaged Navier-Stokes and continuity equations for a homogeneous porous medium is [111, 107]

$$\begin{gathered} \frac{1}{\epsilon}\left(\frac{\partial\langle \mathbf{u}\rangle}{\partial t} + \frac{\langle \mathbf{u}'\rangle\cdot\boldsymbol{\nabla}\langle \mathbf{u}'\rangle}{\epsilon} + \boldsymbol{\nabla}\cdot\langle \mathbf{u}'\mathbf{u}'\rangle\right) = -\frac{1}{\bar{\rho}}\boldsymbol{\nabla}\langle P\rangle^f + \\ + \underbrace{\frac{\nu}{\epsilon}\nabla^2\langle \mathbf{u}\rangle}_{\substack{\text{Brinkman}\\ \text{drag}}} - \underbrace{\frac{\nu}{k}\langle \mathbf{u}\rangle}_{\substack{\text{Darcy}\\ \text{drag}}} - \underbrace{\frac{\nu}{k}\mathbb{F}\cdot\langle \mathbf{u}\rangle}_{\substack{\text{Forchheimer}\\ \text{drag}}} \\ \boldsymbol{\nabla}\cdot\langle \mathbf{u}\rangle = 0 \end{gathered} \tag{1.10}$$

1.1.2.2 Interface conditions between channel and porous flow

Coupling a channel flow with the flow in an adjacent layer of porous medium introduces the difficult modeling of the interface conditions, since analytical evidences show that the no-slip condition is no longer valid. Beavers and Joseph [9] considered a laminar channel flow coupled with an adjacent porous flow modeled by the Darcy's law. Since Darcy's law cannot resolve boundary layers inside the porous region, they introduced a discontinuous tangential interface velocity proportional to the Darcy's velocity and validated their boundary condition with experimental data[3]. This condition is non physical, since the velocity at the interface is expected to be continuous, but it allows to avoid the difficult modeling of the transition region between porous and channel flow. This region is characterized by rapid variations in the porous material properties, together with steep velocity gradients which originate a boundary layer referred to as the Brinkman layer [107, 100, 97].
More recently, Ochoa-Tapia and Whitaker [84, 85, 86] developed interface conditions suitable to the volume-averaged Navier-Stokes equations. Since these equations (eq. 1.10) are not valid in the transition region, they introduced interface conditions involving, along with continuity of velocity and pressure, a jump in the tangential stress. Under the assumption of negligible inertial effects in the porous layer (valid for small permeability, typically for a nondimensional value $\sigma \equiv \sqrt{k}/h \leq 0.02$), inertial terms and Forchheimer drag can be neglected in the VANS equations, which can be written as

$$\begin{aligned} &\frac{1}{\epsilon}\frac{\partial \langle \mathbf{u} \rangle}{\partial t} = -\frac{1}{\bar{\rho}}\boldsymbol{\nabla}\langle P \rangle^f + \frac{\nu}{\epsilon}\nabla^2\langle \mathbf{u} \rangle - \frac{\nu}{k}\langle \mathbf{u} \rangle \\ &\boldsymbol{\nabla}\cdot\langle \mathbf{u} \rangle = 0 \end{aligned} \tag{1.11}$$

For these equations, Ochoa-Tapia and Whitaker interface conditions are

$$\begin{aligned} \mathbf{u} &= \langle \mathbf{u} \rangle \\ P &= \langle P \rangle^f \\ \frac{1}{\epsilon}\frac{\partial \langle u \rangle}{\partial y} - \frac{\partial u}{\partial y} &= \mp \frac{\tau}{\sqrt{k}} u \\ \frac{1}{\epsilon}\frac{\partial \langle w \rangle}{\partial y} - \frac{\partial w}{\partial y} &= \mp \frac{\tau}{\sqrt{k}} w \end{aligned} \tag{1.12}$$

---

[3] For an historical perspective on the modeling of interface conditions, the reader is referred to the works of Tilton [107] and to the theses of Rosti [97] and Scarselli [100].

where τ is a coefficient accounting for the momentum jump at the interface (determined experimentally), the $\mp$ sign refers to the position of the porous layer (at the top or at the bottom of the channel, respectively) and $(\mathbf{u},\ P)$ are velocity and pressure in the channel governed by the Navier-Stokes equations (eq. 1.1) with no-slip condition on the impermeable wall.

1.2 Problem statement

This work is aimed to the design of a Linear Quadratic Regulator (LQR) for the incompressible flow in plane channel bounded by two rigid parallel layers of homogeneous porous media, where the porosity is sufficiently small to neglect inertial effects.

The fluid region is governed by the Navier-Stokes momentum and continuity equations while the porous regions are governed by the VANS momentum and continuity equations, provided with no-slip conditions at the impermeable walls and the Ochoa-Tapia conditions at the interfaces

$$\begin{aligned}
\frac{\partial \mathbf{u}}{\partial t} - \nu\nabla^2\mathbf{u} + \mathbf{u}\cdot\boldsymbol{\nabla}\mathbf{u} + \frac{1}{\bar{\rho}}\boldsymbol{\nabla}P &= \mathbf{0} \\
\boldsymbol{\nabla}\cdot\mathbf{u} &= 0 && \text{in} \quad \Omega \\
\frac{1}{\epsilon_j}\frac{\partial\langle\mathbf{u}\rangle_j}{\partial t} + \frac{\nu}{k_j}\langle\mathbf{u}\rangle_j - \frac{\nu}{\epsilon_j}\nabla^2\langle\mathbf{u}\rangle_j + \frac{1}{\bar{\rho}}\boldsymbol{\nabla}\langle P\rangle_j^f &= \mathbf{0} \\
\boldsymbol{\nabla}\cdot\langle\mathbf{u}\rangle_j &= 0 && \text{in} \quad \Omega_j \\
\langle\mathbf{u}\rangle_j &= 0 && \text{on} \quad \Gamma_{w,j} \qquad (1.13) \\
\mathbf{u} &= \langle\mathbf{u}\rangle_j \\
P &= \langle P\rangle_j^f \\
\frac{1}{\epsilon_j}\frac{\partial\langle u\rangle_j}{\partial y} - \frac{\partial u}{\partial y} &= \mp\frac{\tau_j}{\sqrt{k_j}}u \\
\frac{1}{\epsilon_j}\frac{\partial\langle w\rangle_j}{\partial y} - \frac{\partial w}{\partial y} &= \mp\frac{\tau_j}{\sqrt{k_j}}w && \text{on} \quad \Gamma_{i,j}
\end{aligned}$$

where index $j = 1, 2$ refers to the upper and lower porous layers, respectively. The channel is assumed to extend indefinitely in the wall-parallel directions, in which periodic boundary conditions will be assumed.

The same configuration has been considered in the linear stability analyses of Tilton and Cortelezzi [107] and Scarselli [100], who performed the eigenanalysis and the computation of the transient energy growth, respectively, and in the turbulent Direct Numerical Simulation (DNS) performed by Rosti [97]. They have shown that permeability destabilizes up to two Orr-Sommerfeld eigenvalues at lower Reynolds number than the critical Reynolds number of plane channel flow, and that porous walls are able to sustain turbulence at a very low Reynolds number. This work is in continuity with their studies.

Porous layers are used here as a first macroscopic model for the finite size geometry of the distributed blowing-suction actuators at walls. Thus, in the control setup the feedback law $\boldsymbol{\phi}(x, z, t)$ is used to impose the boundary conditions below the porous regions, replacing the no-slip condition for wall-normal velocity

$$\langle v \rangle_j = \phi_j \quad \text{on} \quad \Gamma_{w,j} \tag{1.14}$$

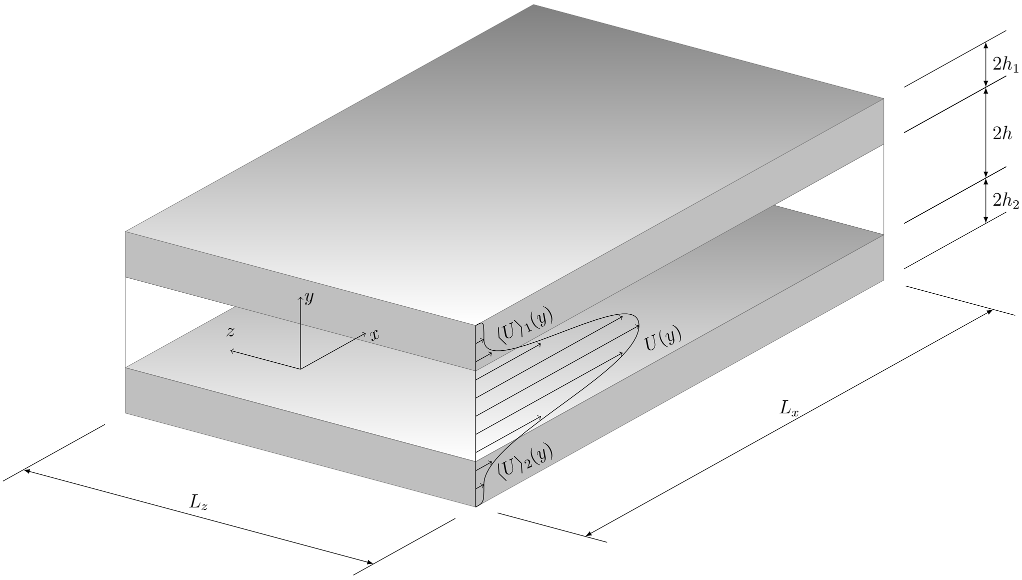

Figure 1.3: Sketch of plane channel with permeable walls. Not to scale.

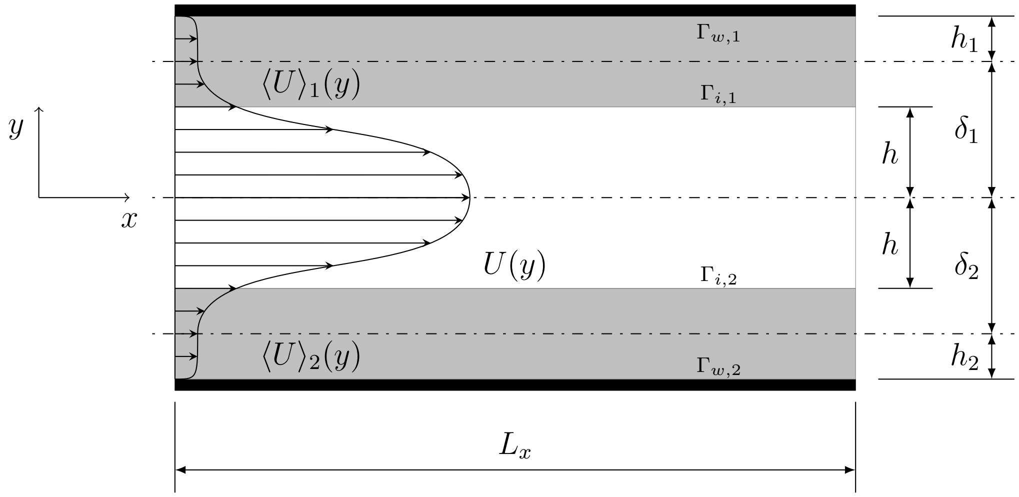

Figure 1.4: Section of plane channel with permeable walls. Not to scale.

2

Full-state optimal controller design

This chapter presents the theoretical development of a model-based linear feedback controller for the problem defined in section 1.2. Due the interdisciplinarity of the problem, the most general framework is provided in order to benefit from the advances in neighbouring disciplines.

The setup sketched in section 1.2 has several features in common with similar control problems arising in engineering, physics and mathematics. The channel is composed by different layers, which are coupled at the interfaces among them, and the flow in each of them is governed by its own equations. The system is controlled through its boundary by means of distributed wall actuation. In mathematical terms, this situation can be abstracted in a boundary control problem of coupled (multidomain) systems of partial differential equations [69, 82].

In accordance with the separation theorem [35], the optimal control and observation problems can be solved independently and the resulting compensator will still be optimal for the problem at hand. So, this work deals with the design of the optimal full-state feedback controller only. Since the observation problem for plane channel flow (and fluid flows in general) has proven to be challenging [77, 54, 11], performances of the designed full information controller will be useful to motivate further studies of a state observer.

First, the control problem is introduced for an uncoupled, single-domain system (section 2.1). Then the effects of spatial invariance of the flow in the wall-parallel directions are explained (section 2.2). Finally, the discussion is extended to the coupled, multidomain case (section 2.3) and the control techniques adopted in this work are presented (section 2.4).

2.1 Optimal boundary control of continuum systems

Let us consider an infinite-dimensional, linear[1] time-invariant system of partial differential equations in descriptor form[2] controlled on a portion of the boundary

$$\begin{aligned} \mathcal{E}\frac{\partial \mathbf{x}}{\partial t} &= \mathcal{A}\mathbf{x} && \text{in } \Omega \\ x_j &= \phi_i && \text{on } \Gamma_i \end{aligned} \tag{2.1}$$

provided with suitable boundary conditions (dependent on the specific problem) on the uncontrolled portion of the boundary. The state variable $\mathbf{x}$ is a complex[3] vector-valued function defined in a suitable Hilbert space on the domain Ω, while the complex vector of boundary values $\boldsymbol{\phi}$ is defined in a Hilbert space on the controlled boundary Γ only. A component of the state variable is constrained by a component of $\boldsymbol{\phi}$ on a specific subset of Γ.

When dealing with multiple-input multiple-output (MIMO) systems, optimal control is a standard choice to exploit the overabundance of design parameters for the minimization of a suitable performance index, expressed as an objective functional. This is typically defined as the time integral of a suitable norm of the state $\mathbf{x}$ and the control input $\mathbf{u}$

$$\mathcal{J} = \frac{1}{2}\int_0^T \left(||\mathcal{C}\mathbf{x}||^2_{L^2(\Omega)} + ||\mathbf{D}\mathbf{u}||^2_{L^2(\Gamma)} \right) \mathrm{d}t \tag{2.2}$$

where the operator $\mathcal{C}$ and the matrix $\mathbf{D}$ depend on the specific choices of the weighted L^2 norms of the state and the control vectors. The choice of the $L^2(\Gamma)$ norm for the control input is dictated from the fact that $\mathbf{u}$ is defined only on the controlled boundary Γ, and not inside the volume Ω

---

[1] In most cases, as the one at hand, the model system is the result of the linearization of a nonlinear system around a reference state.

[2] Throughout this chapter, we will make use of standard tools of functional analysis and system dynamics. For a review of functional analysis and linear differential operators, the reader is referred to the books of Salsa [99] and Lanczos [65] respectively. For a review of system dynamics and descriptor linear systems, the reader is referred to the books of Cannon [20] and Duan [32] respectively.

[3] Since we will deal with complex Fourier coefficients, we develop all of our analysis for complex functions.

$$||\mathcal{C}\mathbf{x}||^2_{L^2(\Omega)} = \int_\Omega (\mathcal{C}\mathbf{x})^2 \,\mathrm{d}\Omega \tag{2.3}$$

$$||\mathbf{D}\mathbf{u}||^2_{L^2(\Gamma)} = \int_\Gamma (\mathbf{D}\mathbf{u})^2 \,\mathrm{d}\Gamma \tag{2.4}$$

The integral definition of the objective functional enforces the requirement for the system to be stabilizable (unless, the integral will diverge in time), while the weighting of the control input (referred to as Tikhonov regularization in the context of ill-posed problems) limits the actuation power avoiding actuator saturation.

The boundary control is unusual in the context of classical control theory, whose techniques have been developed for discrete systems first and are more at ease with a control input acting through a matrix $\mathbf{B}$ rather than through a boundary condition. Control theories have been generalized to infinite-dimensional systems with the presence of a volume forcing acting through an operator $\mathcal{B}$ and, in order to exploit well-established control techniques, it is useful to recast our boundary forcing into a volume forcing through a lifting procedure [82, 17]. Thanks to linearity, the state $\mathbf{x}$ can be decomposed into a term $\mathbf{x}_0$ with homogeneous boundary conditions on the controlled portion of the boundary and a term $\mathbf{x}_\phi$ with inhomogeneous conditions on the same portion of the boundary

$$\mathbf{x} = \mathbf{x}_0 + \mathbf{x}_\phi \tag{2.5}$$

Separation of variables can be invoked to relate $\mathbf{x}_\phi$ to the imposed boundary values $\boldsymbol{\phi}$ through a matrix of arbitrary *lifting functions* $\mathbf{G}(\mathbf{r})$ depending on the space coordinates $\mathbf{r}$ only

$$\mathbf{x}_\phi(\mathbf{r}, t) = \mathbf{G}(\mathbf{r})\boldsymbol{\phi}(t) \tag{2.6}$$

Substitution into the system leads to

$$\mathcal{E}\frac{\partial \mathbf{x}_0}{\partial t} + \mathcal{E}\mathbf{G}\frac{\partial \boldsymbol{\phi}}{\partial t} = \mathcal{A}\mathbf{x}_0 + \mathcal{A}\mathbf{G}\boldsymbol{\phi} \tag{2.7}$$

Now, the control input has to be chosen. The two simplest choices are the boundary values on the controlled boundary $\boldsymbol{\phi} = \mathbf{u}$ or their time derivatives $\frac{\partial \boldsymbol{\phi}}{\partial t} = \mathbf{u}$. Both of them can be accounted for by writing a first order relation

$$m_1\frac{\partial \boldsymbol{\phi}}{\partial t} = m_0\boldsymbol{\phi} + \mathbf{u} \tag{2.8}$$

Setting $m_1 = 0,\ m_0 = -1$ leads to $\boldsymbol{\phi} = \mathbf{u}$, while $m_1 = 1,\ m_0 = 0$ leads to $\frac{\partial \boldsymbol{\phi}}{\partial t} = \mathbf{u}$. Other combinations allow to consider more involved first order relations, and are not investigated in this work.

The controlled system now reads

$$\underbrace{\begin{pmatrix} \mathcal{E} & \mathcal{E}\mathbf{G} \\ 0 & m_1 \end{pmatrix}}_{\mathcal{E}_s} \frac{\partial}{\partial t} \underbrace{\begin{pmatrix} \mathbf{x}_0 \\ \boldsymbol{\phi} \end{pmatrix}}_{\mathbf{x}_s} = \underbrace{\begin{pmatrix} \mathcal{A} & \mathcal{A}\mathbf{G} \\ 0 & m_0 \end{pmatrix}}_{\mathcal{A}_s} \underbrace{\begin{pmatrix} \mathbf{x}_0 \\ \boldsymbol{\phi} \end{pmatrix}}_{\mathbf{x}_s} + \underbrace{\begin{pmatrix} 0 \\ \mathbf{I} \end{pmatrix}}_{\mathcal{B}_s} \mathbf{u} \tag{2.9}$$

provided with homogeneous boundary conditions on the controlled portion of the boundary and the usual ones on the uncontrolled portion. Note that the first row in eq. 2.9 is a system of partial differential equations (PDEs), while the second row is a system of ordinary differential equations (ODEs) in time. The full state $\mathbf{x}_s$ is then composed by an infinite-dimensional part $\mathbf{x}_0$ and a discrete one $\boldsymbol{\phi}$.

In this work, we deal with the linear descriptor system written in the compact form

$$\mathcal{E}_s \frac{\partial \mathbf{x}_s}{\partial t} = \mathcal{A}_s \mathbf{x}_s + \mathcal{B}_s \mathbf{u} \tag{2.10}$$

In the rest of this chapter, we consider the descriptor system of eq. 2.10 as if it was composed by the infinite-dimensional part only, since this is the most delicate case to handle. Pedix s is dropped for convenience of notation. The discrete state variables add no contribution to the conceptual development of the control techniques, and the implementation details of the mixed case will be presented after the discretization of the infinite-dimensional system in chapter 3.

There are two ways to solve the optimal control problem. Discretizing the functional objective and the system first, and then performing optimization (discretize-then-optimize approach); or performing optimization first, and then discretizing the functional objective and the system (optimize-then-discretize approach). In the next section the latter approach is presented, and then it is explained why it has been chosen for this work (section 2.3). The former, more classical approach is presented in appendix D.

2.1.1 Optimize-then-discretize (continuous adjoint) approach

This approach is a generalization of the Lagrange multipliers procedure usually adopted in the discretized setting. The infinite-dimensional constrained optimization problem (eq. 2.2) can be recast into an unconstrained one by the introduction of a Lagrange multiplier (adjoint variable) $\boldsymbol{\lambda}$ and the redefinition of functional $\mathcal{J}$ as the Lagrangian[4]

$$\mathcal{J} = \frac{1}{2}\int_0^T \left(||\mathcal{C}\mathbf{x}||^2_{L^2(\Omega)} + ||\mathbf{D}\mathbf{u}||^2_2 - \langle \boldsymbol{\lambda},\, \mathcal{E}\frac{\partial \mathbf{x}}{\partial t} - \mathcal{A}\mathbf{x} - \mathcal{B}\mathbf{u} \rangle_{L^2(\Omega)} \right) \mathrm{d}t \tag{2.11}$$

where the notation $\langle \cdot, \cdot \rangle_{L^2(\Omega)}$ has been introduced to denote the $L^2(\Omega)$ inner product. Integration by parts in time and space can be used to define the adjoint operators[5] $\mathcal{E}^\dagger$, $\mathcal{A}^\dagger$, $\mathcal{B}^\dagger$, $\mathcal{C}^\dagger$. Taking the Fréchet derivatives of the Lagrangian, the infinite-dimensional Hamiltonian system[6] can be derived

$$\begin{pmatrix} \mathcal{E} & 0 \\ 0 & \mathcal{E}^\dagger \end{pmatrix} \frac{\partial}{\partial t} \begin{pmatrix} \mathbf{x} \\ \boldsymbol{\lambda} \end{pmatrix} = \begin{pmatrix} \mathcal{A} & 0 \\ -\mathcal{C}^\dagger\mathcal{C} & -\mathcal{A}^\dagger \end{pmatrix} \begin{pmatrix} \mathbf{x} \\ \boldsymbol{\lambda} \end{pmatrix} + \begin{pmatrix} \mathcal{B} \\ 0 \end{pmatrix} \mathbf{u} \qquad \text{in } \Omega \tag{2.12}$$

provided with suitable boundary conditions, together with the transversality condition

$$\mathbf{R}\mathbf{u} + \int_\Omega \mathcal{B}^\dagger \boldsymbol{\lambda}\, \mathrm{d}\Omega = 0 \tag{2.13}$$

(having defined $\mathbf{R} \equiv \mathbf{D}^H\mathbf{D}$). Once this set of equations has been derived, direct and adjoint equations can be discretized in space according to independent schemes. Looking for a relation between the adjoint and direct variable in the form

$$\boldsymbol{\lambda} = \mathcal{P}\mathcal{E}\mathbf{x} \tag{2.14}$$

and assuming $\mathbf{R}$ to be invertible, we get the feedback relation

$$\mathbf{u} = -\mathbf{R}^{-1}\int_\Omega \mathcal{B}^\dagger \mathcal{P}\mathcal{E}\mathbf{x}\, \mathrm{d}\Omega \equiv \int_\Omega \mathcal{K}\mathcal{E}\mathbf{x}\, \mathrm{d}\Omega \tag{2.15}$$

This relation highlights an important property of infinite-dimensional systems controlled through their boundary: The proportional feedback law is expressed as a volume integral of the state variable[7]. This property cannot be appreciated in the discrete adjoint method (appendix D).

---

[4] The term $||\mathbf{D}\mathbf{u}||^2_{L^2(\Gamma)}$ as been expressed as the euclidean norm $||\mathbf{D}\mathbf{u}||^2_2$, since after Fourier decomposition (see section 3.3) the problem becomes one-dimensional in space.

[5] The adjoint operator is briefly introduced in appendix B. Boundary terms arising from the integration are used to define the adjoint initial and boundary conditions, and are omitted here.

[6] Looking at the Hamiltonian system, the dual nature of the controllability/stabilizability and observability/detectability concepts is clear. The direct variable is forced by the control input through the operator $\mathcal{B}$, while the adjoint variable is forced by the direct one through the operator $\mathcal{C}$.

[7] As noted in [14], the integral definition is necessary to guarantee convergence of the discretized feedback law with grid refinement. This is the same reason behind the integral definition of inner products in function spaces [65].

The integral nature of feedback law is further enhanced in the context of spatially invariant systems. This will be the subject of the next section.

2.2 The benefits of spatial invariance: Localization

Plane channel flow is a highly idealized geometry, which is useful to study fundamental flow physics without concerning with further effects introduced by peculiarities of the flow boundary. The spatial invariance of the flow in the wall-parallel directions allows the use of harmonic analysis to study the behavior of the system in wavenumber space. When dealing with linear dynamical systems, the application of the Fourier transform leads to a decoupled set of dynamical systems for the Fourier coefficients of the state variable. Thus, thanks to Parseval's (or Plancherel's) theorem[8], it is possible to decouple the control problem also

$$\begin{aligned}\mathcal{J} &= \frac{1}{2}\int_0^T \left(||\mathcal{C}\mathbf{x}||^2_{L^2(\Omega)} + ||\mathbf{D}\mathbf{u}||^2_{L^2(\Gamma)}\right)\mathrm{d}t = \\ &= L_x L_z \sum_{\kappa_x,\,\kappa_z} \underbrace{\left[\frac{1}{2}\int_0^T \left(||\mathcal{C}\hat{\mathbf{x}}||^2_{L^2(\hat{\Omega})} + ||\mathbf{D}\hat{\mathbf{u}}||^2_2\right)\mathrm{d}t\right]}_{\hat{\mathcal{J}}} \equiv \\ &\equiv L_x L_z \sum_{\kappa_x,\,\kappa_z} \hat{\mathcal{J}}\end{aligned} \tag{2.18}$$

---

[8] Parseval's theorem allows to write the energy of a function in Fourier space. Its expression, however, depends on the scaling used in the definition of the Fourier coefficients. If we choose to define them as the wave amplitudes, then the Fourier series and its coefficients can be written as

$$\begin{aligned}f(x) &= \sum_{\kappa_x} \hat{f}(i\kappa_x)e^{i\kappa_x x} \\ \hat{f}(i\kappa_x) &= \frac{1}{L_x}\int_{-\frac{L_x}{2}}^{\frac{L_x}{2}} f(x)e^{-i\kappa_x x}\,\mathrm{d}x\end{aligned} \tag{2.16}$$

with $\kappa_x = \frac{2\pi n_x}{L_x}$, $n_x = -N_x, \dots, N_x$. Then Parseval's theorem reads

$$\begin{aligned}\int_{-\frac{L_x}{2}}^{\frac{L_x}{2}} f^2(x)\,\mathrm{d}x &= \int_{-\frac{L_x}{2}}^{\frac{L_x}{2}} f(x)\left(\sum_{\kappa_x}\hat{f}(i\kappa_x)e^{i\kappa_x x}\right)\mathrm{d}x = \\ &\sum_{\kappa_x}\left(\int_{-\frac{L_x}{2}}^{\frac{L_x}{2}} f(x)e^{i\kappa_x x}\,\mathrm{d}x\right)\hat{f}(i\kappa_x) = L_x\sum_{\kappa_x}\hat{f}^*(i\kappa_x)\hat{f}(i\kappa_x)\end{aligned} \tag{2.17}$$

The extension to more spatial dimensions is straightforward.

with $\kappa_x = \frac{2\pi n_x}{L_x}$, $n_x = -N_x, \ldots, N_x$ and $\kappa_z = \frac{2\pi n_z}{L_z}$, $n_z = -N_z, \ldots, N_z$. The y direction is the only spatial dimension remaining, and its domain has been denoted as $\hat{\Omega}$.

Since the control action is distributed in the invariant directions, harmonic analysis applies to the control input as well. Thus, each Fourier component $\hat{\mathcal{J}}$ of the objective functional can be minimized independently. According to the feedback law derived in the previous section (eq. 2.15), the Fourier coefficients of the control input will be proportional to the Fourier coefficients of the state

$$\hat{\mathbf{u}}(t) = \int_{-h-2h_2}^{h+2h_1} \hat{\mathcal{K}}(y)\mathcal{E}\hat{\mathbf{x}}(y,t)\,\mathrm{d}y \tag{2.19}$$

where independent variables have been written explicitly, and integration limits are those of plane channel with permeable walls (fig. 1.4).

As multiplication in wavenumber space leads to convolution in the physical space, the resulting feedback law will be given by the convolution of a control kernel with the state [5, 54]

$$\mathbf{u}(x,z,t) = \int_{\Omega} \mathcal{K}(x-\bar{x},\bar{y},z-\bar{z})\mathcal{E}\mathbf{x}(\bar{x},\bar{y},\bar{z},t)\,\mathrm{d}\bar{x}\,\mathrm{d}\bar{y}\,\mathrm{d}\bar{z} \tag{2.20}$$

It has been shown theoretically [5] that control kernels decay exponentially from the origin. This property states that the amount of information about the state needed by each actuator decays in space, and this allows to argue for spatial truncation (instead of other model reduction techniques) in the physical implementation of such control systems. This *localized* controller structure could allow its implementation in slightly off-design configurations also [12]. However, the degree of localization strongly depends on the control authority, as weaker controllers will be less and less localized in space; to stabilize the system while saving control energy, the controller needs information from farther sensors also.

2.3 Troubles with the *discrete* adjoint: Adjoint consistency

The correctness of the adjoint problem is necessary for the computation of the control law, since each objective functional defines its own adjoint problem (see appendix B), and the control law is directly proportional to the adjoint solution. Hence, any inconsistence in the adjoint problem will be inherited by the feedback gains, with the possibility to spoil the numerical results or not to obtain any result

at all.
The *continuous* approach to the derivation of the adjoint problem has been presented in the previous section (its *discrete* counterpart is presented in appendix D), but nothing has been said about the numerical properties of the two methods.

The *continuous* adjoint problem is derived analytically from the infinite - dimensional direct problem and it is then discretized (*discretization of the adjoint*), possibly with other schemes than those used for the direct problem. If a stable and consistent numerical scheme is used, then convergence of the adjoint numerical solution is guaranteed.

The *discrete* adjoint problem, instead, is derived once the direct problem has been discretized. From the point of view of the implementation, this procedure involves taking the conjugate-transpose of the direct problem matrices (*adjoint of the discretization*). While it is argued that this approach leads to exact (up to machine precision) discrete gradients of the objective functional [40], there is no guarantee that this discrete adjoint problem would be a consistent approximation of the infinite-dimensional adjoint problem.
In fact, it has been noted in several research areas involving optimization through adjoint-based techniques (a posteriori error analysis, sensitivity analysis for adaptive mesh refinement with finite differences [105, 68], discontinuous Galerkin methods for compressible flows [46, 47, 48, 52, 51], finite elements methods for fluid-structure interaction [34]) that the discrete adjoint solution may be affected by non-smooth and oscillatory behavior. Inconsistencies typically arise at the boundaries or even at elements interfaces, and are persistent to mesh refinement [46].

This issue with the discrete adjoint approach has been highlighted since mid 1990s in the context of finite difference methods [102, 105], but the rigorous concept of *adjoint consistency* was formulated only in mid 2000s [71] in the context of discontinuous Galerkin methods. A numerical formulation is said to be *adjoint consistent* if the discrete adjoint problem is a consistent approximation of the continuous adjoint problem. Adjoint consistency does not follow from consistency of the discretized direct problem, in general.
When dealing with *truly discrete* systems, such as electrical or hydraulic networks or lumped-parameters systems, the discrete adjoint approach is automatically used in the optimization procedure, since it is the only possible approach. When adopting a discrete adjoint approach with *discretized* systems, instead, the consistency of the numerical scheme implied by the adjoint of the direct numerical scheme has to be checked.

A clear example of an *adjoint inconsistent* numerical scheme is given in [68] and is reported here. Consider the one-dimensional heat equation

$$\begin{aligned} \frac{\partial u}{\partial t} &= \frac{\partial^2 u}{\partial x^2} \qquad x \in (0,1), \quad t > 0 \\ \left.\frac{\partial u}{\partial x}\right|_{x=0} &= 0 \\ u(1,t) &= 1 \end{aligned} \tag{2.21}$$

whose continuum adjoint problem is

$$\begin{aligned} -\frac{\partial v}{\partial t} &= \frac{\partial^2 v}{\partial x^2} \qquad x \in (0,1), \quad t > 0 \\ \left.\frac{\partial v}{\partial x}\right|_{x=0} &= 0 \\ v(1,t) &= 0 \end{aligned} \tag{2.22}$$

and discretize the direct problem with a central finite difference scheme on a uniform grid

$$\begin{aligned} \left.\frac{\partial u}{\partial x}\right|_{x_i} &\simeq \frac{u_{i+1} - u_{i-1}}{2h} \\ \left.\frac{\partial^2 u}{\partial x^2}\right|_{x_i} &\simeq \frac{u_{i+1} - 2u_i + u_{i-1}}{h^2} \end{aligned} \tag{2.23}$$

Discretization of the PDE on the internal grid points and substitution of the boundary conditions (with the help of ghost points) leads to the discretized direct system

$$\begin{bmatrix} \dot{u}_1 \\ \vdots \\ \dot{u}_N \end{bmatrix} = \frac{1}{h^2} \begin{bmatrix} -2 & 2 & & & & \\ 1 & -2 & 1 & & & \\ & 1 & -2 & 1 & & \\ & & \ddots & \ddots & \ddots & \\ & & & 1 & -2 & 1 \\ & & & & 0 & 0 \end{bmatrix} \begin{bmatrix} u_1 \\ \vdots \\ u_N \end{bmatrix} \tag{2.24}$$

Colored terms belong to the asymmetric part of the numerical sheme. The discrete adjoint problem is obtained simply through matrix transposition and change of sign of the time derivative

$$-\begin{bmatrix} \dot{v}_1 \\ \vdots \\ \dot{v}_N \end{bmatrix} = \frac{1}{h^2} \begin{bmatrix} -2 & 1 & & & & \\ 2 & -2 & 1 & & & \\ & 1 & -2 & 1 & & \\ & & \ddots & \ddots & \ddots & \\ & & & 1 & -2 & 0 \\ & & & & 1 & 0 \end{bmatrix} \begin{bmatrix} v_1 \\ \vdots \\ v_N \end{bmatrix} \tag{2.25}$$

It is evident that the numerical scheme is flipped at the boundaries. It has been shown that the numerical scheme implied by the discrete adjoint in eq. 2.25 is not consistent with *any* continuum partial differential equations, not only with eq. 2.22.

Due to transposition, inconsistencies are likely to occur whenever inhomogeneous boundary conditions are considered, or variational formulations with an asymmetric choice of functional spaces for trial and test functions (Petrov-Galerkin formulations) are employed.

Are these inconsistency a true problem? The discrete adjoint method is argued to lead to functional gradients which are exact up to machine precision, irrespective of the numerical scheme implied by the discrete adjoint. The physical relevance of an inconsistent adjoint solution, however, is questionable, and inconsistencies are likely to seriously hamper any successive adjoint-based numerical computation. Inconsistencies in the adjoint problem, in the present work, have proven to be a serious trouble for any adjoint-based optimization technique.

When dealing with multidomain, coupled optimization problems, the swapping of the interface coupling terms in the discrete adjoint approach is likely to generate similar inconsistencies, unless an *ad hoc* adjoint consistent scheme is studied. To the best of our knowledge, a first attempt in deriving an adjoint consistent formulation for multiphysics problems has been successfully performed in the field of fluid-structure interaction [34]. In this work, for a preliminary assessment of the effects of porous walls on channel flow control, the continuous adjoint approach has been preferred. Further development of an adjoint consistent numerical formulation will be motivated by the obtained results.

2.4 Bypassing the Riccati equation

Since classical spectral discretization techniques for channel flow leading to nonsingular systems have shown to be inconsistent (see chap. 3) and adjoint consistency is a major issue when adopting the discrete adjoint approach with nontrivial boundary and interface conditions, in this work the continuous adjoint approach is employed with the numerical formulation presented in chapter 3. This choice is also in order when dealing with singular descriptor systems[9]. The continuous adjoint framework makes it necessary to adopt numerical techniques for optimal control that avoid the Riccati equation, since most of its methods of solution implicitly assume the usage of the discrete adjoint[10].

2.4.1 A pole placement technique: The minimum energy control

An interesting situation arises in the infinite-horizon control, when the control weight tends to infinity (or, to make the integral in the objective functional in eq. 2.2 well defined, when the state weight tends to zero). The resulting controller is referred in literature as the minimal energy control [35], since the control action is kept to a minimum and its only effect is the reflection of the unstable system eigenvalues with respect to the imaginary axis. In this case, the algebraic Riccati equation reduces to an algebraic Bernoulli equation [1] (just the same equation, in which the forcing term Q is dropped) and an efficient technique has been proposed by Bewley, Pralits and Luchini [16] to compute its solution by exploiting the knowledge of the controlled system spectrum.

The technique has been presented for the discrete adjoint approach with state-space and descriptor systems [16, 24]. Here we further develop this technique in order to apply it with the continuous adjoint approach.

Since in the minimum energy limit the controlled system spectrum is the union of the stable eigenvalues and the reflection (with respect to the imaginary axis) of the unstable eigenvalues of the uncontrolled system, we know the closed-loop

---

[9] Some techniques have recently been presented to solve the algebraic Riccati equations for fluid systems by exploiting the decoupling between differential and algebraic states [50, 49], but their extension to multiphysics problems should be carefully addressed. In the system dynamics community, the classical approach to optimal control of singular descriptor systems is the reduction to a normal (state space) form; these methods are suitable for small discrete systems, and adjoint consistency for continuum systems should be demonstrated.

[10] See appendix D.

spectrum of the Hamiltonian system (eq. 2.12 and 2.13). This knowledge can be exploited to project the Hamiltonian system on the reflected modes[11], greatly simplifying the expression of the algebraic Bernoulli equation and allowing for a solution in closed form.

The Hamiltonian system (eq. 2.12) can be projected on the subspace spanned by the direct and adjoint eigenfunctions ($\mathbf{r}_i$ and $\mathbf{l}_i$, respectively) corresponding to the unstable system eigenvalues σ_i.
Defining the modal projection (assuming Einstein's convention)

$$\begin{aligned} \mathbf{x} &= \mathbf{r}_i \mathbf{x}_i, \quad \mathbf{x}_i = \langle \mathbf{l}_i,\ \mathcal{E}\mathbf{x} \rangle_{L^2(\Omega)} \\ \boldsymbol{\lambda} &= \mathbf{l}_i \boldsymbol{\lambda}_i, \quad \boldsymbol{\lambda}_i = \langle \mathbf{r}_i,\ \mathcal{E}^\dagger \boldsymbol{\lambda} \rangle_{L^2(\Omega)} \end{aligned} \tag{2.26}$$

subject to the normalization

$$\langle \mathbf{l}_i, \mathcal{E}\mathbf{r}_j \rangle_{L^2(\Omega)} = \langle \mathbf{r}_i, \mathcal{E}^\dagger \mathbf{l}_j \rangle_{L^2(\Omega)} = \delta_{ij} \tag{2.27}$$

we can leverage the dynamics decoupling

$$\begin{aligned} \langle \mathbf{l}_i, \mathcal{A}\mathbf{r}_j \rangle_{L^2(\Omega)} &= \sigma_i \delta_{ij} \\ \langle \mathbf{r}_i, \mathcal{A}^\dagger \mathbf{l}_j \rangle_{L^2(\Omega)} &= \sigma_i^* \delta_{ij} \end{aligned} \tag{2.28}$$

to write the system in modal form

$$\begin{aligned} \frac{d\mathbf{x}_i}{dt} &= \sigma_i \mathbf{x}_i + \langle \mathbf{l}_i, \mathcal{B} \rangle_{L^2(\Omega)} \mathbf{u} \\ \frac{d\boldsymbol{\lambda}_i}{dt} &= -\langle \mathbf{r}_i, \mathcal{C}^\dagger \mathcal{C} \mathbf{r}_j \rangle_{L^2(\Omega)} \mathbf{x}_j - \sigma_i^* \boldsymbol{\lambda}_i \end{aligned} \tag{2.29}$$

with the transversality condition

$$\mathbf{u} = -\mathbf{R}^{-1} \langle \mathcal{B}^{\dagger^H}, \mathbf{l}_i \rangle_{L^2(\Omega)} \boldsymbol{\lambda}_i \tag{2.30}$$

Now the algebraic Bernoulli equation can be written for the system in modal coordinates, looking for a relation between direct and adjoint modal coordinates

$$\boldsymbol{\lambda}_i = \mathcal{P}_{ij} \mathbf{x}_j = \mathcal{P}_{ij} \langle \mathbf{l}_j,\ \mathcal{E}\mathbf{x} \rangle_{L^2(\Omega)} \tag{2.31}$$

The same reasoning and formulae in [16] can now be applied to solve for $\mathcal{P}_{ij}$. Without loss of generality, the algebraic Bernoulli equation can be obtained by

---

[11] Assuming they are not degenerate; see the appendix in [101] for the degenerate case.

setting $\mathcal{C} = 0$ and $\mathbf{R} = \mathbf{I}$. The elements $\mathcal{P}_{ij}$ can be arranged in a matrix operator $\mathcal{P}$, whose inverse $\mathcal{F}$ satisfies the relation

$$\mathcal{F}_{ij} = [\mathcal{P}_{ij}]^{-1} = \frac{\langle \mathbf{l}_i,\, \mathcal{B}\rangle_{L^2(\Omega)}\langle \mathcal{B}^{\dagger^H},\, \mathbf{l}_j\rangle_{L^2(\Omega)}}{\sigma_i + \sigma_j^*} \tag{2.32}$$

and then the feedback law reads

$$\mathbf{u} = -\langle \mathcal{B}^{\dagger^H}, \mathbf{l}_i\rangle_{L^2(\Omega)}\boldsymbol{\lambda}_i = -\langle \mathcal{B}^{\dagger^H}, \mathbf{l}_i\rangle_{L^2(\Omega)}\mathcal{P}_{ij}\langle \mathbf{l}_j,\, \mathcal{E}\mathbf{x}\rangle_{L^2(\Omega)} \tag{2.33}$$

Thus, the expression for the feedback gains operator is

$$\mathcal{K}_{MEC} = -\langle \mathcal{B}^{\dagger^H}, \mathbf{l}_i\rangle_{L^2(\Omega)}\mathcal{P}_{ij}\mathbf{l}_j^H \tag{2.34}$$

So, having introduced a suitable space discretization (with a weight matrix M_Ω to perform discrete integration), the computation of $\mathcal{P}_{ij}$ requires only the computation of the unstable direct and adjoint eigenfunctions and the inversion of a matrix whose dimension is given by the number of unstable system eigenvalues.

2.4.2 The optimization framework: The adjoint of the direct-adjoint (Hamiltonian) system

The technique presented in sec. 2.4.1 is restricted to unstable systems and does not allow general ratios between state and control weights. A way to compute the feedback gains for the infinite time horizon control without solving the algebraic Riccati equation has been proposed by Pralits and Luchini [90] and further applied in [103]. The key idea is to go back to the infinite time horizon optimization setting, of which the Riccati equation is a particular way of expressing the solution.

We want to optimize the objective functional

$$\mathcal{J} = \frac{1}{2}\int_0^T \left(||\mathcal{C}\mathbf{x}||^2_{L^2(\Omega)} + ||\mathbf{D}\mathbf{u}||^2_2 \right) \mathrm{d}t \tag{2.35}$$

subject to

$$\begin{aligned} \mathcal{E}\frac{\partial \mathbf{x}}{\partial t} &= \mathcal{A}\mathbf{x} + \mathcal{B}\mathbf{u} && \text{in } \Omega, \quad t \in (0, T] \\ \mathcal{E}\mathbf{x}(0) &= \mathcal{E}\mathbf{x}_0 && \text{in } \Omega \end{aligned} \tag{2.36}$$

provided with suitable boundary conditions.

Standard optimization techniques allow to compute iteratively the optimal control $\mathbf{u}$ which minimize the objective functional $\mathcal{J}$ starting from an initial guess, but not the feedback gains. We are interested in them because we want to apply the linear control on the original, nonlinear system. Since feedback gains in the infinite time horizon setting are stationary, imposing as many independent initial conditions $\mathbf{Ex}_0^{(i)}$ as the number n of degrees of freedom we choose to retain in the discretization could allow to get the feedback gains as

$$\left[\mathbf{u}(0)^{(1)} \quad \dots \quad \mathbf{u}(0)^{(n)}\right] = \mathbf{K}\left[\mathbf{Ex}_0^{(1)} \quad \dots \quad \mathbf{Ex}_0^{(n)}\right] \tag{2.37}$$

provided with the adjoint boundary conditions. Such computation, however, is extremely cumbersome as it requires n independent optimization procedures.

An alternative approach, requiring only as many optimization procedures as the number m of control inputs (which, for a continuum system, are much less than the degrees of freedom), is based on the use of the adjoint variable. We have already seen how the Lagrange multipliers technique allows to define an adjoint variable $\boldsymbol{\lambda}$ subject to the problem

$$\begin{aligned} \mathcal{E}^\dagger \frac{\partial \boldsymbol{\lambda}}{\partial t} &= -\mathcal{A}^\dagger \boldsymbol{\lambda} - \mathcal{C}^\dagger \mathcal{C} \mathbf{x} && \text{in } \Omega, \quad t \in (T, 0] \\ \mathcal{E}^\dagger \boldsymbol{\lambda}(T) &= \mathcal{E}^\dagger \boldsymbol{\lambda}_T && \text{in } \Omega \end{aligned} \tag{2.38}$$

Again, since gains become stationary as $T \to +\infty$, we can evaluate the transversality/feedback relation (eq. 2.13) at the initial time

$$\mathbf{u}(0) = \int_\Omega \mathcal{K}\mathcal{E}\mathbf{x}_0 \, \mathrm{d}\Omega = -\mathbf{R}^{-1} \int_\Omega \mathcal{B}^\dagger \boldsymbol{\lambda}(0) \, \mathrm{d}\Omega \tag{2.39}$$

Evaluating this relation for each $i-\text{th}$ component of the control input $\mathbf{u}$

$$u_i(0) = \int_\Omega \mathcal{K}_i \mathcal{E}\mathbf{x}_0 \, \mathrm{d}\Omega = -\int_\Omega \left(\mathbf{R}^{-1}\mathcal{B}^\dagger\right)_i \boldsymbol{\lambda}(0) \, \mathrm{d}\Omega \tag{2.40}$$

we see that assigning the following initial and final conditions

$$\begin{aligned} \mathcal{E}\mathbf{x}_0 &= -\left(\mathcal{B}^{\dagger^H}\mathbf{R}^{-1}\right)_i \\ \mathcal{E}^\dagger \boldsymbol{\lambda}_T &= 0 \end{aligned} \tag{2.41}$$

we can compute the feedback operator for the $i-\text{th}$ component of the control input as

$$\mathcal{K}_i = \boldsymbol{\lambda}^H(0) \tag{2.42}$$

The computed feedback operator is optimal for every initial condition $\mathcal{E}\mathbf{x}_0$ and terminal condition $\mathcal{E}^\dagger \boldsymbol{\lambda}_T$. A particular choice is necessary only to allow us to compute $\mathcal{K}$ from the values assumed by the adjoint variable $\boldsymbol{\lambda}$ at time $t = 0$.

This procedures needs to be repeted only m times, and can benefit from the presence of symmetries in the problem. Each optimization step requires the subsequent integration of the direct and adjoint equations forward and backward in time, the evaluation of the objective functional and the update of $\mathbf{u}$ through a line minimization, until a specified tolerance (on the objective functional, the relative increment of the control or its gradient) is reached. At the end of the procedure, the feedback gains for each component of the control input can be computed by eq. 2.42. The time horizon for integration should be long enough for gains stationarity to be fulfilled.

The interpretation of the above technique in terms of adjoint of the Hamiltonian system is presented in the original works [90, 103].

3

Numerical formulation

In a given physical situation we feel certain in advance that the solution of a certain boundary value problem must exist since the physical quantity realised in nature is itself the desired solution. And thus we often encounter the expression: "We know for physical reasons that the solution exists." This expression is actually based on wrong premises. While we cannot doubt that a certain physical quantity realises the solution to a certain boundary value problem, we have no guarantee that the ***mathematical formulation*** *of that problem is correct to the last dot. We have neglected so many accessories of the problem, we have simplified so much on the given physical situation that we know in advance that the field equation with which we operate cannot be considered as the final truth.*

C. Lanczos, "Linear Differential Operators". 1960.

This chapter is devoted to the development of a suitable numerical formulation to be used for the solution of the control problems presented in chapter 2. First, the dimensionless parameters which characterize the problem are introduced (section 3.1) and the linearized flow model to be used in the control synthesis is derived (section 3.2); then the multidomain spectral discretization strategy is presented (section 3.3). Finally, several issues concerning the treatment of boundary and interface conditions are discussed (section 3.4) in order to motivate the development of the specific multidomain technique adopted in this work.

The numerical approximation of the general control techniques developed in chapter 2 is presented in section 3.6, and the interface between control programs and DNS solver is summarized in section 3.7.

3.1 Nondimensionalization

When dealing with incompressible flows with constant density $\bar{\rho}$ it is customary to redefine pressure as

$$p \equiv \frac{P}{\bar{\rho}} \tag{3.1}$$

Introducing the length, time and velocity scales $\mathcal{L}$, $\mathcal{T}$, $\mathcal{U}$, the dimensionless parameters characterizing the flow are the Strouhal and Reynolds numbers St and

Re defined as

$$\begin{aligned} St &\equiv \frac{\mathcal{L}}{\mathcal{U}\mathcal{T}} \\ Re &\equiv \frac{\mathcal{L}\mathcal{U}}{\nu} \end{aligned} \tag{3.2}$$

For each $j-\mathrm{th}$ porous layer the dimensionless permeability σ_j can be defined as

$$\sigma_j \equiv \frac{\sqrt{k_j}}{\mathcal{L}} \tag{3.3}$$

In this work, the length scale is set to be equal to the central channel half-height

$$\mathcal{L} = h \tag{3.4}$$

The choice of the velocity scale leads to different definitions of the Reynolds number. We get the *centerline Reynolds number* $Re_{\mathbb{C}}$ by choosing the mean turbulent velocity at the channel centerline as reference velocity

$$\mathcal{U} = \langle U_{\mathbb{C}} \rangle \tag{3.5}$$

We get the *Poiseuille Reynolds number* Re_P by choosing as reference velocity the centerline velocity of the laminar solution

$$\mathcal{U} = U_{\mathbb{C}} \tag{3.6}$$

We get the *bulk Reynolds number* by choosing as reference velocity the channel streamwise velocity averaged in the wall normal direction

$$\mathcal{U} = \frac{1}{2h} \int_{-h}^{h} U \,\mathrm{d}y \tag{3.7}$$

The time scale is chosen as

$$\mathcal{T} = \frac{\mathcal{L}}{\mathcal{U}} \tag{3.8}$$

in order to get $St = 1$. The requirement $St = 1$ makes the time scale dependent on the choice of the reference velocity: This must be kept in mind when comparing eigenvalues computed using different definitions of the Reynolds number, since they will be scaled accordingly.

3.2 Linearized flow model

Introducing the dimensionless reference states $(\mathbf{U}(y),\ P(y))$ and $(\langle \mathbf{U} \rangle_j(y),\ \langle P \rangle_j^f(y))$, solutions to the nonlinear problem (eq. 1.13) in the channel and porous layers

($j = 1, 2$) respectively, it is possible to decompose the nondimensional velocity and pressure into a reference and a perturbation part

$$\begin{aligned}
\mathbf{u} &= \mathbf{U}(y) + \mathbf{u}' \\
p &= P(y) + p' \\
\langle \mathbf{u} \rangle_j &= \langle \mathbf{U} \rangle_j(y) + \langle \mathbf{u} \rangle_j' \\
\langle p \rangle_j &= \langle P \rangle_j^f(y) + \langle p \rangle_j^{f\prime}
\end{aligned} \tag{3.9}$$

In this work, the reference state is the laminar solution used in [107], aligned with the x axis. Thanks to the small perturbation hypothesis, it is possible to derive a linear model for the state perturbations.

Dropping the apex from the notation for perturbations with a slight (but convenient) abuse of notation, we get the following nondimensional, linearized version of eq. 1.13

$$\begin{aligned}
\frac{\partial \mathbf{u}}{\partial t} - \frac{1}{Re}\nabla^2 \mathbf{u} + \mathbf{U}(y) \cdot \boldsymbol{\nabla} \mathbf{u} + \mathbf{u} \cdot \boldsymbol{\nabla} \mathbf{U}(y) + \boldsymbol{\nabla} p &= \mathbf{0} \\
\boldsymbol{\nabla} \cdot \mathbf{u} &= 0 & \text{in} \quad \Omega \\
\frac{1}{\epsilon_j}\frac{\partial \langle \mathbf{u} \rangle_j}{\partial t} + \frac{1}{\sigma_j^2 Re}\langle \mathbf{u} \rangle_j - \frac{1}{\epsilon_j Re}\nabla^2 \langle \mathbf{u} \rangle_j + \boldsymbol{\nabla} \langle p \rangle_j^f &= \mathbf{0} \\
\boldsymbol{\nabla} \cdot \langle \mathbf{u} \rangle_j &= 0 & \text{in} \quad \Omega_j \\
\langle \mathbf{u} \rangle_j &= 0 & \text{on} \quad \Gamma_{w,j} \\
\mathbf{u} &= \langle \mathbf{u} \rangle_j \\
p &= \langle p \rangle_j^f \\
\frac{1}{\epsilon_j}\frac{\partial \langle u \rangle_j}{\partial y} - \frac{\partial u}{\partial y} &= \mp \frac{\tau_j}{\sigma_j} u \\
\frac{1}{\epsilon_j}\frac{\partial \langle w \rangle_j}{\partial y} - \frac{\partial w}{\partial y} &= \mp \frac{\tau_j}{\sigma_j} w & \text{on} \quad \Gamma_{i,j}
\end{aligned} \tag{3.10}$$

Note that linearization has been necessary in the channel layer only, since equations for the porous layers are already linear thanks to the hypothesis of neglecting inertial effects in the porous regions. No modification of the boundary and interface conditions is required, since they are already linear.

3.3 Spectral discretization and multidomain formulation

In this section the discretization methods chosen to numerically approximate eq. 3.10 are introduced. Since each channel layer is governed by different equations coupled through interface conditions only, the discretization strategy have to manage the splitting of the flow domain in the wall-normal direction.

3.3.1 Multidomain strategy

In order to manage the complex interface conditions which couple flows across different layers, the differential problem has been numerically approximated by collocation of the strong form of eq. 3.10. This non-variational formulation allows to impose boundary and interface conditions by *patching* [18, 23]: Boundary and interface conditions are explicitly written as additional equations relating flow states on the boundary and interface nodes (a procedure referred to as *boundary bordering* - see section 3.4) with no need for the basis functions to implicitly satisfy them (*basis recombination*). The resulting discrete model is rather flexible and allows to implement different boundary and interface conditions with no need for a change of basis functions. Standard techniques for multidomain solution strategies (such as the Schur complement technique [23]) and for systems of differential-algebraic equations [4] can then be used for stability analysis and time integration, which are the basic tools of optimal control.

3.3.2 Wall-parallel directions

As there is no flow coupling in the streamwise and spanwise directions, in each layer the flow state can be expanded by means of the Fourier series

$$
\begin{aligned}
\mathbf{u}(x,y,z,t) &= \sum_{\kappa_x,\kappa_z} \hat{\mathbf{u}}(\kappa_x,y,\kappa_z,t)e^{i\kappa_x x+i\kappa_z z}\\
p(x,y,z,t) &= \sum_{\kappa_x,\kappa_z} \hat{p}(\kappa_x,y,\kappa_z,t)e^{i\kappa_x x+i\kappa_z z}\\
\langle\mathbf{u}\rangle_j(x,y,z,t) &= \sum_{\kappa_x,\kappa_z} \langle\hat{\mathbf{u}}\rangle_j(\kappa_x,y,\kappa_z,t)e^{i\kappa_x x+i\kappa_z z}\\
\langle p\rangle_j^f(x,y,z,t) &= \sum_{\kappa_x,\kappa_z} \langle\hat{p}\rangle_j^f(\kappa_x,y,\kappa_z,t)e^{i\kappa_x x+i\kappa_z z}
\end{aligned}
\tag{3.11}
$$

with $\kappa_x = \frac{2\pi n_x}{L_x}$, $n_x = -N_x, \ldots, N_x$ and $\kappa_z = \frac{2\pi n_z}{L_z}$, $n_z = -N_z, \ldots, N_z$. This is a standard choice for an efficient treatment of the spatially invariant, wall-parallel directions for wall-bounded flows [101].

The employment of the Fourier series leads to a spectral Bubnov-Galerkin formulation [18], which allows to exploit the advantages of spectral accuracy while fully decoupling the problem in wavenumber space [101]. The differential operators in the x and z directions are transformed into algebraic operators, with the nabla operator defined in wavenumber space as

$$\hat{\boldsymbol{\nabla}} \equiv \begin{pmatrix} i\kappa_x \\ \frac{\partial}{\partial y} \\ i\kappa_z \end{pmatrix} \tag{3.12}$$

As discussed in chapter 2, the optimal control problem can thus be solved independently for each wavenumber pair.
The linear model equations for each wavenumber pair read

$$\begin{aligned}
\frac{\partial \hat{\mathbf{u}}}{\partial t} - \frac{1}{Re}\hat{\nabla}^2 \hat{\mathbf{u}} + \mathbf{u}_0 \cdot \hat{\boldsymbol{\nabla}} \hat{\mathbf{u}} + \hat{\mathbf{u}} \cdot \hat{\boldsymbol{\nabla}} \mathbf{u}_0 + \hat{\boldsymbol{\nabla}} \hat{p} &= \mathbf{0} \\
\hat{\boldsymbol{\nabla}} \cdot \hat{\mathbf{u}} &= 0 && \text{in} \quad \Omega \\
\frac{1}{\epsilon_j}\frac{\partial \langle \hat{\mathbf{u}} \rangle_j}{\partial t} + \frac{1}{\sigma_j^2 Re}\langle \hat{\mathbf{u}} \rangle_j - \frac{1}{\epsilon_j Re}\hat{\nabla}^2 \langle \hat{\mathbf{u}} \rangle_j + \hat{\boldsymbol{\nabla}} \langle \hat{p} \rangle_j^f &= \mathbf{0} \\
\hat{\boldsymbol{\nabla}} \cdot \langle \hat{\mathbf{u}} \rangle_j &= 0 && \text{in} \quad \Omega_j \\
\langle \hat{\mathbf{u}} \rangle_j &= 0 && \text{on} \quad \Gamma_{w,j} \\
\hat{\mathbf{u}} &= \langle \hat{\mathbf{u}} \rangle_j \\
\hat{p} &= \langle \hat{p} \rangle_j^f \\
\frac{1}{\epsilon_j}\frac{\partial \langle \hat{u} \rangle_j}{\partial y} - \frac{\partial \hat{u}}{\partial y} &= \mp \frac{\tau_j}{\sigma_j}\hat{u} \\
\frac{1}{\epsilon_j}\frac{\partial \langle \hat{w} \rangle_j}{\partial y} - \frac{\partial \hat{w}}{\partial y} &= \mp \frac{\tau_j}{\sigma_j}\hat{w} && \text{on} \quad \Gamma_{i,j}
\end{aligned} \tag{3.13}$$

3.3.3 Wall-normal direction

To fully exploit the advantages of spectral methods for collocation of eq. 3.13 in the wall-normal direction, a Chebyshev cardinal functions series expansion [18, 22] is employed for each Fourier coefficient

$$\begin{aligned}
\hat{\mathbf{u}}(\kappa_x, y, \kappa_z, t) &= \sum_{i=0}^{N_y-1} C_i(y)\hat{\mathbf{u}}_i(\kappa_x, \kappa_z, t) \\
\hat{p}(\kappa_x, y, \kappa_z, t) &= \sum_{i=0}^{N_y-1} C_i(y)\hat{p}_i(\kappa_x, \kappa_z, t) \\
\langle\hat{\mathbf{u}}\rangle_j(\kappa_x, y, \kappa_z, t) &= \sum_{i=0}^{N_{y_j}-1} C_i(y)\langle\hat{\mathbf{u}}_i\rangle_j(\kappa_x, \kappa_z, t) \\
\langle\hat{p}\rangle_j^f(\kappa_x, y, \kappa_z, t) &= \sum_{i=0}^{N_{y_j}-1} C_i(y)\langle\hat{p}_i\rangle_j^f(\kappa_x, \kappa_z, t)
\end{aligned} \tag{3.14}$$

where a different number of polynomials and collocation nodes in each channel layer is possible.

This allows to express the first and second order derivatives $\frac{\partial}{\partial y}$ and $\frac{\partial^2}{\partial y^2}$ as the matrix operators $\mathbf{D}^{(1)}$ and $\mathbf{D}^{(2)}$ (see appendix A) and to fully discretize the problem for each wavenumber pair.

3.4 Boundary and interface conditions treatment

The treatment of boundary conditions has shown to be the most delicate part in the collocation scheme. *Basis recombination* and *boundary bordering* are the two main families of techniques used to incorporate boundary conditions in the pseudospectral discretization of a boundary value problem [18]. The former technique aims to the construction of a set of basis functions which implicitly satisfy boundary conditions, while the latter uses a set of basis functions with unprescribed boundary values and incorporates boundary conditions through algebraic equations relating the evaluation of the solution on boundary nodes.

The two approaches have been shown to be equivalent for linear problems [59]. A main difference between them is that, when dealing with dynamical problems, the former approach usually leads to state-space (nonsingular) systems, while the latter, due to the explicit presence of algebraic boundary conditions, leads to descriptor (singular) systems. Since most of the standard tools of linear control theory has been developed for state-space systems, many works in flow control have focused on reducing the system to a state-space form.

In this work, the correct treatment of boundary conditions is even more essential since it is necessary to properly handle the interface conditions among flows in

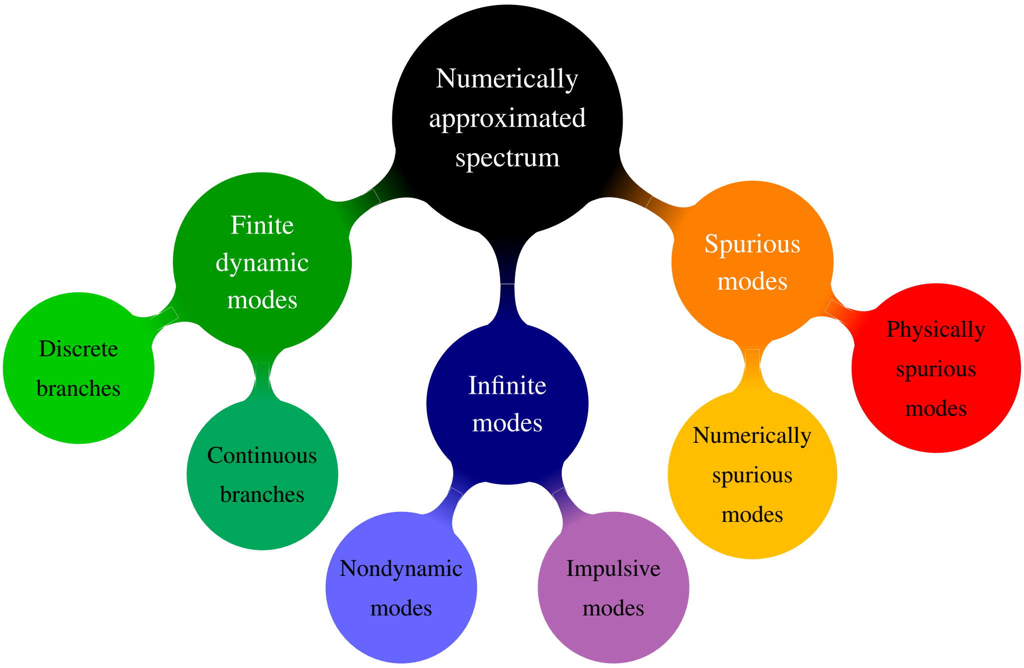

Figure 3.1: Classification of numerically approximated eigenvalues and eigenvectors.

different channel layers also.
For linear systems, the stability analysis (and hence, a correct eigenanalysis) is a prerequisite for the analysis and design of control systems. Before introducing several different treatments of boundary conditions, then, the properties of the numerical approximated spectrum of a linear system are presented and it is explained how an inconsistent treatment of boundary and interface conditions can spoil the computation.

3.4.1 Finite, infinite and spurious modes

The numerical approximation of the spectrum of a linear system of differential-algebraic equations, arising from a truly discrete problem (a chemical plant, a hydraulic or electrical network) or from the discretization of a continuum one (as the Navier-Stokes equations for incompressible flows) either, can be subdivided into three main families of modes [10, 18] (see fig. 3.1).

Finite dynamic modes have finite eigenvalues and are responsible for the causal dynamical behaviour of the system. If the model system is the discretization of a continuum system, finite modes can have continuous branches [101] in addition to discrete modes.

Infinite modes have infinite eigenvalues and are originated from the presence of the algebraic equations. They fall into two categories. *Nondynamic modes*, which are as many as the number of algebraic equations and are associated with system directions in which there is a purely algebraic input-output relation, and *dynamics modes at* ∞ (or *impulsive modes*) associated with directions in which the system can exhibit impulsive behaviour due only to an initial (possibly smooth) condition with zero control input. Their presence allows descriptor systems to assume an anticausal behaviour, developing impulses and derivatives of the impulse in the time response[1]. This behaviour is related to the concept of *consistent initial conditions*: For a descriptor linear system to develop a causal time response, the initial condition must satisfy the algebraic constraints of the system. If we want to compute the system response from an arbitrary, inconsistent initial condition we must allow the system to develop distributional, anticausal solutions [32].

Spurious modes arise from the numerical discretization of a continuum system. They can be classified into *numerically spurious modes*, which simply are numerically underresolved modes (and they often constitute as much as half of the whole discretized spectrum [18]), and *physically spurious modes*, which arise from an inconsistent treatment of boundary conditions [18]. While numerically spurious modes are not an issue, since the contribution of underresolved modes to the system dynamical behaviour is generally negligible, physically spurious modes are a serious danger to dynamical analyses since their eigenvalues may have high real part, so they are likely to significantly spoil the stability properties of the system (and to blow up any attempted time integration).

Since the work of Orszag [87] on linear stability of plane channel flow, spectral approximations of the Orr-Sommerfeld stability equation have often been affected by the presence of physically spurious modes [18, 23, 79, 56, 31, 75]. This is due to an inconsistent treatment of the homogeneous Neumann conditions on normal velocity in wavenumber space

$$\left.\frac{\partial \hat{v}}{\partial y}\right|_{\Gamma_w} = 0 \tag{3.15}$$

which are a consequence of the evaluation of the incompressibility constraint on

---

[1] For a complete derivation of distributional solutions for linear descriptor systems, see the book of Duan [32].

solid walls

$$(\boldsymbol{\nabla} \cdot \mathbf{u})|_{\Gamma_w} = 0 \tag{3.16}$$

The second order differential operator at the left hand side of the Orr-Sommerfeld equation requires the Dirichlet conditions only (two conditions, one for each wall) in order to be inverted, while the fourth order differential operator at the right hand side requires both the Dirichlet and the Neumann conditions (four conditions) [18]. In Chebyshev spectral discretizations, the imposition of both the Dirichlet and Neumann conditions on both the left and right hand side of the Orr-Sommerfeld equation has been shown to lead to physically spurious modes [30], while Legendre polynomials produce two infinite eigenvalues. A correct treatment of boundary conditions would require the reduction of the fourth order problem to a system of two second order problems, through the introduction of an auxiliary variable $\hat{\xi} \equiv \hat{\nabla}^2 \hat{v}$ [31]. Then the Neumann conditions on velocity can be used to implicitly define the boundary conditions for $\hat{\xi}$, producing a differential problem that is not overdetermined anymore. This situation is encountered in primitive variables formulations also, where pressure is not provided with a proper boundary condition on solid walls [18, 94]; again, the evaluation of the incompressibility constraint on the solid boundary can implicitly provide the boundary values for the Poisson pressure equation derived from the linearized Navier-Stokes momentum and continuity equations (see section 3.4.4). In the next sections some troubles with the numerical formulations adopted in the previous works on channel flow through porous walls are presented, together with the discretization technique adopted in this work (section 3.4.5).

3.4.2 Singular perturbations techniques

Schmid and Henningson proposed a *boundary bordering* collocation scheme based on Chebyshev polynomials to be applied on the Orr-Sommerfeld and Squire equations [101], also extended by Tilton and Cortelezzi [107] for the linear stability analysis of channel flow through porous walls and used by Scarselli [100] for the transient energy growth analysis of the same problem.

The technique consists in collocating the differential equations on the internal nodes, collocating the Dirichlet conditions on the boundary nodes, and then substituting the matrix rows corresponding to the collocation of the Orr-Sommerfeld equation on the next-to-boundary nodes with the Neumann conditions on velocity. All the algebraic boundary conditions are replaced with singular perturbations

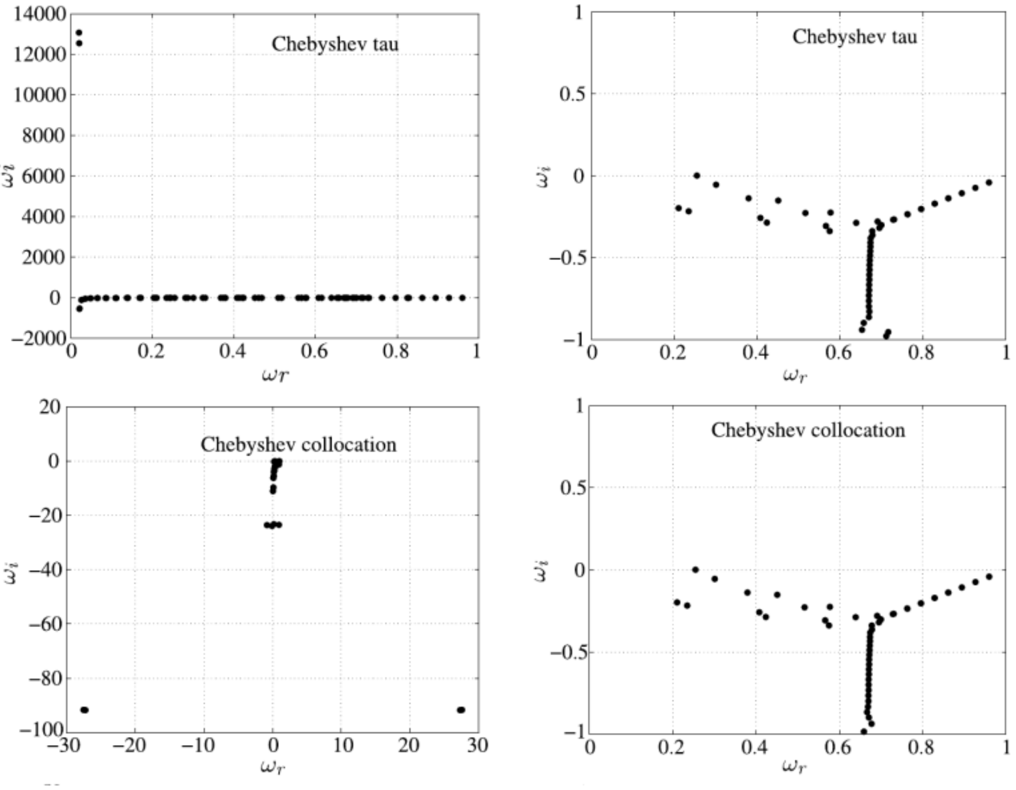

Figure 3.2: Comparison between spectra of the Orr-Sommerfeld equation for the wavenumber pair $(1, 0.25)$ at $Re_P = 7500$ computed with the Chebyshev-tau method [87] and the Chebyshev collocation scheme of Schmid and Henningson [101] using $N = 100$ polynomials (from [101]). On the left the whole computed spectrum is shown, while on the right only the least stable, physically relevant part is shown. In the former scheme the spurious eigenvalues appear with a high real part $\Re(\sigma) = \omega_i \kappa_x$, while in the latter they appear with a high imaginary part $\Im(\sigma) = -\omega_r \kappa_x$.

equations of the kind

$$\begin{aligned} -m \left.\frac{\partial v}{\partial t}\right|_w &= v|_w \qquad m \ll 1 \\ -m \left.\frac{\partial \eta}{\partial t}\right|_w &= \eta|_w \\ -m \left.\frac{\partial v}{\partial t}\right|_w &= \left.\frac{\partial v}{\partial y}\right|_w \end{aligned} \tag{3.17}$$

in order to desingularize the problem.

Singular perturbations avoid the appearance of *infinite* eigenvalues, but they are not effective against *physically spurious* eigenvalues. Moreover, this tech-

nique introduce an inconsistency since some collocation points are discarded in favor of other conditions. Examination of the whole spectrum (fig. 3.2) reveals a large spread from the real axis (with the convention used in the figure, the imaginary axis), although no physically spurious eigenvalue appears; figure 3.3 shows a comparison between spectra computed with Schmid and Henningson's technique and the descriptor Kleiser-Schumann technique (presented in section 3.4.5). When extending the singular perturbation technique to the imposition of interface conditions in plane channel flow with permeable walls [107, 100], physically spurious eigenvalues with high real part may appear depending on the numerical values of the parameters of the permeable layers. Since physically spurious eigenvalues spoil the system response and optimal control strongly depends on the discretized adjoint problem, this formulation is inadmissible for dynamical analyses. Thus, it has been discarded in the present work.
Further inconsistencies in the discrete adjoint operator are revealed by the examination of left eigenvectors[2], both for the impermeable and permeable case (figures 3.4, 3.5). All of them exhibit an highly oscillatory behaviour and do not respect the adjoint boundary conditions on normal velocity and vorticity (which are the same as the direct ones for the impermeable case, as shown in [101]; the permeable case is discussed in appendix C).

3.4.3 Modified basis functions techniques

Physically spurious modes of the Orr-Sommerfeld equation are similar to the spurious pressure modes occurring in the primitive variables formulation of incompressible flows. In spectral discretizations it is common practice to satisfy the inf-sup compatibility condition by approximating pressure with polynomials whose degree is two less than that of velocity [18, 23].

Similarly, McFadden, Murray and Boisvert [79] proposed to neglect the two highest order polynomials from the discretization of the left hand side (LHS) of the Orr-Sommerfeld equation by the Chebyshev tau method, in order to impose homogeneous Neumann conditions on the right hand side (RHS) only. Their technique is exact for the one-dimensional incompressible flow model; for the

---

[2] Left eigenvectors (discrete adjoint approach) are related to the discretization of the adjoint eigenfunctions (continuous adjoint approach) by a linear transformation through the integration weight matrix [68].

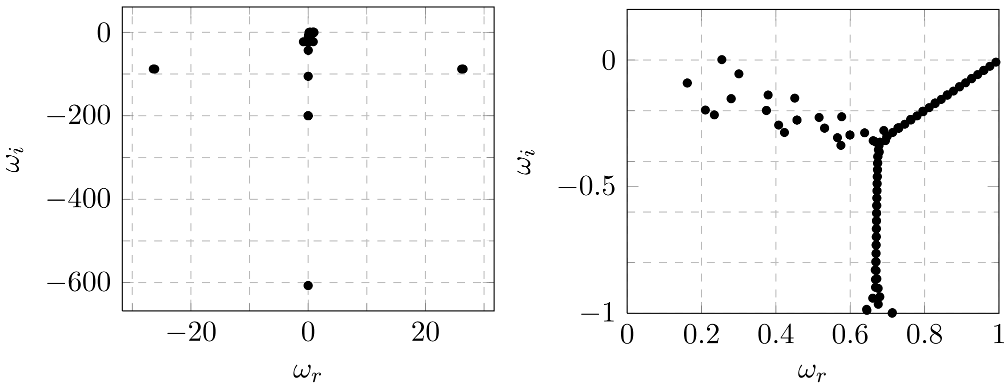

(a) Whole spectrum (singular perturbations).

(b) Physically relevant part (singular perturbations).

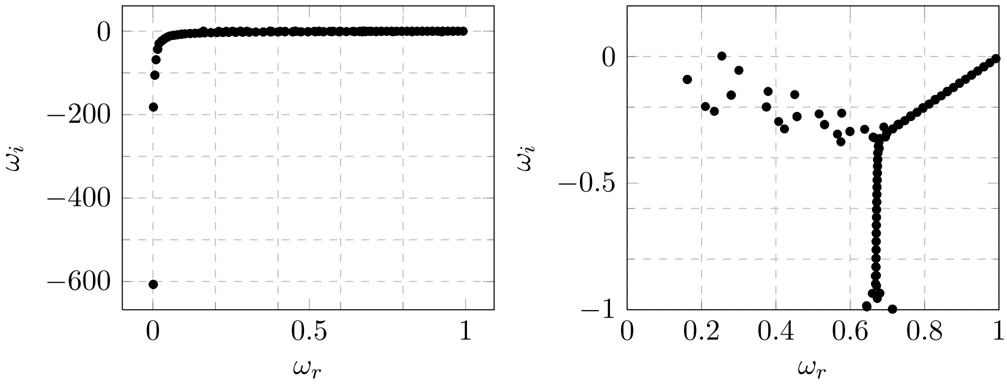

(c) Whole spectrum (descriptor Kleiser-Schumann).

(d) Physically relevant part (descriptor Kleiser-Schumann).

Figure 3.3: Comparison between the Orr-Sommerfeld and Squire spectrum computed by the Chebyshev collocation scheme of Schmid and Henningson (top figures) and the Kleiser-Schumann technique in descriptor form using primitive variables (bottom figures) of sec. 3.4.5. The same parameters $Re_P = 7500$, $(\kappa_x, \kappa_z) = (1, 0.25)$, $N = 100$ and the convention $\Re(\sigma) = \omega_i \kappa_x$, $\Im(\sigma) = -\omega_r \kappa_x$ are used to facilitate comparisons with fig. 3.2. No spreading of the spectrum is observed when using the Kleiser-Schumann technique, and physically spurious eigenvalues do not appear.

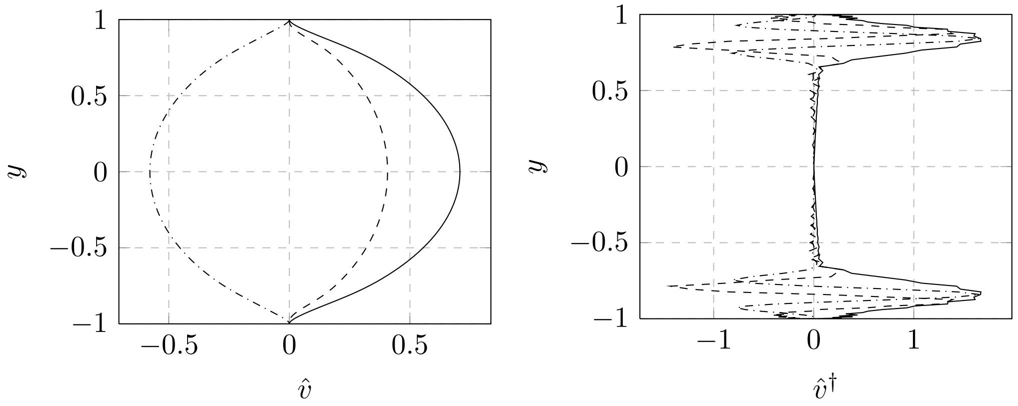

(a) Direct velocity eigenfunction. (b) Adjoint velocity eigenfunction.

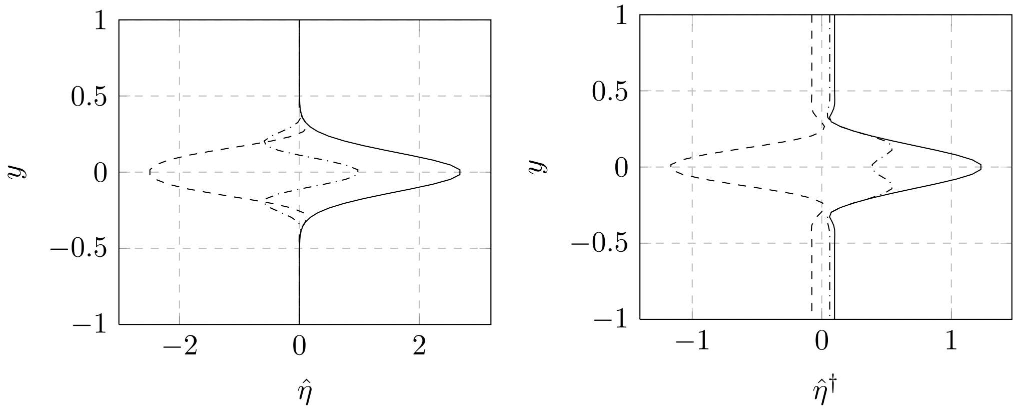

(c) Direct vorticity eigenfunction. (d) Adjoint vorticity eigenfunction.

Figure 3.4: Direct and (discrete) adjoint eigenfunctions of the first Orr-Sommerfeld (top) and Squire (bottom) modes, computed by the Chebyshev collocation scheme of Schmid and Henningson, for the same case of fig. 3.2 and 3.3. Dashed line is real part, dash-dotted line is imaginary part, solid line is absolute value. Inconsistencies in the discrete adjoint are apparent from the oscillations of adjoint velocity (which are persistent to grid refinement) and the inhomogeneous boundary values of adjoint vorticity.

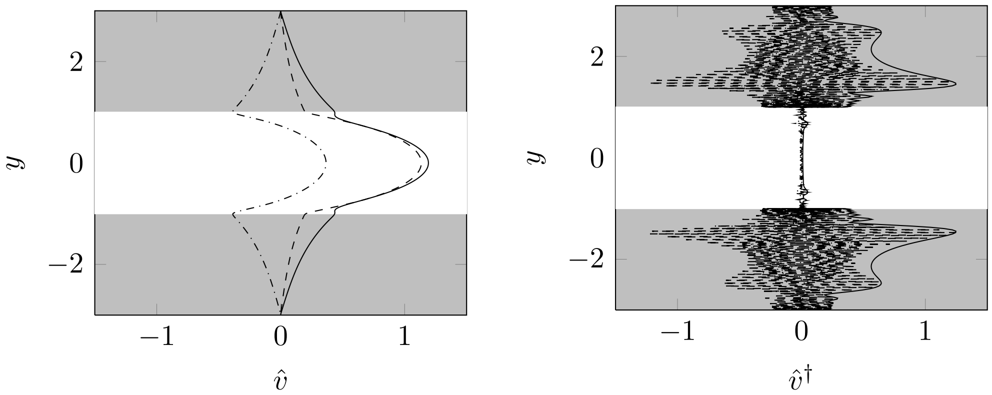

(a) Direct velocity eigenfunction. (b) Adjoint velocity eigenfunction.

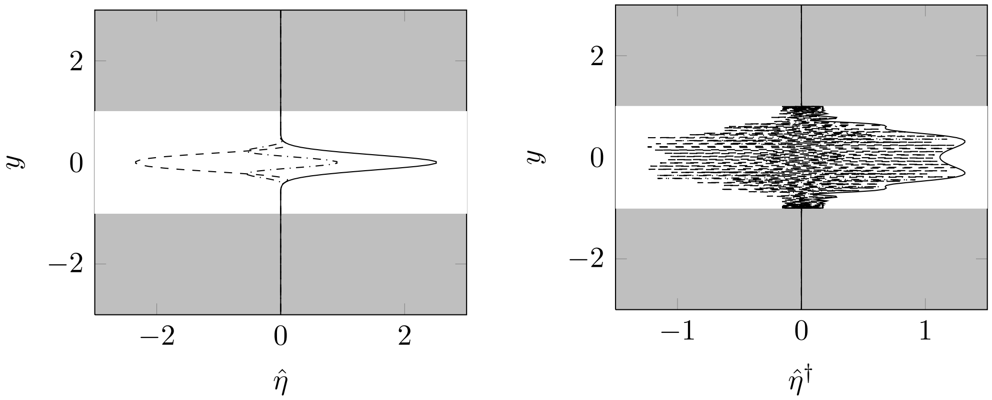

(c) Direct vorticity eigenfunction. (d) Adjoint vorticity eigenfunction.

Figure 3.5: Direct and (discrete) adjoint eigenfunctions of the first Orr-Sommerfeld (top) and Squire (bottom) modes for plane channel with permeable wall, computed by the Chebyshev collocation scheme of Schmid and Henningson. Porous layer are symmetric, the case is $Re_b = 2000$, $(\kappa_x, \kappa_z) = (1, 0)$, $\sigma = 0.02$, $\epsilon = 0.6, \tau = 0, h = 1$ (as in figure 5 of [107]), with $N = 100$ in all layers. Dashed line is real part, dash-dotted line is imaginary part, solid line is absolute value. Inconsistencies in the discrete adjoint are apparent from the discontinuity of adjoint variables through the interfaces, the inhomogeneous boundary values and the oscillations near the boundaries.

Orr-Sommerfeld equation their technique is not exact anymore, but the numerical error is small and can be estimated.

Huang and Sloan [56] proposed an analogous technique for Chebyshev cardinal functions. Their strategy consists in discretizing the left and the right hand sides of the equation with different basis functions, each satisfying the correct number of boundary conditions to be imposed [56, 18]. So, the LHS is discretized with the standard Chebyshev cardinal functions $C_j(y)$ (see appendix A) while the RHS is discretized with modified cardinal functions $h_j(y)$ which automatically satisfy homogeneous Neumann conditions (basis recombination)

$$h_j(y) \equiv \frac{1-y^2}{1-y_j^2} C_j(y) \tag{3.18}$$

The boundary nodes are discarded to impose homogeneous Dirichlet conditions (boundary bordering). It has been noted some disagreement on whether the modified basis function should be used for all the RHS or for the fourth order derivative only: Huang and Sloan used it for all the RHS, while the implementation found in Weiderman and Reddy's Matlab Differentiation Matrix Suite [110] use ”clamped” boundary conditions on the fourth order derivative only; McKernan [80] also studied the usage of modified basis functions and advocated their application for the discretization of all the RHS.

When dealing with coupled flow problems, the extension of these techniques should be carefully addressed. It the present work, it has been found that McFadden, Murray and Boisvert's technique is not generalizable, since coefficients of the highest order polynomials in each subdomain are coupled with coefficients of polynomials in other subdomains and cannot be neglected. The application of Huang and Sloan's modified cardinal functions has been tried, adopting a lifting procedure in each channel layer in order to apply homogeneous Neumann conditions on velocity at the interfaces also; boundary and interface conditions have been imposed algebraically, leading to an index 2 DAE system which can be reduced to normal (state-space) form [4]. The resulting system, however, is still affected by the presence of two high real part physically spurious eigenvalues and cannot be used for dynamical analyses.

3.4.4 Influence matrix (Schur complement) method

A widely adopted technique to impose boundary conditions in the direct numerical simulation of plane channel flow with the Chebyshev tau method is the *influence matrix* method, used by Kleiser and Schumann (see [23]) with primitive variables and by Kim, Moin and Moser [64] with a normal velocity-normal vorticity formulation. In normal velocity - normal vorticity formulations, the fourth order velocity equation is first reduced to two second order equations through the introduction of an auxiliary variable $\hat{\xi} \equiv \hat{\nabla}^2 \hat{v}$ (as it has been advocated for stability analyses also [31]). At each time step, linearity is leveraged to solve the problem for arbitrary boundary values of the auxiliary variables; then, boundary values of the auxiliary variable are computed to satisfy homogeneous Neumann conditions on velocity, solving a linear system by the inversion of a so-called *influence matrix*[3].

In the primitive variables formulation, the same algorithm can be used to derive pressure boundary conditions from the Neumann conditions on normal velocity, once a Poisson equation for pressure equation has been analytically derived. Solution of the time-discretized momentum equation together with the Poisson equation for pressure

$$\begin{aligned} \left(-\hat{\nabla}^2 + \lambda\right) \hat{\mathbf{u}} + \hat{\boldsymbol{\nabla}} \hat{p} &= \hat{\mathbf{b}} \\ \hat{\nabla}^2 \hat{p} &= \hat{\boldsymbol{\nabla}} \cdot \hat{\mathbf{b}} \end{aligned} \tag{3.19}$$

(having denoted λ as a coefficient determined by the time scheme and $\hat{\mathbf{b}}$ as a generic right hand side) fulfills the incompressibility constraint $\hat{\nabla} \cdot \hat{\mathbf{u}} = 0$ only when the evaluation of the continuity constraint on the boundary

$$\left(\hat{\nabla} \cdot \hat{\mathbf{u}}\right)\Big|_{\Gamma_w} = 0 \tag{3.20}$$

is imposed as boundary condition to implicitly define the pressure boundary values [94]. In fact, taking the divergence of the momentum equations it can be shown that the system of equations 3.19 only imposes that $\hat{\nabla} \cdot \hat{\mathbf{u}}$ is harmonic at each time step: To make a harmonic function vanish in all the domain, it is sufficient to set its boundary value to zero.

For spectral approximations of plane channel flow (where the problem is one-dimensional after Fourier decomposition), stability and convergence of the method have been demonstrated [21].

The Kleiser-Schumann method can be recognized as the Schur complement method used in multidomain and domain decomposition problems [23]. Nodal values of the unknown in the internal grid points can be expressed as functions

---

[3] Only the essential features of the Kleiser-Schumann method are presented here. For implementation details, see [23, 64, 94].

of the nodal values on the interfaces, and a linear system for the values of the unknown on the interface can be assembled using the Schur complement matrix; the technique amounts to a block Gaussian elimination, but relies on the theory of Steklov-Poincaré interface operator [23]. While in domain decomposition problems the Schur complement is used to reduce the full system to a system for the unknown interface values only, in the Kleiser-Schumann method the Schur complement is used to obtain a system for the unknown internal values only.

The possibility to apply the Schur complement method to stability analysis and its flexibility in handling more general boundary conditions have been recognized in the magnetohydrodynamics community, where non-trivial boundary conditions often occur. The method has been successfully applied first to magnetohydrodynamic [92] and then to classical hydrodynamic [44] stability problems, without the appearance of any physically spurious mode. In these works it has been remarked that the application of an algebraic constraint to an evolutionary problem through the Schur complement technique naturally (and correctly) leads to a singular descriptor systems, with as many infinite eigenvalues as the number of implicit boundary conditions; the imposition of the same constraint on the time derivative of the state variable leads to a nonsingular descriptor system, but makes the ”stiffness” matrix singular: This phenomenon is known as *drift* in the multibody dynamics community, and in the works [44, 92] it has been circumvented by shifting the zero eigenvalues.

When dealing with singular descriptor systems, the continuous adjoint method is required. Since the analytical derivation of the adjoint interface conditions is much more meaningful in the primitive variables formulation than in the normal velocity-normal vorticity ones (see appendix B), for the present work a primitive variables formulation has been adopted.

The pressure equation has been derived taking the divergence of the momentum equation and imposing $\hat{\boldsymbol{\nabla}} \cdot \hat{\mathbf{u}} = 0$. Usually, the Poisson pressure equation is derived imposing the constraint time derivative $\frac{\partial}{\partial t}\left(\hat{\boldsymbol{\nabla}} \cdot \hat{\mathbf{u}}\right) = 0$ also. The resulting equation for pressure, however, is not equivalent to the incompressibility constraint: It only guarantees that $\hat{\boldsymbol{\nabla}} \cdot \hat{\mathbf{u}}$ satisfies a Helmholtz equation, even if incompressibility is imposed on the solid boundary. Eigenfunctions clearly do not satisfy incompressibility. The solution satisfies the incompressibility constraint only if the initial condition does so.

Instead, if the time derivative is retained in the pressure equation then this is equivalent to imposing that $\hat{\boldsymbol{\nabla}} \cdot \hat{\mathbf{u}}$ is harmonic, and the evaluation of the incompressibility constraint on the solid boundary is sufficient to guarantee incompressibility in all the domain.

In cartesian coordinates, the resulting system of equations in wavenumber space (denoting $\alpha \equiv \kappa_x$ and $\beta \equiv \kappa_z$ for convenience of notation) is composed by the linearized Navier-Stokes momentum and Poisson pressure equation

$$\begin{aligned}
\frac{\partial \hat{u}}{\partial t} - \frac{1}{Re}\left(\frac{\partial^2}{\partial y^2} - \kappa^2\right)\hat{u} + i\alpha U(y)\hat{u} + U'(y)\hat{v} + i\alpha\hat{p} = 0 \\
\frac{\partial \hat{v}}{\partial t} - \frac{1}{Re}\left(\frac{\partial^2}{\partial y^2} - \kappa^2\right)\hat{v} + i\alpha U(y)\hat{v} + \frac{\partial \hat{p}}{\partial y} = 0 \\
\frac{\partial \hat{w}}{\partial t} - \frac{1}{Re}\left(\frac{\partial^2}{\partial y^2} - \kappa^2\right)\hat{w} + i\alpha U(y)\hat{w} + i\beta\hat{p} = 0 \\
\frac{\partial}{\partial t}\left(i\alpha\hat{u} + \frac{\partial}{\partial y}\hat{v} + i\beta w\right) + \left(\frac{\partial^2}{\partial y^2} - \kappa^2\right)\hat{p} + 2i\alpha U'(y)\hat{v} = 0
\end{aligned} \tag{3.21}$$

and the Volume Averaged Navier-Stokes momentum equation and Poisson pressure equation in each porous layer

$$\begin{aligned}
\frac{1}{\epsilon_j}\frac{\partial\langle\hat{u}\rangle_j}{\partial t} + \frac{1}{\sigma_j^2 Re}\langle\hat{u}\rangle_j - \frac{1}{\epsilon_j Re}\left(\frac{\partial^2}{\partial y^2} - \kappa^2\right)\langle\hat{u}\rangle_j + i\alpha\langle\hat{p}\rangle_j^f = 0 \\
\frac{1}{\epsilon_j}\frac{\partial\langle\hat{v}\rangle_j}{\partial t} + \frac{1}{\sigma_j^2 Re}\langle\hat{v}\rangle_j - \frac{1}{\epsilon_j Re}\left(\frac{\partial^2}{\partial y^2} - \kappa^2\right)\langle\hat{v}\rangle_j + \frac{\partial\langle\hat{p}\rangle_j^f}{\partial y} = 0 \\
\frac{1}{\epsilon_j}\frac{\partial\langle\hat{w}\rangle_j}{\partial t} + \frac{1}{\sigma_j^2 Re}\langle\hat{w}\rangle_j - \frac{1}{\epsilon_j Re}\left(\frac{\partial^2}{\partial y^2} - \kappa^2\right)\langle\hat{w}\rangle_j + i\beta\langle\hat{p}\rangle_j^f = 0 \\
\frac{\partial}{\partial t}\left(i\alpha\langle\hat{u}\rangle_j + \frac{\partial}{\partial y}\langle\hat{v}\rangle_j + i\beta\langle\hat{w}\rangle_j\right) + \left(\frac{\partial^2}{\partial y^2} - \kappa^2\right)\langle\hat{p}\rangle_j^f = 0
\end{aligned} \tag{3.22}$$

provided with the evaluation of the incompressibility constraint on solid walls and interfaces. Additional patching conditions are required at the interfaces: These conditions are the same derived for normal velocity from the momentum jump conditions in appendix C.

3.4.5 Descriptor system: Kleiser-Schumann method *without* influence matrix

Since the reduced system is singular, this situation can be exploited to avoid block Gaussian elimination and work with the original descriptor system directly. Implementation is straightforward, and numerical integration in time can be performed on DAE systems employing L-stable methods [76].

The linearized equations in primitive variables 3.10 are discretized by collocation with Chebyshev cardinal functions on a Gauss-Lobatto grid defined on each channel layer (explicit expressions for the discretization matrices and the domain mapping in the porous regions are given in appendix A).

The aim of the procedure is to obtain a numerical discretization of the descriptor linear system 2.10

$$\mathbf{E}_s\dot{\mathbf{x}}_s = \mathbf{A}_s\mathbf{x}_s + \mathbf{B}_s\mathbf{u} \tag{3.23}$$

which is composed by the *discretization* of the infinite-dimensional coupled flow system, the *discrete* boundary control dynamical equations and the *algebraic* boundary and interface conditions (imposed by *boundary bordering*)

$$\overbrace{\begin{bmatrix}\mathbf{E} & \mathbf{EG}\\ \mathbf{0} & m_1\mathbf{I}\end{bmatrix}}^{\mathbf{E}_s}\overbrace{\begin{bmatrix}\dot{\mathbf{x}}_0\\ \dot{\boldsymbol{\phi}}\end{bmatrix}}^{\dot{\mathbf{x}}_s} = \overbrace{\begin{bmatrix}\mathbf{A} & \mathbf{AG}\\ \mathbf{0} & m_0\mathbf{I}\end{bmatrix}}^{\mathbf{A}_s}\overbrace{\begin{bmatrix}\mathbf{x}_0\\ \boldsymbol{\phi}\end{bmatrix}}^{\mathbf{x}_s} + \overbrace{\begin{bmatrix}\mathbf{0}\\ \mathbf{I}\end{bmatrix}}^{\mathbf{B}_s}\mathbf{u} \tag{3.24}$$

The state and input vectors can be further decomposed into the contributions brought by each channel layer

$$\mathbf{x}_0 = \begin{bmatrix}\mathbf{x}_0^u\\ \mathbf{x}_0^c\\ \mathbf{x}_0^l\end{bmatrix} \qquad \boldsymbol{\phi} = \begin{bmatrix}\hat{\phi}^u\\ \hat{\phi}^l\end{bmatrix} \qquad \mathbf{u} = \begin{bmatrix}u^u\\ u^l\end{bmatrix} \tag{3.25}$$

as well as the discretized flow system matrices

$$\mathbf{E} = \left[\begin{array}{ccc}\mathbf{E}^u & 0 & 0\\ 0 & \mathbf{E}^c & 0\\ 0 & 0 & \mathbf{E}^l\\ \hdashline 0 & 0 & 0\end{array}\right] \qquad \mathbf{A} = \left[\begin{array}{ccc}\mathbf{A}^u & 0 & 0\\ 0 & \mathbf{A}^c & 0\\ 0 & 0 & \mathbf{A}^l\\ \hdashline \mathbf{A}^u_{BICs} & \mathbf{A}^c_{BICs} & \mathbf{A}^l_{BICs}\end{array}\right] \qquad \mathbf{G} = \left[\begin{array}{c}\mathbf{G}^u\\ \mathbf{0}\\ \mathbf{G}^l\\ \hdashline \mathbf{0}\end{array}\right] \tag{3.26}$$

bordered with the algebraic boundary and interface conditions.

The state in each channel layer can finally be decomposed into the cartesian velocity components and the pressure parts

$$\mathbf{x}_0^u = \begin{bmatrix}\hat{u}^u\\ \hat{v}^u\\ \hat{w}^u\\ \hat{p}^u\end{bmatrix} \qquad \mathbf{x}_0^c = \begin{bmatrix}\hat{u}^c\\ \hat{v}^c\\ \hat{w}^c\\ \hat{p}^c\end{bmatrix} \qquad \mathbf{x}_0^l = \begin{bmatrix}\hat{u}^l\\ \hat{v}^l\\ \hat{w}^l\\ \hat{p}^l\end{bmatrix} \tag{3.27}$$

leading to the matrix partitions

$$\mathbf{E}^u = \begin{bmatrix}\mathbf{E}^u_{uu} & 0 & 0 & 0\\ 0 & \mathbf{E}^u_{vv} & 0 & 0\\ 0 & 0 & \mathbf{E}^u_{ww} & 0\\ \mathbf{E}^u_{pu} & \mathbf{E}^u_{pv} & \mathbf{E}^u_{pw} & 0\end{bmatrix} \qquad \mathbf{A}^u = \begin{bmatrix}\mathbf{A}^u_{uu} & 0 & 0 & 0\\ 0 & \mathbf{A}^u_{vv} & 0 & 0\\ 0 & 0 & \mathbf{A}^u_{ww} & 0\\ 0 & 0 & 0 & \mathbf{A}^u_{pp}\end{bmatrix} \tag{3.28}$$

$$\mathbf{E}^c = \begin{bmatrix} \mathbf{E}^c_{uu} & 0 & 0 & 0 \\ 0 & \mathbf{E}^c_{vv} & 0 & 0 \\ 0 & 0 & \mathbf{E}^c_{ww} & 0 \\ \mathbf{E}^c_{pu} & \mathbf{E}^c_{pv} & \mathbf{E}^c_{pw} & 0 \end{bmatrix} \qquad \mathbf{A}^c = \begin{bmatrix} \mathbf{A}^c_{uu} & \mathbf{A}^c_{uv} & 0 & 0 \\ 0 & \mathbf{A}^c_{vv} & 0 & 0 \\ 0 & 0 & \mathbf{A}^c_{ww} & 0 \\ 0 & \mathbf{A}^c_{pv} & 0 & \mathbf{A}^c_{pp} \end{bmatrix} \tag{3.29}$$

$$\mathbf{E}^l = \begin{bmatrix} \mathbf{E}^l_{uu} & 0 & 0 & 0 \\ 0 & \mathbf{E}^l_{vv} & 0 & 0 \\ 0 & 0 & \mathbf{E}^l_{ww} & 0 \\ \mathbf{E}^l_{pu} & \mathbf{E}^l_{pv} & \mathbf{E}^l_{pw} & 0 \end{bmatrix} \qquad \mathbf{A}^l = \begin{bmatrix} \mathbf{A}^l_{uu} & 0 & 0 & 0 \\ 0 & \mathbf{A}^l_{vv} & 0 & 0 \\ 0 & 0 & \mathbf{A}^l_{ww} & 0 \\ 0 & 0 & 0 & \mathbf{A}^l_{pp} \end{bmatrix} \tag{3.30}$$

$$\mathbf{G}^u = \begin{bmatrix} 0 & 0 \\ \mathbf{G}^u_v & 0 \\ 0 & 0 \\ \mathbf{G}^u_p & 0 \end{bmatrix} \qquad \mathbf{G}^l = \begin{bmatrix} 0 & 0 \\ 0 & \mathbf{G}^l_v \\ 0 & 0 \\ 0 & \mathbf{G}^l_p \end{bmatrix} \tag{3.31}$$

Matrix blocks are defined thanks to the discretization of equations 3.21 and 3.22.

Matrix $\mathbf{A}_{BICs} = \begin{bmatrix} \mathbf{A}^u_{BICs} & \mathbf{A}^c_{BICs} & \mathbf{A}^l_{BICs} \end{bmatrix}$ is defined from the discretization of boundary and interface conditions (equations 3.10).

The lifting functions $\mathbf{G}$ is chosen to satisfy the steady problem with inhomogeneous boundary conditions, but this choice is arbitrary.

It is worth noting that the only coupling among flows in different channel layers is realized through the interface conditions, while different velocity components are coupled in the channel layer only.

The continuum adjoint problem (derived in appendix B) is discretized according to the same procedure.

3.5 Linearized timestepper

The direct and adjoint linear descriptor systems derived in section 3.4.5 need to be integrated in time by means of numerical schemes suitable for descriptor systems. Explicit integration cannot be used because Zero-stability[4] of the method

---

[4] *Zero-stability* is the numerical stability of an integration scheme as long as the time step is limited; thus, it expresses the *conditional stability* of an integration scheme. *A-stability* expresses the *unconditional stability* of an integration scheme. *L-stability* is the ability of an A-stable integration scheme to contract its spectral radius into the origin of the unit circle as $\Re(\lambda h) \to -\infty$ (h and λ being the time step and a system eigenvalue, respectively).

cannot be achieved. A-stability of the integration method is necessary, but also L-stability is needed to filter out oscillations related to the infinite eigenvalues, while retaining the accuracy of the method [76, 4].

In the present work, linear descriptor systems have been integrated in time adopting the two-step backward differentiation formula (BDF-2), which is both A-stable and L-stable, with second order accuracy [95, 4]. Since this scheme is not *self-starting*, the Crank-Nicolson scheme (second order accurate, A-stable, but not L-stable) has been employed for the first time step when initial conditions of the kind $\mathbf{x}_{s_0}$ were prescribed; when initial conditions of the kind $\mathbf{E}_s\mathbf{x}_{s_0}$ were imposed (as in the direct system integration at each step of the ADA algorithm), the backward Euler scheme (first order accurate, both A-stable and L-stable) has been used.

3.6 Control synthesis algorithms

The control methods presented in chapter 2 need some minor adjustments in order to be used for mixed continuum and discrete systems, such as those arising in the lifting function approach (eq. 2.9).

The functional in eq. 2.2 constrained with the system in eq. 2.9 (introducing the adjoint variables $(\boldsymbol{\lambda}, \boldsymbol{\psi})$) reads

$$\begin{multline} \mathcal{J} = \frac{1}{2}\int_0^T \Big(\langle \mathcal{C}\mathbf{x}, \mathcal{C}\mathbf{x} \rangle_{L^2(\Omega)} + \langle \mathbf{u}, \mathbf{R}\mathbf{u} \rangle_2 + \\ - \langle \boldsymbol{\lambda}, \mathcal{E}\frac{\partial \mathbf{x}_0}{\partial t} + \mathcal{E}\mathbf{G}\frac{\mathrm{d}\boldsymbol{\phi}}{\mathrm{d}t} - \mathcal{A}\mathbf{x}_0 - \mathcal{A}\mathbf{G}\boldsymbol{\phi} \rangle_{L^2(\Omega)} - \langle \boldsymbol{\psi},\ m_1\frac{d\boldsymbol{\phi}}{dt} - m_0\boldsymbol{\phi} - \mathbf{u} \rangle_2 \Big)\,\mathrm{d}t \end{multline} \tag{3.32}$$

Defining the adjoint operators $\mathcal{E}^\dagger,\ \mathcal{A}^\dagger$ (see appendix B), it can be expressed as

$$\begin{split} \mathcal{J} = \frac{1}{2}\int_0^T \Big(& \langle \mathbf{x}_0,\ \mathcal{E}^\dagger\frac{\partial \boldsymbol{\lambda}}{\partial t} + \mathcal{A}^\dagger\boldsymbol{\lambda} + \mathcal{C}^\dagger\mathcal{C}\mathbf{x}_0 + \mathcal{C}^\dagger\mathcal{C}\mathbf{G}\boldsymbol{\phi} \rangle_{L^2(\Omega)} + \\ & + \langle \boldsymbol{\phi},\ \int_\Omega \mathbf{G}^H\mathcal{E}^\dagger\frac{\partial \boldsymbol{\lambda}}{\partial t}\,\mathrm{d}\Omega + m_1\frac{d\boldsymbol{\psi}}{dt} + \int_\Omega \mathbf{G}^H\mathcal{A}^\dagger\boldsymbol{\lambda}\,\mathrm{d}\Omega + m_0\boldsymbol{\psi} + \\ & + \mathbf{G}^H\mathcal{C}^\dagger\mathcal{C}\mathbf{x}_0 + \mathbf{G}^H\mathcal{C}^\dagger\mathcal{C}\mathbf{G}\boldsymbol{\phi} - \mathbf{u} \rangle_2 + \\ & + \langle \mathbf{u},\ \mathbf{R}\mathbf{u} + \boldsymbol{\psi} \rangle_2 \big)\,\mathrm{d}t \end{split} \tag{3.33}$$

Direct operators for the full systems have been defined in eq. 2.9. The adjoint operators for the full system are defined as[5]

$$\mathcal{E}_s^\dagger \equiv \begin{pmatrix} \mathcal{E}^\dagger & \mathbf{0} \\ \int_\Omega \mathbf{G}^H \mathcal{E}^\dagger & m_1 \mathbf{I} \end{pmatrix} \quad \mathcal{A}_s^\dagger \equiv \begin{pmatrix} \mathcal{A}^\dagger & \mathbf{0} \\ \int_\Omega \mathbf{G}^H \mathcal{A}^\dagger & m_0 \mathbf{I} \end{pmatrix} \quad \mathcal{B}_s^\dagger \equiv \begin{pmatrix} 0 \\ \mathbf{I} \end{pmatrix} \tag{3.34}$$

The feedback gains could be partitioned as

$$\mathcal{K}_s = \begin{pmatrix} \mathcal{K}_x & \mathcal{K}_\phi \end{pmatrix} \tag{3.35}$$

and the feedback law includes spatial integration on the continuous states only

$$\mathbf{u} = \mathcal{K}_s \begin{pmatrix} \int_\Omega & \mathbf{0} \\ 0 & \mathbf{I} \end{pmatrix} \mathcal{E}_s \mathbf{x}_s \tag{3.36}$$

Using the same discretization procedure explained in section 3.4.5, having defined the matrix $\mathbf{M}_\Omega$ to account for the integration weights in all the channel layers, the adjoint system matrices are

$$\mathbf{E}_s^\dagger \equiv \begin{bmatrix} \mathbf{E}^\dagger & \mathbf{0} \\ \mathbf{G}^H \mathbf{M}_\Omega \mathbf{E}^\dagger & m_1 \mathbf{I} \end{bmatrix} \quad \mathbf{A}_s^\dagger \equiv \begin{bmatrix} \mathbf{A}^\dagger & \mathbf{0} \\ \mathbf{G}^H \mathbf{M}_\Omega \mathbf{A}^\dagger & m_0 \mathbf{I} \end{bmatrix} \quad \mathbf{B}_s^\dagger \equiv \begin{bmatrix} \mathbf{0} \\ \mathbf{I} \end{bmatrix} \tag{3.37}$$

When dealing with a mixed discretized-discrete system, the discrete inner product to be used in eq. 3.36 needs to be defined through the matrix

$$\mathbf{M}_s \equiv \begin{bmatrix} \mathbf{M}_\Omega & \mathbf{0} \\ \mathbf{0} & \mathbf{I} \end{bmatrix} \tag{3.38}$$

to account for both the infinite and finite dimensional parts. Thus, the discretized feedback law can be written as

$$\mathbf{u} = \mathbf{K}_s \mathbf{M}_s \mathbf{E}_s \mathbf{x}_s \tag{3.39}$$

3.6.1 Minimum energy controller

The technique outlined in section 2.4.1 can be used with the system described by matrices $(\mathbf{E}_s,\ \mathbf{A}_s,\ \mathbf{B}_s)$ and its adjoint counterpart $(\mathbf{E}_s^\dagger,\ \mathbf{A}_s^\dagger,\ \mathbf{B}_s^\dagger)$. The numerical computation of the feedback gains is summarized in algorithm 1, which is suitable for both the optimize-then-discretize and the discretize-then-optimize approaches. In order to speed up the eigenanalysis, the Matlab implementation of the ARPACK library [67] has been used to compute only a small subset of the least stable eigenvalues and eigenvectors.

---

[5] For conciseness, integration of differential operators acting on a subset of state variables is denoted by the integration symbol in the corresponding matrix block.

Algorithm 1 Minimum energy controller gains $\mathbf{K}_{MEC}$

```
Require: $\boldsymbol{\sigma}_s \equiv [\sigma_1 \dots \sigma_N]$, $\mathbf{L}_s \equiv [\mathbf{l}_1 \dots \mathbf{l}_N]$, $\mathbf{B}_s,\ \mathbf{B}_s^\dagger$, $\mathbf{M}_s$
$\mathbf{B}_m^{dir} = \mathbf{L}_s^H \mathbf{M}_s \mathbf{B}_s$
$\mathbf{B}_m^{adj} = \mathbf{B}_s^\dagger \mathbf{M}_s \mathbf{L}_s^H$
$\mathbf{C} = \mathbf{B}_m^{dir} \mathbf{B}_m^{adj}$
for $i = 1 \dots N$ do
    for $i = 1 \dots N$ do
        $\mathbf{F}(i,j) = \frac{\mathbf{C}(i,j)}{\sigma_i + \sigma_j^*}$
    end for
end for
$\mathbf{K}_{MEC} = -\mathbf{B}_m^{adj} \mathbf{F}^{-1} \mathbf{L}_s^H$
return $\mathbf{K}_{MEC}$
```

Algorithm 2 ADA gains row $\mathbf{K}_{ADA_i}$

```
Require: $\mathbf{E}_s$, $\mathbf{A}_s$, $\mathbf{B}_s$, $\mathbf{C}_s$, $\mathbf{E}_s^\dagger$, $\mathbf{A}_s^\dagger$, $\mathbf{B}_s^\dagger$, $\mathbf{C}_s^\dagger$, $\mathbf{R}$, $\mathbf{M}_s$
Factorize $(\mathbf{E}_s, \mathbf{A}_s)$ and $(\mathbf{E}_s^\dagger, \mathbf{A}_s^\dagger)$
$\mathbf{E}_s \mathbf{x}_{s_0} = -\left(\mathbf{B}_s^\dagger \mathbf{R}^{-1}\right)_i$
Guess $\mathbf{u}$, $T$
while $e_K > tol_k$ do
    while $err_J > tol_J$ AND $err_{\boldsymbol{\nabla} J} > tol_{\boldsymbol{\nabla} J}$ do
        Integrate: $\mathbf{E}_s \dot{\mathbf{x}}_s = \mathbf{A}_s \mathbf{x}_s + \mathbf{B}_s \mathbf{u}$
        Integrate: $\mathbf{E}_s^\dagger \dot{\boldsymbol{\lambda}}_s = -\mathbf{A}_s^\dagger \boldsymbol{\lambda}_s - \mathbf{C}_s^\dagger \mathbf{C}_s \mathbf{x}_s$
        Evaluate: $J$, $\boldsymbol{\nabla} J$
        Update $\mathbf{u}$ through line minimization
    end while
    Extend T, extrapolate $\mathbf{u}$
end while
$\mathbf{K}_{ADA_i} = \boldsymbol{\lambda}_s(0)^H$
return $\mathbf{K}_{ADA_i}$
```

3.6.2 ADA controller

The technique presented in section 5.3 has been implemented according to algorithm 2. Numerical integration has been performed using the timestepper presented in section 3.5, using the implicit Euler scheme (to allow the imposition of the $\mathcal{E}_s \mathbf{x}_{s_0}$ initial condition) and the Crank-Nicolson schemes for the first step of the direct and adjoint systems respectively. The optimization has been performed for higher values of the time horizon T, until convergence on $\mathcal{K}_{ADA}$ has been reached. To speed up convergence, the initial guess for $\mathbf{u}$ has been chosen as an extrapolation of the value of $\mathbf{u}$ at the previous time horizon. In order to guarantee accurate results, a convergence study varying the time step size Δt has been performed. Line minimization has been performed using the conjugate gradient method [91].

3.7 Implementation in the DNS program

This section shortly describes the steps needed to implement the gain matrix computed from the linearized model into the nonlinear flow solvers. The DNS code for plane channel flow over impermeable walls is described in [73], while its extension to the plane channel bounded by permeable layers is presented in [97]; both of them exploit Fourier decomposition in the wall-parallel directions and a fourth order, compact finite difference scheme in the wall-normal direction.

3.7.1 State computation

The controller state is chosen as the flow perturbation with respect to a base flow. Since the base flow (in this work, the laminar solution) is on the wavenumber pair $(0, 0)$ only, the controller state is computed from all the other spatial modes.

The flow state in DNS has inhomogeneous boundary conditions, while the controller state has homogeneous boundary conditions thanks to the lifting function technique.

The flow state available from DNS can be defined as

$$\mathbf{x}_s^{DNS} \equiv \begin{bmatrix} \mathbf{x} \\ \phi \end{bmatrix} \tag{3.40}$$

and the controller state can be related to it through the relation

$$\mathbf{x}_s \equiv \begin{bmatrix} \mathbf{x}_0 \\ \phi \end{bmatrix} = \begin{bmatrix} \mathbf{I} & -\mathbf{G} \\ \mathbf{0} & \mathbf{I} \end{bmatrix} \mathbf{x}_s^{DNS} \tag{3.41}$$

After discretization, the feedback law (eq. 3.39) can be written for the DNS flow state

$$\mathbf{u} = \mathbf{K}_s \mathbf{M}_s \mathbf{E}_s \begin{bmatrix} \mathbf{I} & -\mathbf{G} \\ \mathbf{0} & \mathbf{I} \end{bmatrix} \mathbf{x}_s^{DNS} \tag{3.42}$$

Considering the block-diagonal form of matrix $\mathbf{E}_s$, the control input reads

$$\mathbf{u} = \mathbf{K}_s \mathbf{M}_s \begin{bmatrix} \mathbf{E} & \mathbf{0} \\ \mathbf{0} & m_1 \mathbf{I} \end{bmatrix} \mathbf{x}_s^{DNS} \tag{3.43}$$

3.7.2 Interpolation

Since the DNS codes implement a compact, fourth order finite difference discretization in the wall-normal direction [73], gain matrices obtained with Chebyshev cardinal functions on a Chebyshev Gauss-Lobatto grid have to be interpolated on the finite difference grid employed in direct numerical simulation.
Hermite cubic splines have been used for interpolation, due to their better behaviour at boundaries with respect to standard cubic splines. Interpolation is performed for gains $\hat{\mathcal{K}}_u(y)$, $\hat{\mathcal{K}}_v(y)$, $\hat{\mathcal{K}}_w(y)$ on each velocity component, for each control input. Real and imaginary part are interpolated separately from the Chebyshev Gauss-Lobatto grid y^{CGL} to the finite difference grid y^{FD}

$$\begin{aligned}
&\Re\{\hat{\mathcal{K}}_u\left(y^{CGL}\right)\} \rightarrow \Re\{\hat{\mathcal{K}}_u\left(y^{FD}\right)\} \qquad &&\Im\{\hat{\mathcal{K}}_u\left(y^{CGL}\right)\} \rightarrow \Im\{\hat{\mathcal{K}}_u\left(y^{FD}\right)\} \\
&\Re\{\hat{\mathcal{K}}_v\left(y^{CGL}\right)\} \rightarrow \Re\{\hat{\mathcal{K}}_v\left(y^{FD}\right)\} \qquad &&\Im\{\hat{\mathcal{K}}_v\left(y^{CGL}\right)\} \rightarrow \Im\{\hat{\mathcal{K}}_v\left(y^{FD}\right)\} \\
&\Re\{\hat{\mathcal{K}}_w\left(y^{CGL}\right)\} \rightarrow \Re\{\hat{\mathcal{K}}_w\left(y^{FD}\right)\} \qquad &&\Im\{\hat{\mathcal{K}}_w\left(y^{CGL}\right)\} \rightarrow \Im\{\hat{\mathcal{K}}_w\left(y^{FD}\right)\}
\end{aligned} \tag{3.44}$$

Since ghost nodes of the finite difference grid are not needed in the numerical integration in wall-normal direction (eq. 3.36), they can be discarded from the gains interpolation procedure. In the same way, matrix $\mathbf{M}_s$ (defined in eq. 3.38) used in the feedback law in the DNS program (eq. 3.43) is assembled with a matrix $\mathbf{M}_\Omega^{FD}$ of integration weights for the finite difference grid.

4

Validation

This chapter provides some validation results for the linearized flow model (section 4.1), its dedicated timestepper (sec 4.2), the minimum energy controller synthesis (sec. 4.3) and the DNS feedback law implementation (sec. 4.4). Numerical results are compared with predictions from linear systems theory. Validation has been performed using both velocity and acceleration as control input; results are shown only for the velocity control input.

4.1 Direct and adjoint eigenanalysis

To validate the numerical formulation employed in this work, eigenanalysis of the direct and adjoint systems has been performed and the computed eigenvalues have been compared with those listed by Schmid and Henningson [101] for the impermeable case and Tilton and Cortelezzi [107] for the porous case. No physically spurious modes have been observed.
Examples of direct and adjoint eigenfunctions are reported in figure 4.1, and should be compared with the inconsistent results obtained from other numerical formulations (figure 3.5).

4.2 Linearized timestepper

To validate the timestepper for the linear descriptor system derived in chapter 3, the uncontrolled direct system has been integrated from an initial condition parallel (in a L^2 sense) to the first unstable eigenfunction, and the kinetic energy growth has been compared with the exponential trend predicted by linear systems

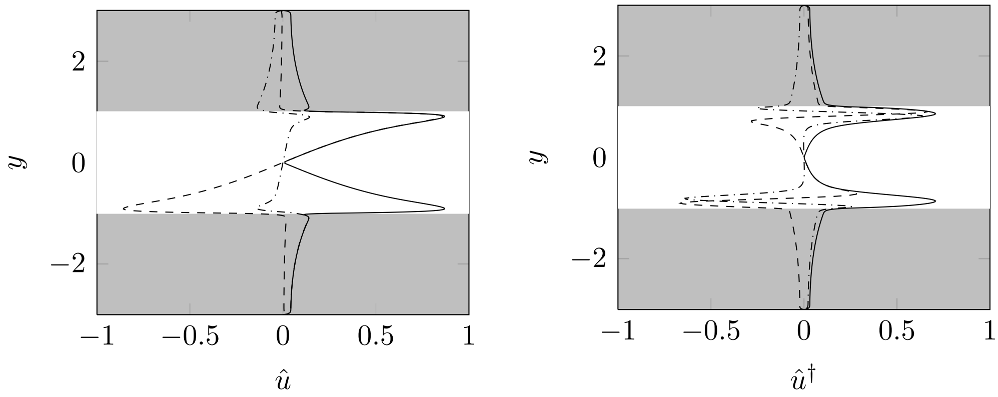

(a) Direct streamwise velocity eigenfunction. (b) Adjoint streamwise velocity eigenfunction.

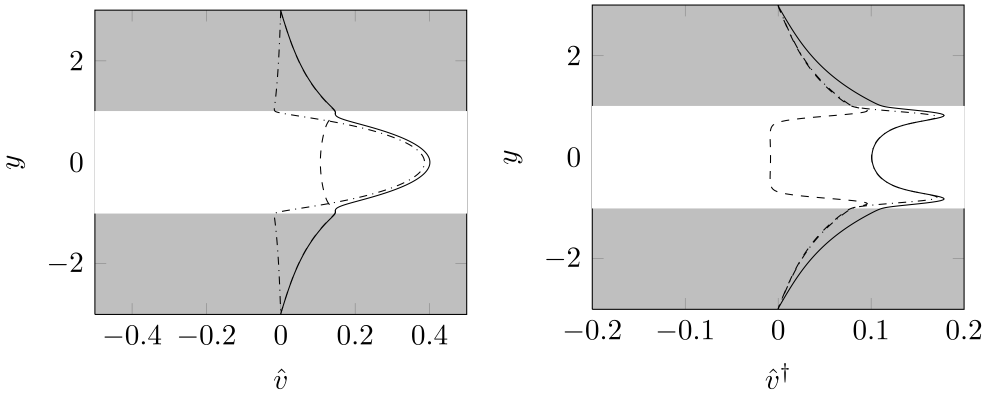

(c) Direct normal velocity eigenfunction. (d) Adjoint normal velocity eigenfunction.

Figure 4.1: Direct and (continuous) adjoint eigenfunctions of the first unstable mode for the plane channel with permeable wall, computed by descriptor Kleiser-Schumann technique. Porous layer are symmetric, the case is $Re_b = 2000$, $(\kappa_x, \kappa_z) = (1, 0)$, $\sigma = 0.02$, $\epsilon = 0.6$, $\tau = 0$, $h = 1$ (as in figure 5 of [107]), with $N = 100$ in all layers. Dashed line is real part, dash-dotted line is imaginary part, solid line is absolute value. Spanwise velocity component is zero (not shown).

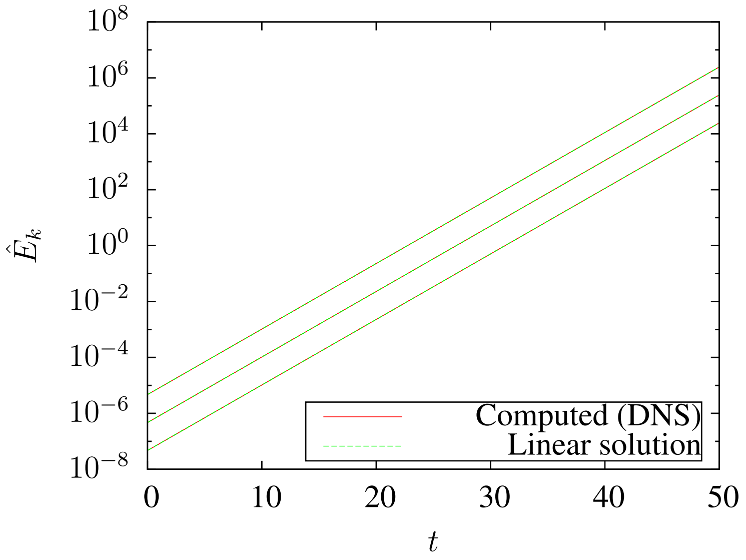

Figure 4.2: Linear descriptor system timestepper validation. Flow case is $Re_P = 6000$, $N = 64$, $\kappa_x = 1$, $\kappa_z = 0$, $\sigma = 0.02$, $\epsilon = 0.6$, $\tau = 0$, $h = 1$. Results are compared with the analytical prediction of linear systems theory; curves are overlapping.

theory[1]. An example for a permeable case is shown in figure 4.2, for different amplitudes of the initial condition.

4.3 Minimum energy controller

The minimum energy controller moves the unstable system eigenvalues to their symmetric location with respect to the imaginary axis; this property can be exploited to validate the numerical implementation of the minimum energy controller. The moved eigenvalues have been numerically compared with the uncontrolled ones; a graphical example is shown in figure 4.3.

4.4 DNS feedback module

To validate the implementation of the feedback law into the DNS solvers, the control has been applied to the time evolution of a perturbed laminar field. The

---

[1] Denoting as λ the eigenvalue corresponding to the eigenfunction chosen as initial condition, the linearized system kinetic energy evolution is $\hat{E}(t) = \hat{E}_0 e^{2\Re(\lambda)t}$.

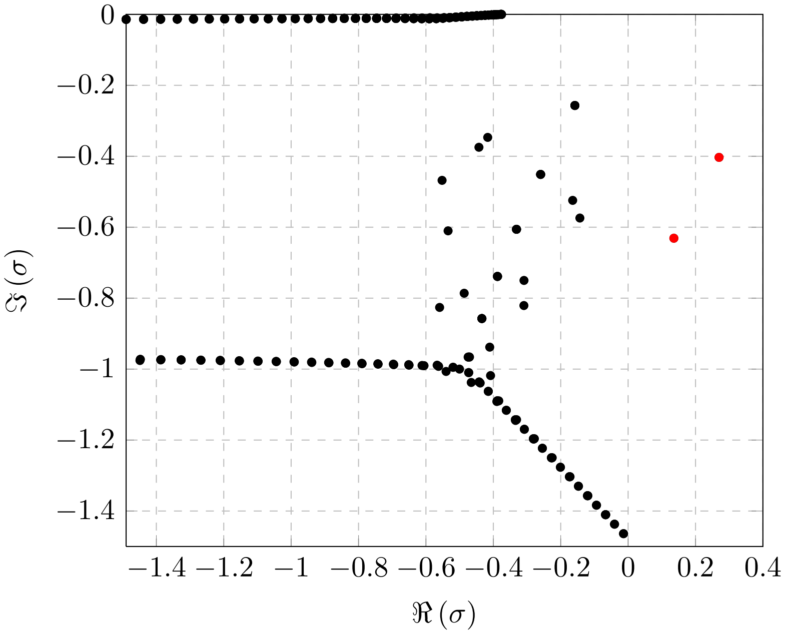

(a) Uncontrolled direct system spectrum.

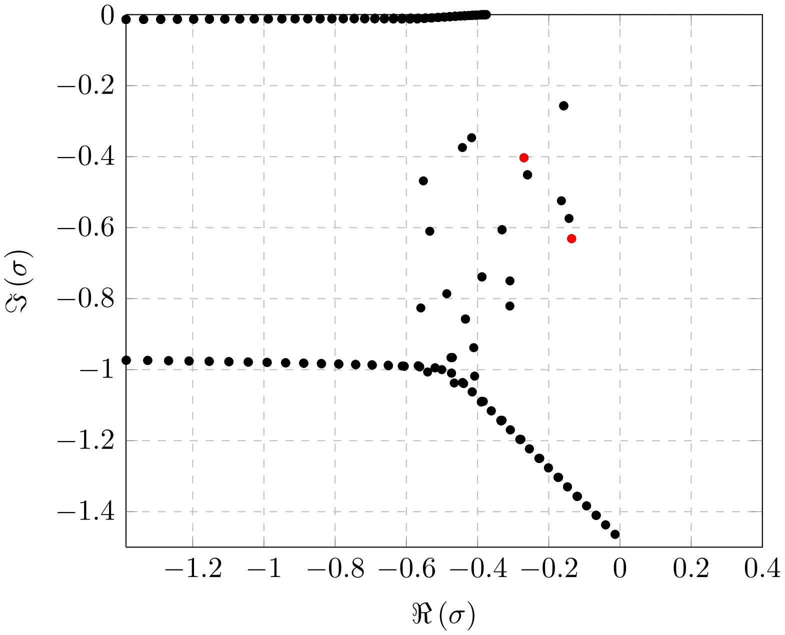

(b) Controlled direct system spectrum.

Figure 4.3: Uncontrolled and controlled direct system spectra for $Re_b = 4000$, $\kappa_x = 1$, $\kappa_z = 0$, $\sigma = 0.02$, $\epsilon = 0.6$, $\tau = 0$, $h = 1$; porous layers are symmetric. Only the least stable finite eigenvalues are shown. Unstable and reflected eigenvalues are marked in red.

perturbation is parallel (in a L^2 sense) to the least stable eigenfunction of the wavenumber pair $(1, 0)$, with an amplitude sufficiently small to assume linearity, in order to verify the exponential decay of the perturbation kinetic energy.
Some results are shown in figure 4.4 for different scalings of the initial condition, for both the impermeable and permeable cases. As long as the initial perturbation amplitude is sufficiently small, results are in agreement with predictions of linear systems theory; for higher values of perturbation amplitude, other spatial modes begin to be excited.

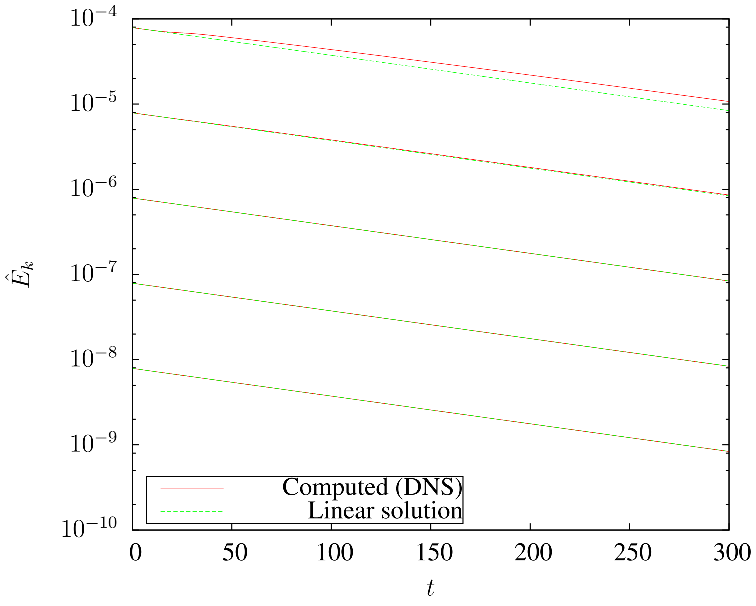

(a) Impermeable walls.

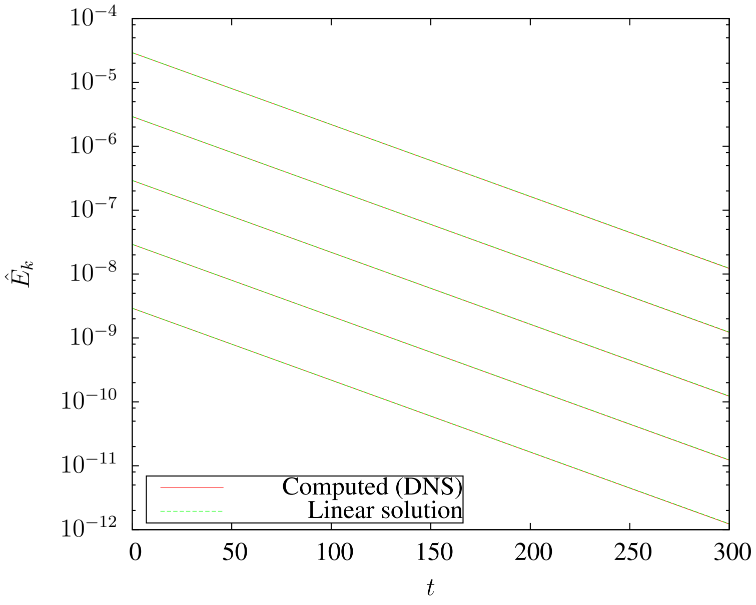

(b) Permeable walls.

Figure 4.4: DNS feedback controller validation. Top: Impermeable walls, $Re_P = 10000$. Bottom: Permeable walls, $Re_P = 3000$, $\sigma = 0.02$, $\epsilon = 0.6$, $\tau = 0$, $h = 0.5$ (symmetric porous layers). Results are compared with the analytical prediction; curves are overlapping, as long as the initial perturbation amplitude is sufficiently small to consider linearity valid.

5

Results

In the previous chapters, techniques for an offline computation of the feedback gains (which are more appropriate for the application in an experimental setup) have been presented. Several issues have prevented the application of standard Riccati-based techniques to the computation of LQRs in wavenumber space, and more expensive alternatives (based on the continuous adjoint method) have been found to be able to overcome the numerical difficulties.

Due to its computational efficiency, the minimum energy controller offers an optimal benchmark for *continuous adjoint* techniques. Control gains synthesis in all the wavenumber space is cheap, allowing for a first look to a convolution kernel in physical space for plane channel flow over porous layers. The minimum energy controller applicability, however, is limited to linearly unstable systems, i.e. to supercritical values of Reynolds number only. Since this controller represents the ”expensive control” limit, in which its authority is reduced to a minimum in order to keep the control energy expenditure as low as possible, it is unlikely for this controller to be effective in reducing turbulence. This controller constitutes a necessary validation step before the implementation of techniques able to handle more general flow cases (with higher values of controller authority and lower values of Reynolds number); from an engineering viewpoint, simple models and techniques are always to be considered before further efforts in more involved techniques. The adjoint of the direct-adjoint controller offers a first example of more general techniques, allowing further studies on control of linear paths to transition.

Before proceeding with the controller design, stabilizability of the coupled system is checked (section 5.1). Section 5.2 presents the results for the minimum energy controller gains in both wavenumber and physical space, with an application on the nonlinear flow simulation. Section 5.3 presents the feedback gains for the ADA controller in wavenumber space. The descriptor systems framework in conjunction with the continuous adjoint method makes it impossible to compare performances in terms of $\mathcal{H}_2$ and $\mathcal{H}_\infty$ transfer function norms, since their direct evaluation from the solution of Lyapunov equations is limited to discrete adjoint state-space systems. Thus, the following analysis aims to obtain as much information as possible from the first feedback gains which it has been possible to compute with the techniques analyzed in this work.

Feedback gains analysis alone is sufficient to highlight some weaknesses of standard LQRs for plane channel flow: In view of an implementation in a physical experiment, controllers designed with an impermeable model could not be robust enough to model uncertainties, and the modeling of actuators geometry in flow control system design could be essential for experimental applications (section 5.4). The permeability model could provide a flexible tool whose parameters could be adjusted to match the specific application after an experimental characterization of the streamwise and spanwise mean effects of the synthetic jets actuation system.

5.1 Modal controllability analysis

A necessary prerequisite for control system design is the system controllability analysis. Since the system can be linearly unstable, it is not controllable and stabilizability must be checked through modal analysis [106].

Controllability residual c_j is defined as the euclidean norm of the projection of the input operator on the $j-\mathrm{th}$ eigenmode

$$c_j = \|\langle \mathbf{l}_j,\, \mathcal{B}\rangle_{L^2(\Omega)}\|_2 \tag{5.1}$$

The projection is done through the inner product by the adjoint eigenfunction, as in section 2.4.1.

Table 5.1 lists the results for the unstable eigenmodes of the wavenumber pair $(1, 0)$ for different values of Reynolds number and permeability. Higher values of Reynolds number and permeability worsen the modal controllability, but the system is still stabilizable since the controllability residuals for the unstable eigenmodes do not vanish. This is sufficient to proceed with the controller synthesis.

5.2 Minimum energy controller

This section shows how permeability modifies the minimum energy controller gains for plane channel flow, both in wavenumber space (section 5.2.1) and in physical space (section 5.2.3).

σ Re_b	0	2×10^{-4}	2×10^{-3}	2×10^{-2}
4000	1.24607	2.58255×10^{-1}	2.97759×10^{-1}	2.66180×10^{-1} 2.17505×10^{-1}
5000	1.09083	2.77318×10^{-1}	3.18477×10^{-1}	2.61395×10^{-1} 2.10715×10^{-1}
6000	1.17748	3.13600×10^{-1}	2.62168×10^{-1}	2.36203×10^{-1} 2.05410×10^{-1}

Table 5.1: Modal controllability residuals of unstable modes for different values of porosity and bulk Reynolds number, for wavenumber pair $(1, 0)$.

Correctness of the controller synthesis and its implementation in both the linearized and nonlinear simulations have been checked in sections 4.3, 4.2 and 4.4. Here, performance with impermeable and permeable walls are compared in linearized (section 5.2.2) and nonlinear (section 5.2.4) simulations.

5.2.1 Gains in wavenumber space

The linearly destabilizing effect of permeability [107] strongly affects the results of the linear controller synthesis, since linear controllers depend on the modal properties of the system. A marked amplification of the gains in wavenumber space is observed as permeability is increased (figures 5.1, 5.2, 5.3, 5.3, 5.4). As long as the unstable eigenvalue is only one, gains are symmetric/antisymmetric with respect to the channel centerline; a direct comparison for different values of permeability is shown in figure 5.5. When permeability is high enough to destabilize two Orr-Sommerfeld modes (figure 5.4), gains lose the symmetry property[1] and begin to exhibit some kind of localization in the wall-normal direction. Gains are higher in proximity of the actuator (in figure 5.4, actuation is on the upper wall). Gains for actuators placed on the upper and lower wall are symmetric with respect to the channel centerline.

As for gains with impermeable walls, gains with permeable layers vanish at walls; but the walls, now, are under the porous regions. At the interfaces between channel and porous layers gains do not vanish; they are continuous across the inter-

---

[1] Eigenfunctions are symmetric/antisymmetric with respect to the channel centerline, and the minimum energy controller gains depend on a linear combination of the unstable adjoint eigenfunctions.

faces (as velocity) and the importance of the porous regions increases with permeability. Velocity in the porous regions also increases with permeability, thus the amount of state information needed by the controller about the porous regions follows the same trend.

All the techniques considered in this work allow the computation of feedback gains on the pressure states also. On a physical ground, one could expect that algebraic states do not contribute to the feedback law; this is a correct conjecture, but a clear distinction among differential and algebraic states is not always as easy as in the present case. In the discrete adjoint setting, the system should be reduced to a canonical form to clearly see the distinction between these two families of states, and optimal feedback gains would be computed only on the differential states in the new coordinate system; transforming the results back to the original coordinate system, feedback gains would appear to couple differential and algebraic states in a non-trivial way [32]. In the present work, gains appear to act on both velocity and pressure, but the distinction among differential and algebraic states is clear from the structure of the operator $\mathcal{E}_s$; the contribution of feedback gains on pressure to the feedback law is filtered out through the multiplication by operator $\mathcal{E}_s$ (eq. 3.36).

Gains show strong gradients and peak values in the near-interface regions of the channel layer, due to the coupling between pressure and velocity and between streamwise and wall-normal velocity; in the porous regions, where there is no coupling among velocity components nor pressure, gains vary monotonically between interfaces and walls. Gains on normal velocity have high values at the channel centerline also, while gains on streamwise velocity approach zero at the channel centerline.

Here, gains are shown for the different cartesian velocity components. To allow comparisons with standard works on plane channel flow control, gains on wall-normal vorticity can be computed from the algebraic relation

$$\hat{\mathcal{K}}_\eta = \frac{\hat{\mathcal{K}}_u}{i\kappa_z} = -\frac{\hat{\mathcal{K}}_w}{i\kappa_x} \tag{5.2}$$

Similar trends have been found by varying the porous layers height at a fixed value of permeability. Gains increase by increasing the permeable layers height (and so the transpiration between channel and porous regions), always being higher than the impermeable case, with a strong dependence of the symmetry properties on the number of unstable eigenmodes.

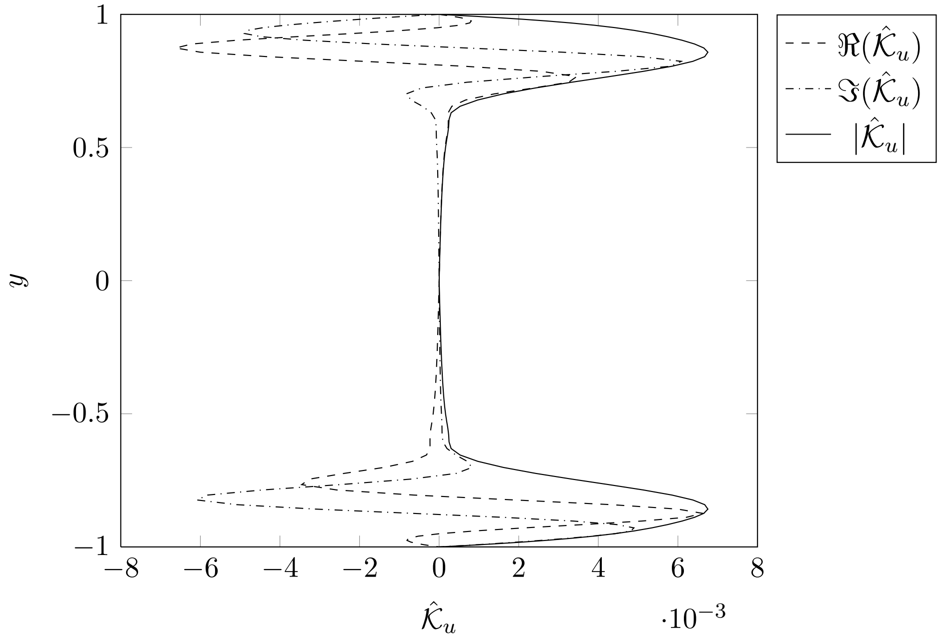

(a) Streamwise velocity gains (impermeable walls).

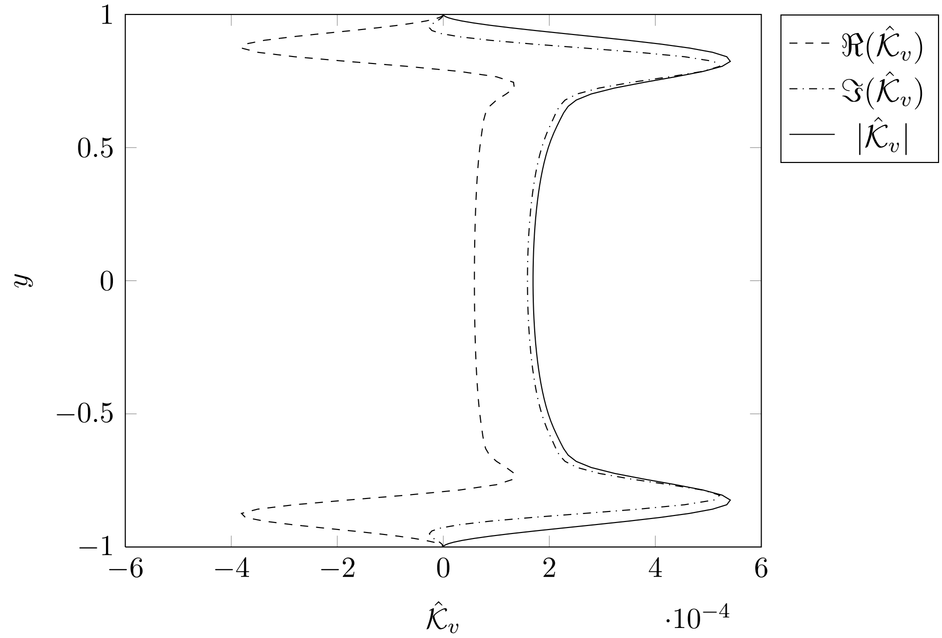

(b) Normal velocity gains (impermeable walls).

Figure 5.1: Minimum energy controller gains for control input on the upper wall. Top: Streamwise velocity gains. Bottom: Wall-normal velocity gains. Flow case is $Re_P = 6000$, $(\kappa_x, \kappa_z) = (1, 0)$ (as table 1 of [107]), with $N = 100$. Gains for spanwise velocity are zero (not shown).

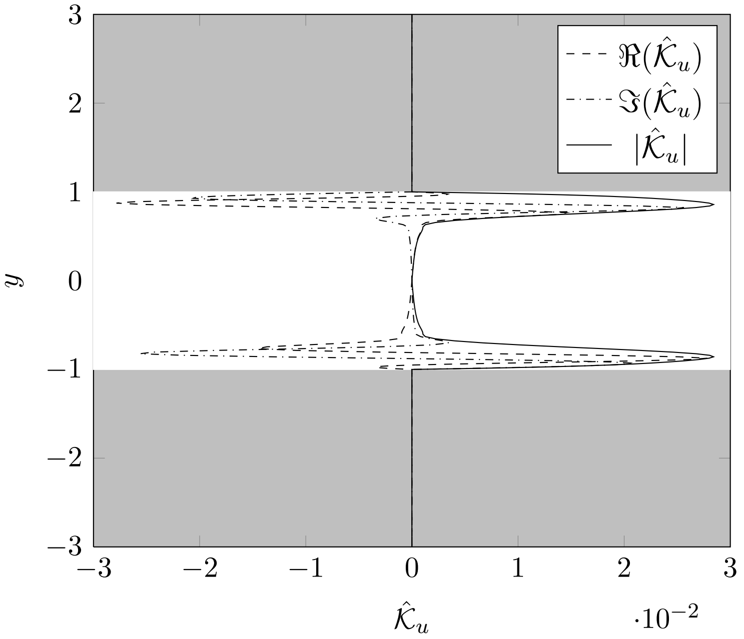

(a) Streamwise velocity gains ($\sigma = 0.0002$).

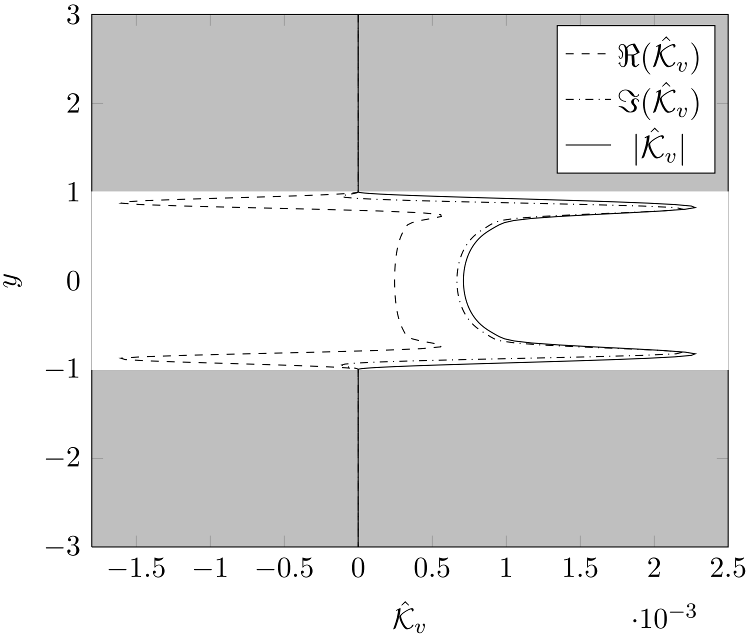

(b) Normal velocity gains ($\sigma = 0.0002$).

Figure 5.2: Minimum energy controller gains for control input on the upper wall. Top: Streamwise velocity gains. Bottom: Wall-normal velocity gains. Flow case is $Re_P = 6000$, $(\kappa_x, \kappa_z) = (1, 0)$. Porous layer are symmetric, $\sigma = 0.0002$, $\epsilon = 0.6$, $\tau = 0$, $h = 1$ (as table 1 of [107]), with $N = 100$ in all layers. Gains for spanwise velocity are zero (not shown).

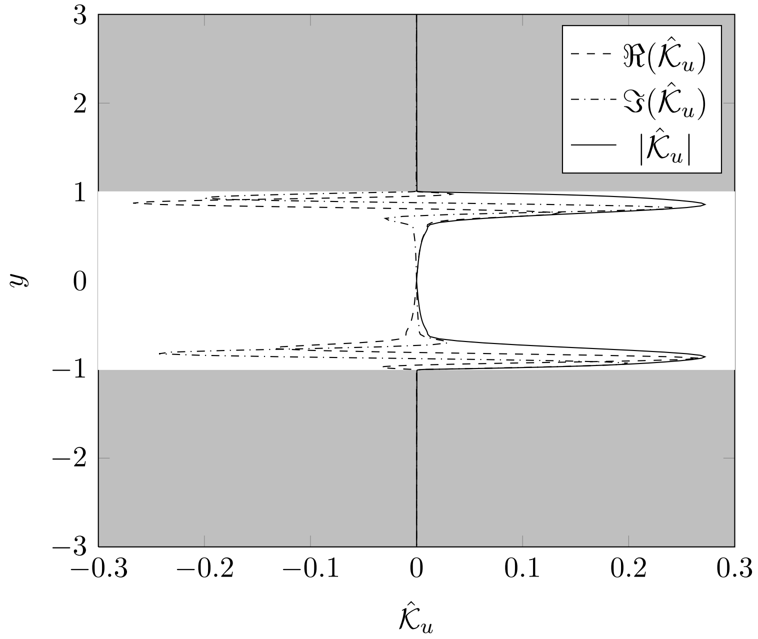

(a) Streamwise velocity gains ($\sigma = 0.002$).

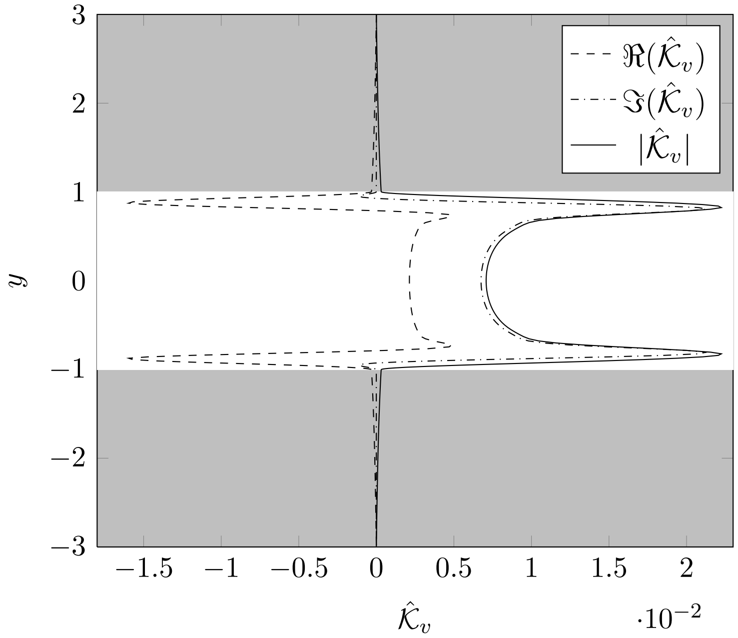

(b) Normal velocity gains ($\sigma = 0.002$).

Figure 5.3: Minimum energy controller gains for control input on the upper wall. Top: Streamwise velocity gains. Bottom: Wall-normal velocity gains. Flow case is $Re_P = 6000$, $(\kappa_x, \kappa_z) = (1, 0)$. Porous layer are symmetric, $\sigma = 0.002$, $\epsilon = 0.6$, $\tau = 0$, $h = 1$ (as table 1 of [107]), with $N = 100$ in all layers. Gains for spanwise velocity are zero (not shown).

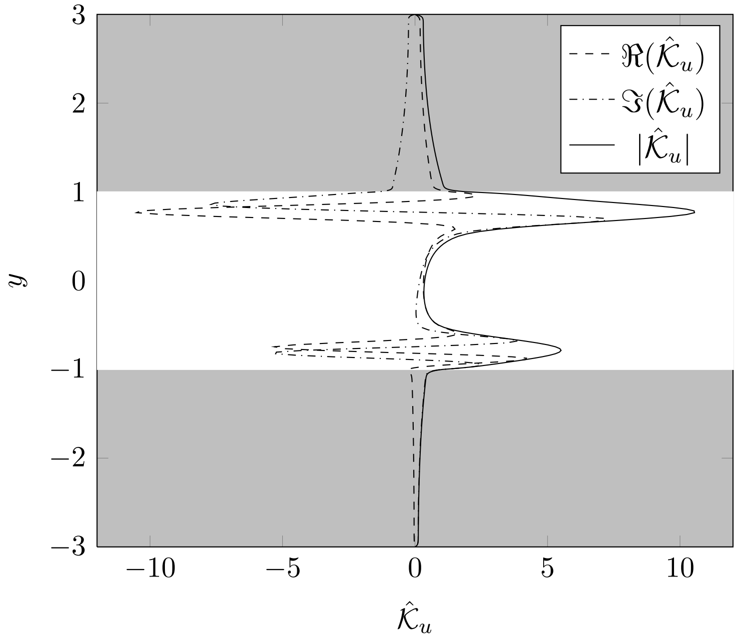

(a) Streamwise velocity gains ($\sigma = 0.02$).

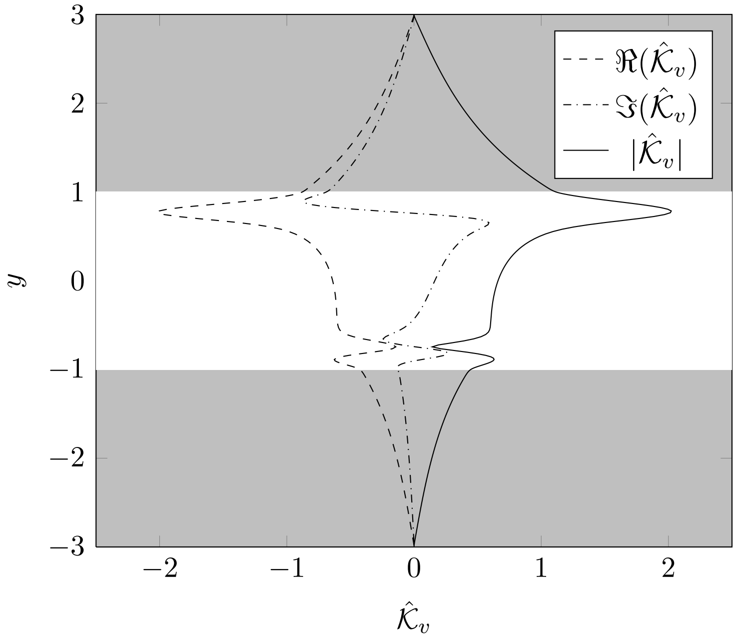

(b) Normal velocity gains ($\sigma = 0.02$).

Figure 5.4: Minimum energy controller gains for control input on the upper wall. Top: Streamwise velocity gains. Bottom: Wall-normal velocity gains. Flow case is $Re_P = 6000$, $(\kappa_x, \kappa_z) = (1, 0)$. Porous layer are symmetric, $\sigma = 0.02,\ \epsilon = 0.6,\ \tau = 0,\ h = 1$ (as table 1 of [107]), with $N = 100$ in all layers. Gains for spanwise velocity are zero (not shown).

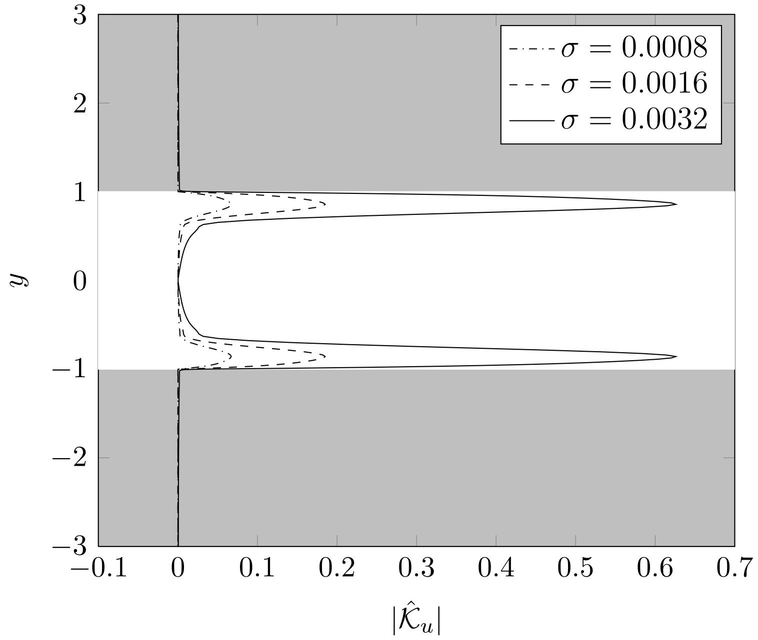

(a) Streamwise velocity gains.

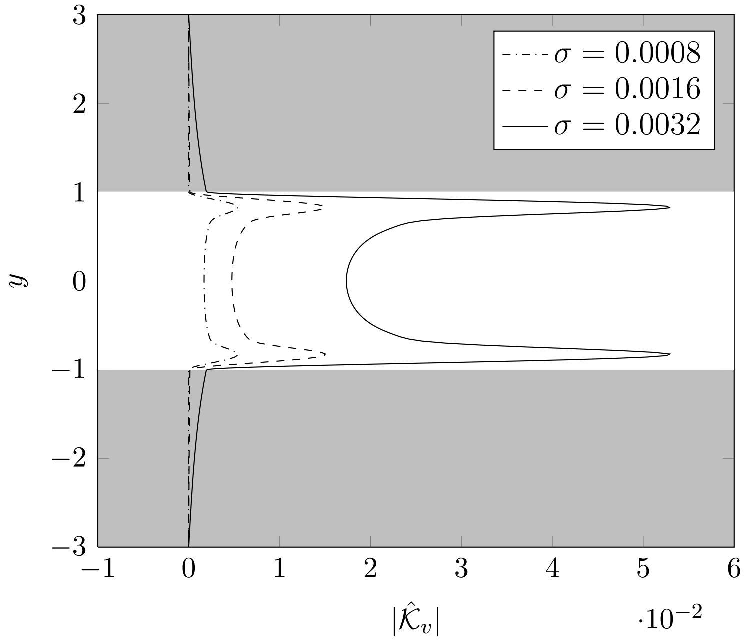

(b) Normal velocity gains.

Figure 5.5: Minimum energy controller gains for control input on the upper wall. Top: Streamwise velocity gains. Bottom: Wall-normal velocity gains. Comparison with different permeability. Porous layers are symmetric, flow case is $Re_P = 6000, \ \epsilon = 0.6, \ \tau = 0, \ h = 1$. Gains for spanwise velocity are zero (not shown).

5.2.2 Performance on the linearized system

The kinetic energy evolution of a perturbed laminar base flow for the uncontrolled and controlled system is shown in figure 5.6, for both an impermeable and a permeable case at the same constant flow rate[2]. The initial condition is parallel to the eigenfunction corresponding the highest real part eigenvalue of the uncontrolled linearized system, thus its energy exhibits a perfectly exponential growth. In the controlled setting, the same perturbation has components on more than one eigenfunctions of the controlled system, and its energy decay is the superimposition of the decay rate of these eigenmodes (not purely exponential anymore).
Since the permeable case is much more unstable than the impermeable one, the energy growth rate of the two uncontrolled systems is very different. For the controlled system, the asymptotic growth rate is dictated by the real part of the least stable eigenvalue. In the impermeable case, it corresponds to the reflection of the Tollmien-Schlichting eigenvalue (which, in the analyzed case, has very small real part); in the permeable case, the unstable eigenvalue has higher real part and the asymptotic growth rate of the controlled system is determined by the least stable eigenvalue in the P-branch (center modes [101]) of the spectrum.

5.2.3 Convolution kernel

An example of convolution kernel in physical space for the minimum energy controller is presented in figure 5.7, representing the isosurfaces of the 5% of the maximum (red) and minimum (blue) values for each velocity component. Porous layers are symmetric; flow case is $Re_P = 3000,\ \sigma = 0.02,\ \epsilon = 0.6, \tau = 0,\ h_p = 0.5,\ L_x = 4\pi,\ L_z = 4\pi$. $N = 80$ in each channel layer. Interfaces can be readily identified by the thickening of structures, which extend till the channel side boundaries.
Controller localization in the invariant directions (see section 2.2) is lost, since this property is related to the controller degree of authority. As suggested in [5], there could be an inherent tradeoff between a cheap controller and a localized one: Cheap (low authority) controllers need information from all the domain to achieve optimality, while higher degrees of authority allow controllers to be more centralized, taking information from sensors in their neighborhood only.
A small amount of localization in the wall-normal direction, however, can be

---

[2] As in chapter 4, the kinetic energy evolution for an initial condition parallel to the direct eigenfunction relative to an eigenvalue λ is $\hat{E}(t) = \hat{E}_0 e^{2\Re(\lambda)t}$.

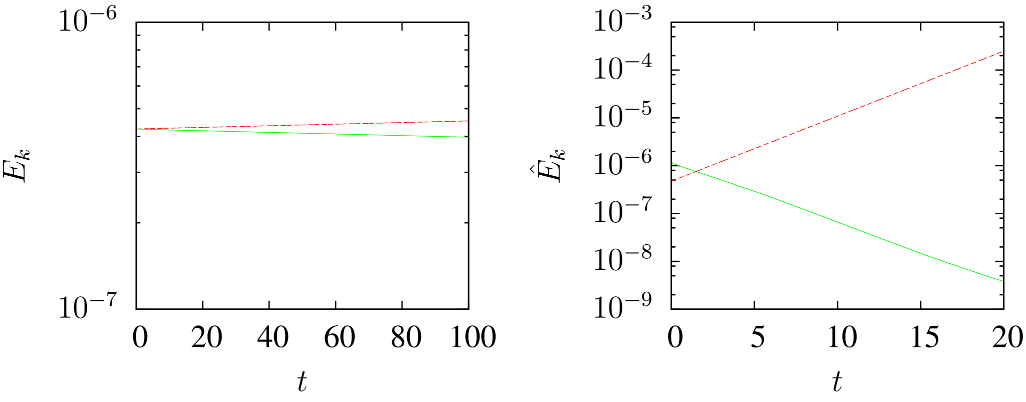

(a) Impermeable walls.

(b) Permeable walls, $\sigma = 0.02$.

Figure 5.6: Comparison between uncontrolled and controlled flow in the linearized simulation, with impermeable (left) and permeable (right) walls. Red: Uncontrolled case. Green: Controlled case. Flow case is $Re_P = 6000, \kappa_x = 1, \ \kappa_z = 0$; porous walls are symmetric, with $\sigma = 0.02, \ \epsilon = 0.6, \ \tau = 0, \ h = 0.5$. The initial condition is parallel to the eigenfunction corresponding the highest real part eigenvalue of the uncontrolled linearized system.

seen near the interfaces between channel and porous layers, where the isosurfaces of the normal velocity kernel show small bulges; these are more pronounced in proximity of the actuator (in this case, on the lower wall). The kernel structures support, in the permeable case, extends through the interfaces and into the porous layers. As noted for gains on normal velocity in wavenumber space, minima and maxima of the convolution kernel extends through all the channel layer.

Isosurfaces for streamwise and spanwise velocity components (thus, for wall-normal vorticity) are strongly localized near the interface between channel and porous regions, showing a checkerboard pattern which reminds the structures seen in centralized LQRs for plane channel flow with impermeable walls (here, without localization in the invariant directions).

5.2.4 Performance in DNS

The kinetic energy evolution of a perturbed laminar base flow has been studied in DNS also (figure 5.8). Computations have been made using the DNS solvers with impermeable walls [73] and permeable layers [97] with the feedback module described in section 3.7.

The same perturbation given in section 5.2.2 has been imposed as initial condition

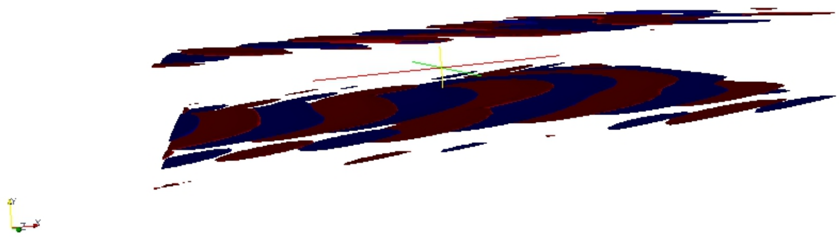

(a) Isosurfaces of convolution kernel $\mathcal{K}_u$ for streawise velocity.

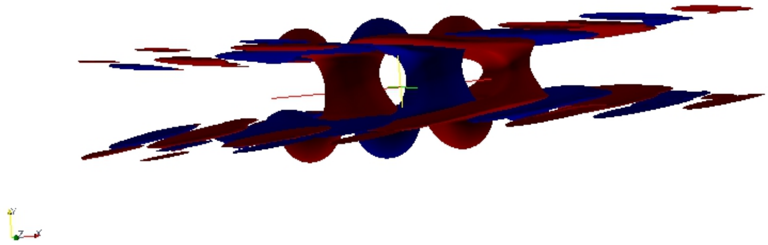

(b) Isosurfaces of convolution kernel $\mathcal{K}_v$ for wall-normal velocity.

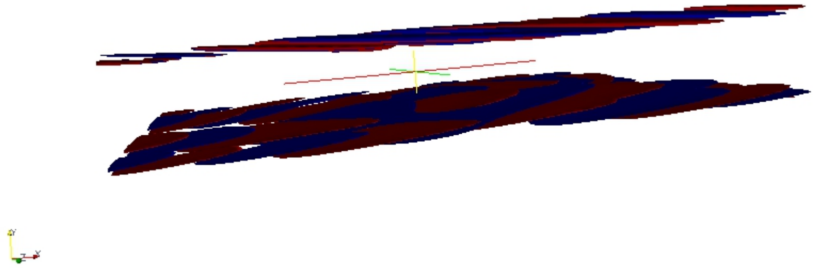

(c) Isosurfaces of convolution kernel $\mathcal{K}_w$ for spanwise velocity.

Figure 5.7: Isosurfaces of the 5% of the maximum (red) and minimum (blue) value of the convolution kernel on each velocity component, for the control input on the lower wall. Porous layers are symmetric; flow case is $Re_P = 3000,\ \sigma = 0.02,\ \epsilon = 0.6, \tau = 0,\ h_p = 0.5,\ L_x = 4\pi,\ L_z = 4\pi.\ N = 80$ in each channel layer.

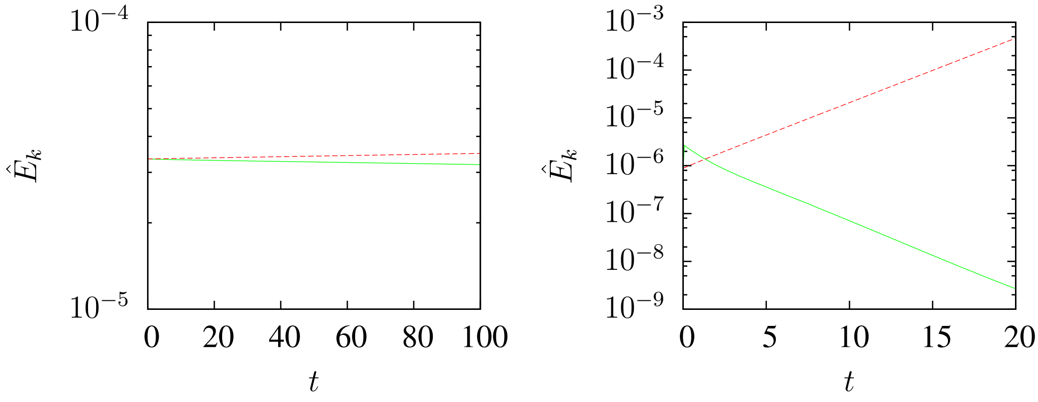

(a) Impermeable walls. (b) Permeable walls, $\sigma = 0.02$.

Figure 5.8: Comparison between uncontrolled and controlled flow in DNS, with impermeable (left) and permeable (right) walls. Red: Uncontrolled case. Green: Controlled case. Flow case and initial condition are the same as in fig. 5.6.

on the spatial mode $(1, 0)$, with an amplitude small enough to satisfy the linearity assumption. As in the linearized simulation, in the controlled setting the perturbation is split on different controlled system eigenfunctions (thus, the energy decay is exponential in time only asymptotically) but no other spatial mode is excited.

The application on a fully developed turbulent flow has been tried also. Figure 5.9 shows the comparison between the effects of the minimum energy controller on the channel with impermeable walls and with permeable layers. In the impermeable case, the time evolution of the streamwise component of the non-dimensional wall shear stress τ_w is shown, for both the uncontrolled and controlled cases; in the permeable case, the value of the shear stress at the interfaces between channel and porous layers is shown. With impermeable walls, the wall shear stress is due entirely to the viscous contribution (thanks to the no-slip condition); with permeable layers, transpiration makes the Reynolds stresses give a contribution to the shear stress at the interfaces.
As expected, the controller authority is too low to produce significant effects on the turbulent flow; the wall shear stress in the controlled case is almost unchanged. The computed control input (wall-normal velocity at walls) is of the order of $\mathcal{O}\left(10^{-6}\right)$: It is maybe enough to control a perturbed laminar base flow, but not to reduce the intensity of turbulent fluctuations and their contribution to wall shear stress.

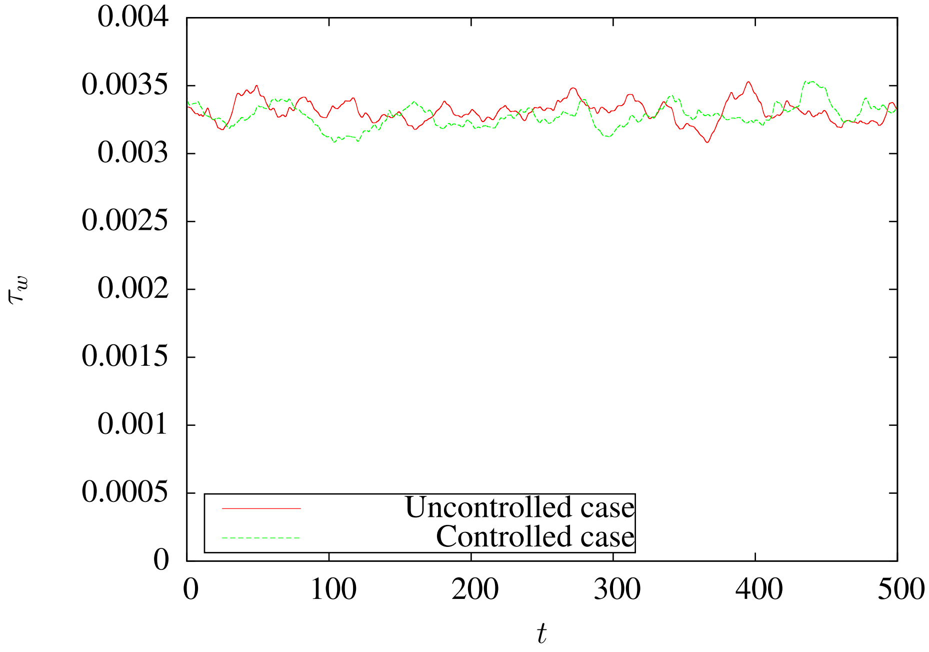

(a) Impermeable walls.

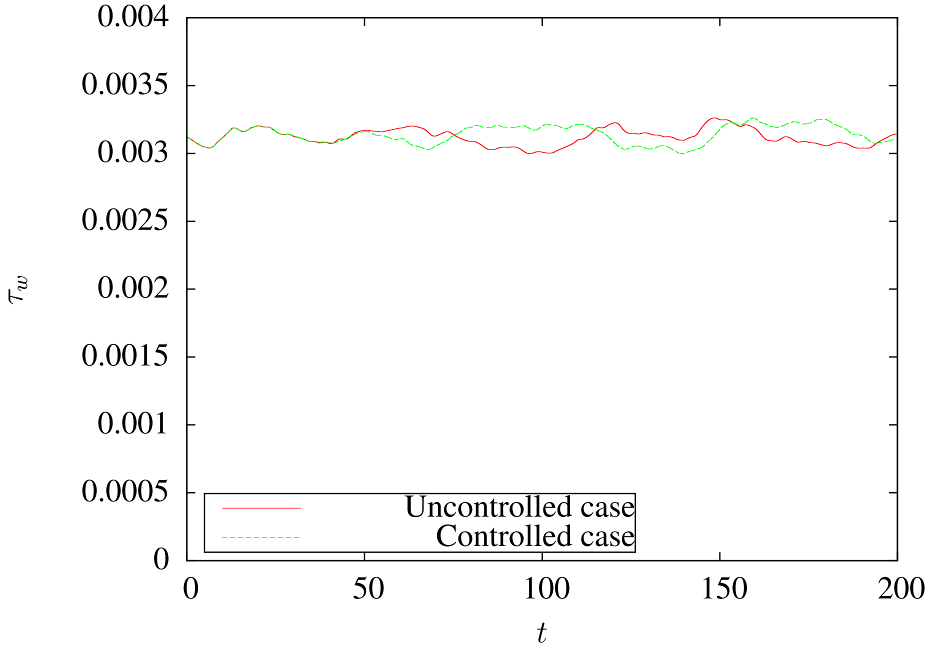

(b) Permeable walls.

Figure 5.9: Comparison between uncontrolled and controlled flow in DNS, with impermeable (top) and permeable (bottom) walls. Flow case is $Re_P = 6000$, starting from a fully developed turbulent flow. Porous layers are symmetric, $\sigma = 0.001$, $\epsilon = 0.6$, $\tau = 0$, $h = 0.5$.

5.3 Adjoint of the Direct-Adjoint controller

Some feedback gains for subcritical plane channel flow and higher controller authority, computed through the adjoint of the direct-adjoint technique (section 5.3), are presented in this section.

The state norm necessary to the objective functional (eq. 2.2) in wavenumber space is defined as the kinetic energy in all the channel layers

$$\|\mathcal{C}\mathbf{x}\|^2_{L^2(\hat{\Omega})} \equiv \frac{1}{2}\int_{-1}^{1} \hat{\mathbf{u}}^* \cdot \hat{\mathbf{u}}\,\mathrm{d}y + \frac{1}{2}\int_{1}^{1+2h_1/h} \langle\hat{\mathbf{u}}\rangle_1^* \cdot \langle\hat{\mathbf{u}}\rangle_1\,\mathrm{d}y + \frac{1}{2}\int_{-1-2h_2/h}^{-1} \langle\hat{\mathbf{u}}\rangle_2^* \cdot \langle\hat{\mathbf{u}}\rangle_2\,\mathrm{d}y \tag{5.3}$$

Relation $\mathbf{x} = \mathbf{x}_0 + \mathbf{G}\boldsymbol{\phi}$ is used to express the kinetic energy as a function of the state $\mathbf{x}_s$, allowing to define the operator $\mathcal{C}_s^\dagger\mathcal{C}_s$.

The control weight is defined as

$$\mathbf{R} = \rho\mathbf{I} \tag{5.4}$$

As noted in [103], the rate of convergence of the iterative optimization depends on the value of the control weight. Higher values lead to faster convergence, since the quadratic functional $\mathcal{J}(\mathbf{u})$ becomes steeper. Convergence is slowed down by increasing the Reynolds number also.

Some care is needed when handling supercritical (linearly unstable) cases. Since the state of the dynamical system tends to diverge, the first time integration should be performed on a sufficiently small time horizon or, equivalently, a stabilizing initial guess of $\mathbf{u}$ should be introduced. The minimum energy controller could be useful to provide such stabilizing guess.

In this work, the Reynolds number $Re_P = 600$ and the control weight $\rho = 1000$ have been used. These parameters have proven to provide convergence on maximum time horizon $T = 225$ (bulk time scale). The maximum number of iteration has been less than 100 with the first time horizon used, reducing to less than 10 with the last time horizon employed. A tolerance of 10^{-6} has been imposed on the relative functional variation.

Spectra of the controlled system and performance of the controller in reducing an arbitrary perturbation are not reported here, since the convergence of the iterative optimization is itself a proof of the stabilizing effect of the controller and root locus analyses have proven not to be meaningful for the characterization of flow controllers properties [14]. Performance of these controllers should be further assessed by studying the reduction of transient energy growth in subcritical channel flow.

The full decoupling of the control problem in wavenumber space allows to perform computations in parallel, with no communication among processes. Before computing a whole convolution kernel, however, the iterative optimization procedure should be made robust enough to be performed automatically for all wavenumber pairs. Since convergence could take longer on certain wavenumber pairs rather than others, load balancing issues should be considered. These topics have not been further developed in this work.

5.3.1 Gains in wavenumber space

Figures 5.10, 5.11, 5.12, 5.13 show ADA controller gains on velocity for different values of permeability; figures 5.14, 5.15, 5.16, 5.17 show gains variation with increasing porous layers height.

As in the expensive control limit, gains grow with an increase in permeability, while decrease with increasing porous layers height.

Since feedback gains now depend an all the adjoint eigenfunctions (not only the unstable ones, as in the minimum energy controller), there is no symmetry with respect to the channel centerline. Gains shape, however, strongly resembles the one of minimum energy controller gains, with monotonical growth in the porous regions, strong gradients at the interfaces and peaks localized close to the interfaces.

Direct comparisons of feedback gains absolute value for different values of permeability and porous layers height are shown in figures 5.18 and 5.19. It can be seen how amplitude varies, but shape is almost unchanged. Differently from what happens in the expensive control limit, the impermeable case do not provide minimum gains, and gains now *decrease* with increasing porous layer height. These features could be explained with the influence of the chosen state norm, which consider the kinetic energy of both channel and porous regions, and modifies the results in a non-trivial way. Further studies should target the effects of other norms (as the dissipation norm [77, 25]).

5.4 Robustness to model uncertainties - A preliminary assessment

The dramatic amplification of feedback gains when permeability is increased allows some considerations on robustness of LQRs for plane channel flow. Classical robustness results for MIMO LQRs are gain margins between 0.5 and $+\infty$

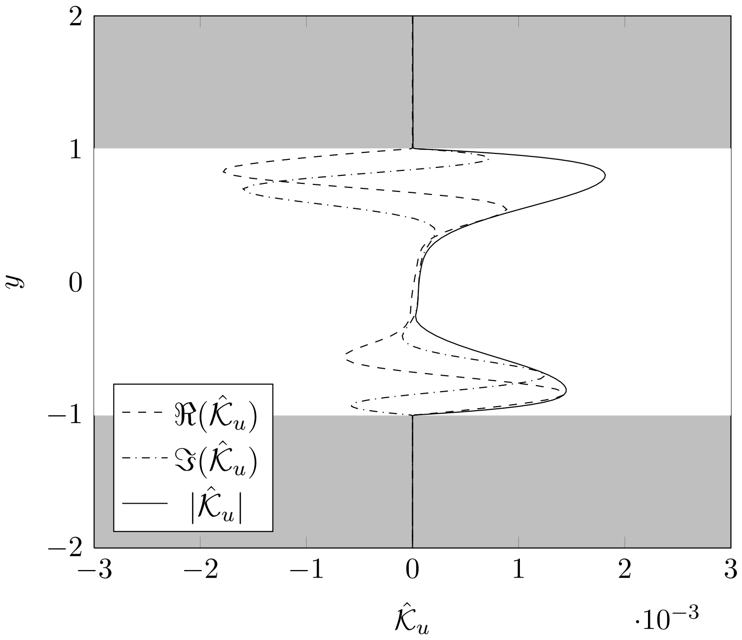

(a) Streamwise velocity gains ($\sigma = 0.002$).

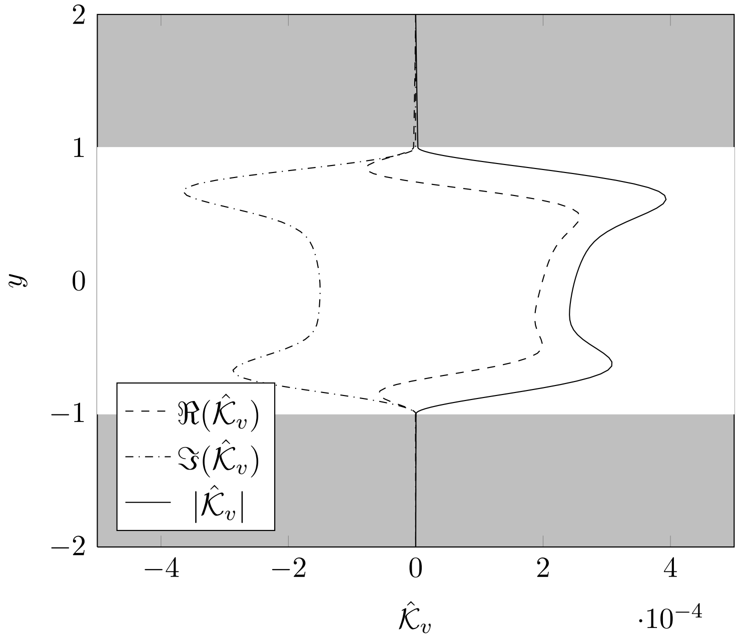

(b) Normal velocity gains ($\sigma = 0.002$).

Figure 5.10: Adjoint of the direct-adjoint controller gains for control input on the upper wall. Top: Streamwise velocity gains. Bottom: Wall-normal velocity gains. Porous layers are symmetric; flow case is $Re_P = 600$, $\kappa_x = 1$, $\kappa_z = 0$, $\sigma = 0.002, \epsilon = 0.6$, $\tau = 0$, $h = 0.5$, $\rho = 1000$. Spanwise velocity gains are zero (not shown).

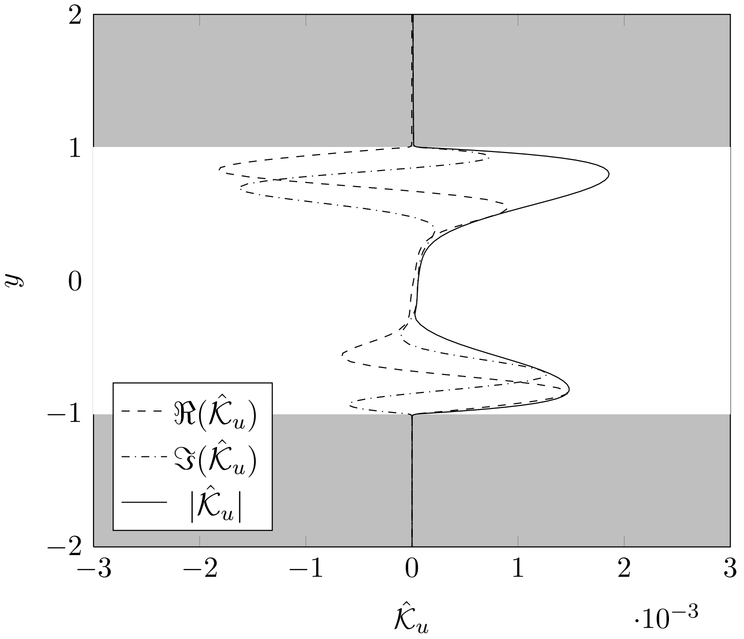

(a) Streamwise velocity gains ($\sigma = 0.004$).

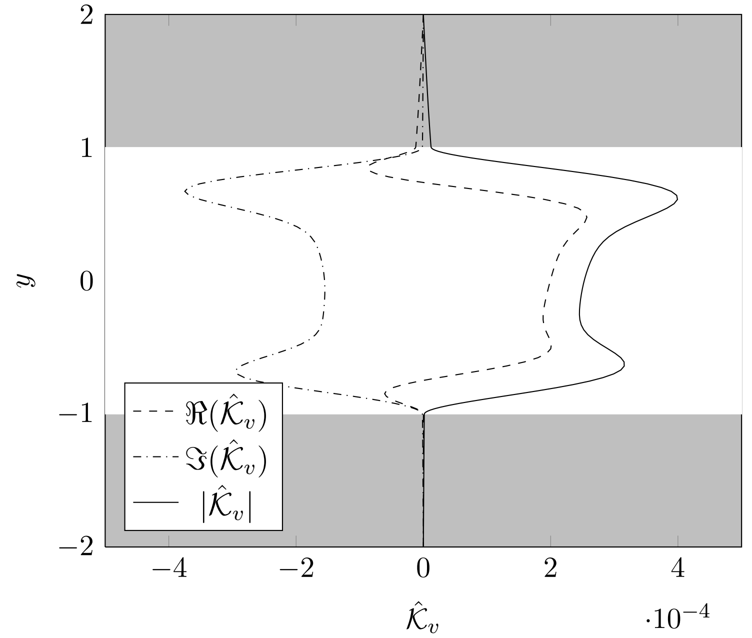

(b) Normal velocity gains ($\sigma = 0.004$).

Figure 5.11: Adjoint of the direct-adjoint controller gains for control input on the upper wall. Top: Streamwise velocity gains. Bottom: Wall-normal velocity gains. Porous layers are symmetric; flow case is $Re_P = 600,\ \kappa_x = 1,\ \kappa_z = 0,\ \sigma = 0.004, \epsilon = 0.6,\ \tau = 0,\ h = 0.5,\ \rho = 1000$. Spanwise velocity gains are zero (not shown).

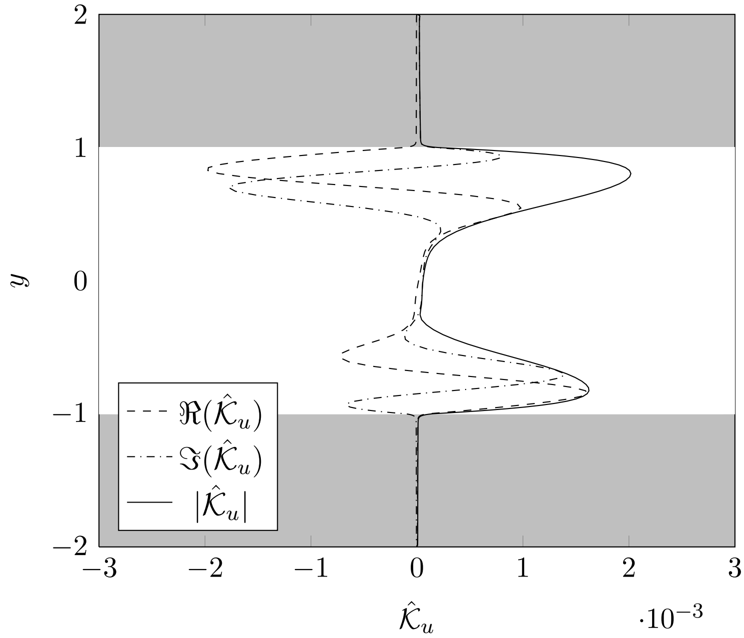

(a) Streamwise velocity gains ($\sigma = 0.008$).

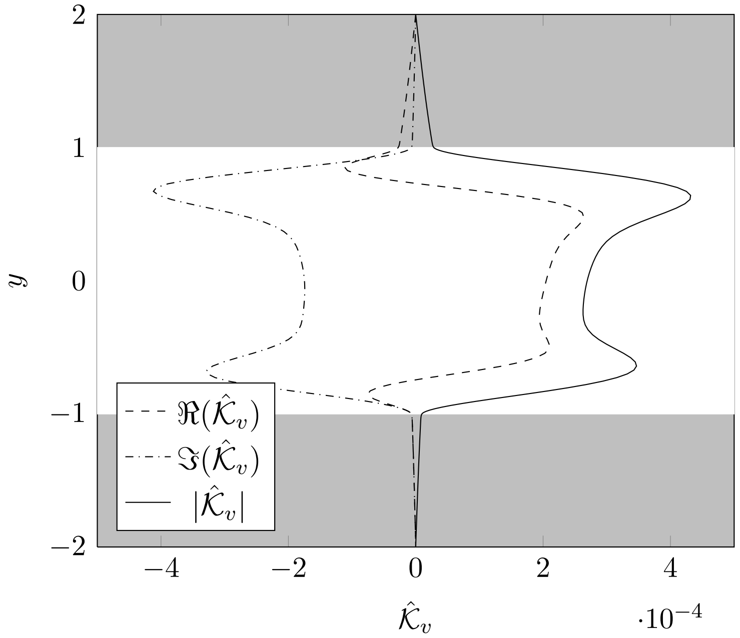

(b) Normal velocity gains ($\sigma = 0.008$).

Figure 5.12: Adjoint of the direct-adjoint controller gains for control input on the upper wall. Top: Streamwise velocity gains. Bottom: Wall-normal velocity gains. Porous layers are symmetric; flow case is $Re_P = 600$, $\kappa_x = 1$, $\kappa_z = 0$, $\sigma = 0.008, \epsilon = 0.6$, $\tau = 0$, $h = 0.5$, $\rho = 1000$. Spanwise velocity gains are zero (not shown).

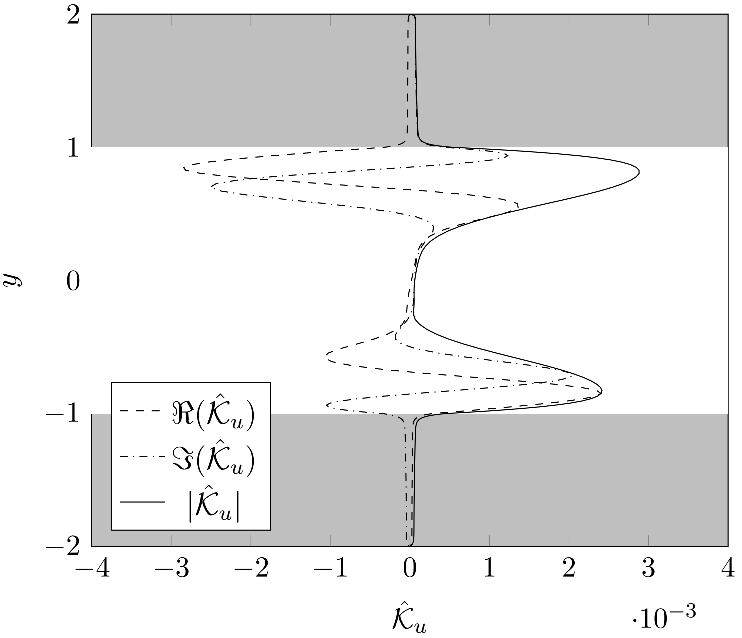

(a) Streamwise velocity gains ($\sigma = 0.016$).

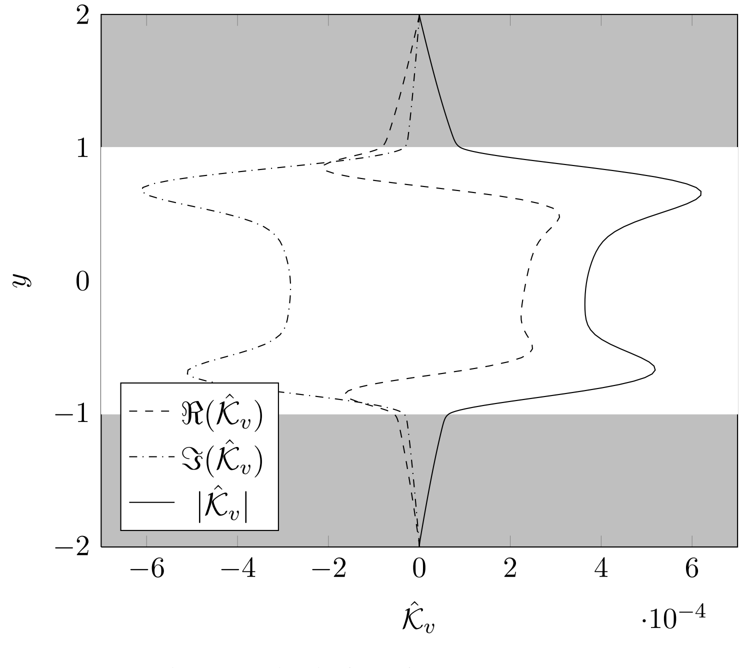

(b) Normal velocity gains ($\sigma = 0.016$).

Figure 5.13: Adjoint of the direct-adjoint controller gains for control input on the upper wall. Top: Streamwise velocity gains. Bottom: Wall-normal velocity gains. Porous layers are symmetric; flow case is $Re_P = 600,\ \kappa_x = 1,\ \kappa_z = 0,\ \sigma = 0.016, \epsilon = 0.6,\ \tau = 0,\ h = 0.5,\ \rho = 1000$. Spanwise velocity gains are zero (not shown).

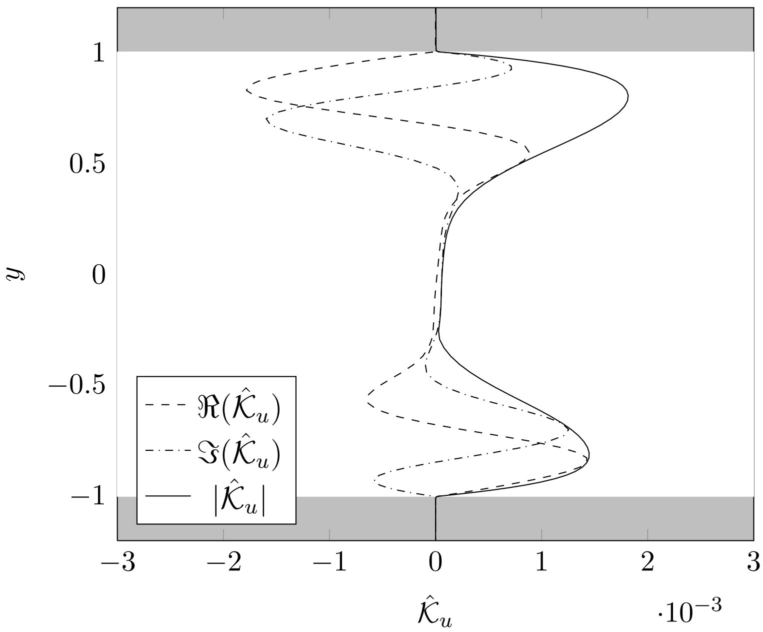

(a) Streamwise velocity gains ($h = 0.1$).

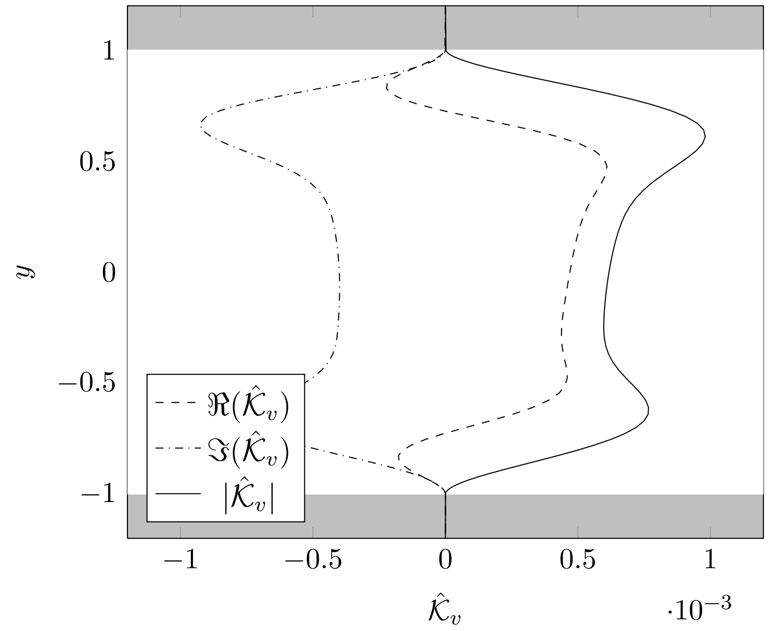

(b) Normal velocity gains ($h = 0.1$).

Figure 5.14: Adjoint of the direct-adjoint controller gains for control input on the upper wall. Top: Streamwise velocity gains. Bottom: Wall-normal velocity gains. Porous layers are symmetric; flow case is $Re_P = 600,\ \kappa_x = 1,\ \kappa_z = 0,\ \sigma = 0.002, \epsilon = 0.6,\ \tau = 0,\ h = 0.1,\ \rho = 1000$. Spanwise velocity gains are zero (not shown).

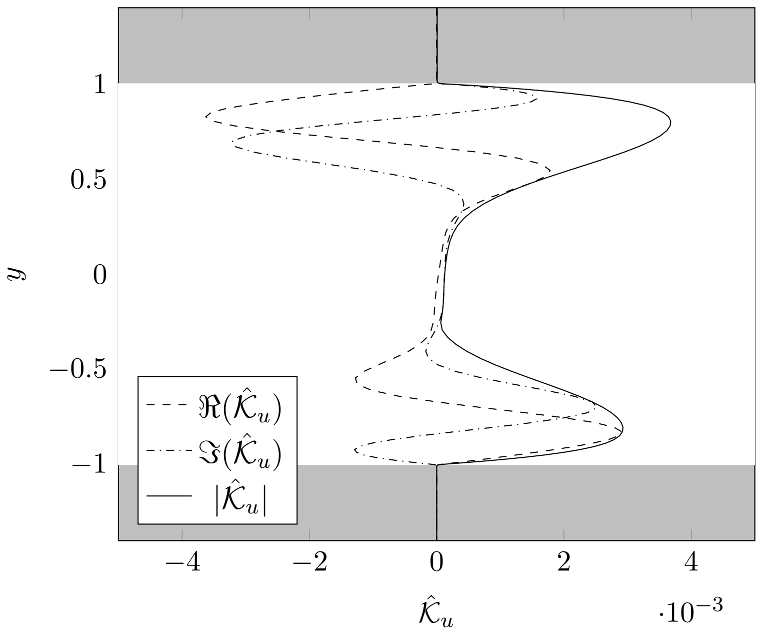

(a) Streamwise velocity gains ($h = 0.2$).

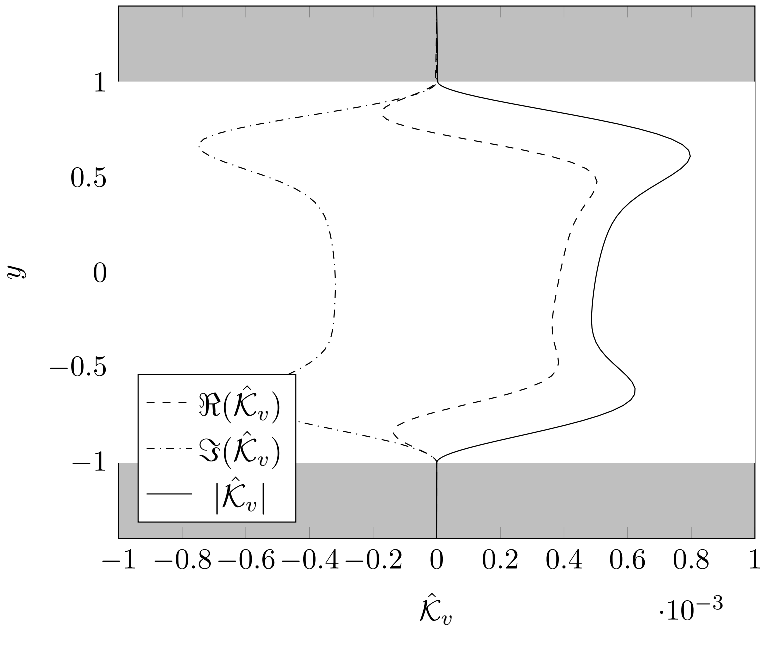

(b) Normal velocity gains ($h = 0.2$).

Figure 5.15: Adjoint of the direct-adjoint controller gains for control input on the upper wall. Top: Streamwise velocity gains. Bottom: Wall-normal velocity gains. Porous layers are symmetric; flow case is $Re_P = 600$, $\kappa_x = 1$, $\kappa_z = 0$, $\sigma = 0.002, \epsilon = 0.6$, $\tau = 0$, $h = 0.2$, $\rho = 1000$. Spanwise velocity gains are zero (not shown).

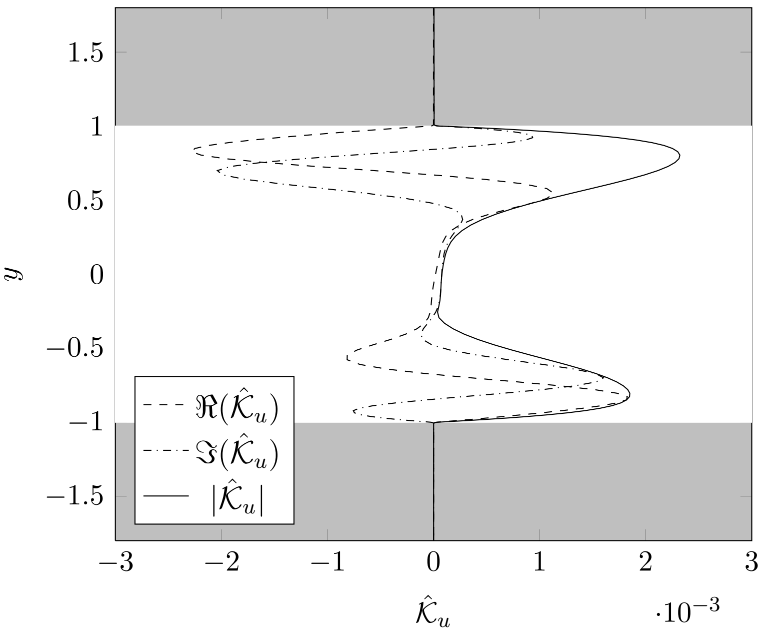

(a) Streamwise velocity gains ($h = 0.4$).

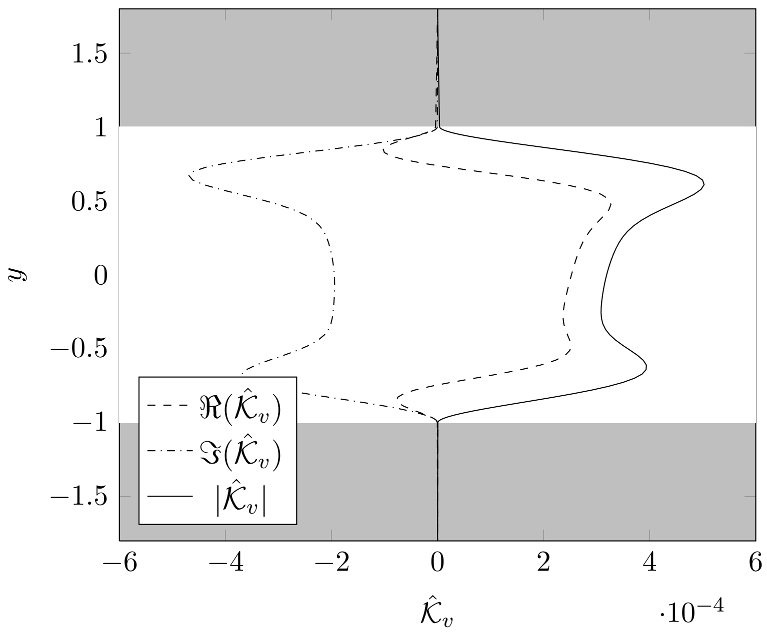

(b) Normal velocity gains ($h = 0.4$).

Figure 5.16: Adjoint of the direct-adjoint controller gains for control input on the upper wall. Top: Streamwise velocity gains. Bottom: Wall-normal velocity gains. Porous layers are symmetric; flow case is $Re_P = 600,\ \kappa_x = 1,\ \kappa_z = 0,\ \sigma = 0.002, \epsilon = 0.6,\ \tau = 0,\ h = 0.4,\ \rho = 1000$. Spanwise velocity gains are zero (not shown).

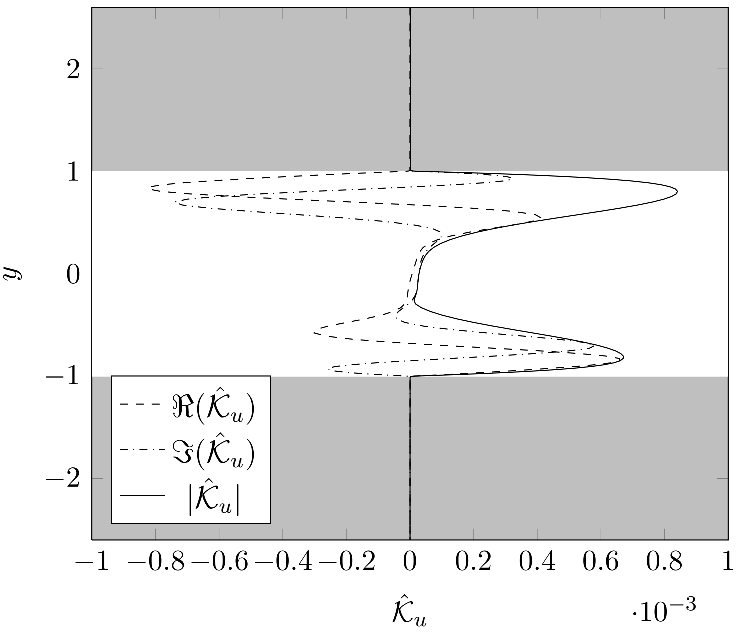

(a) Streamwise velocity gains ($h = 0.8$).

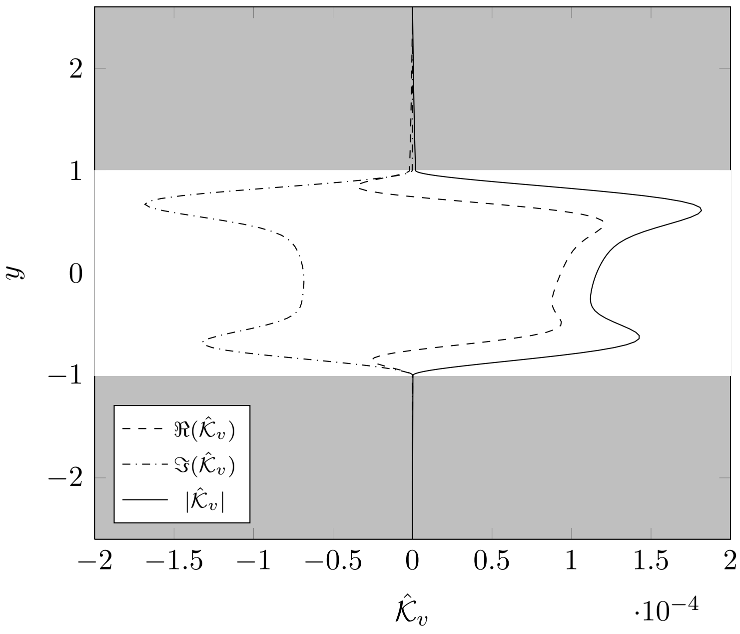

(b) Normal velocity gains ($h = 0.8$).

Figure 5.17: Adjoint of the direct-adjoint controller gains for control input on the upper wall. Top: Streamwise velocity gains. Bottom: Wall-normal velocity gains. Porous layers are symmetric; flow case is $Re_P = 600$, $\kappa_x = 1$, $\kappa_z = 0$, $\sigma = 0.002, \epsilon = 0.6$, $\tau = 0$, $h = 0.8$, $\rho = 1000$. Spanwise velocity gains are zero (not shown).

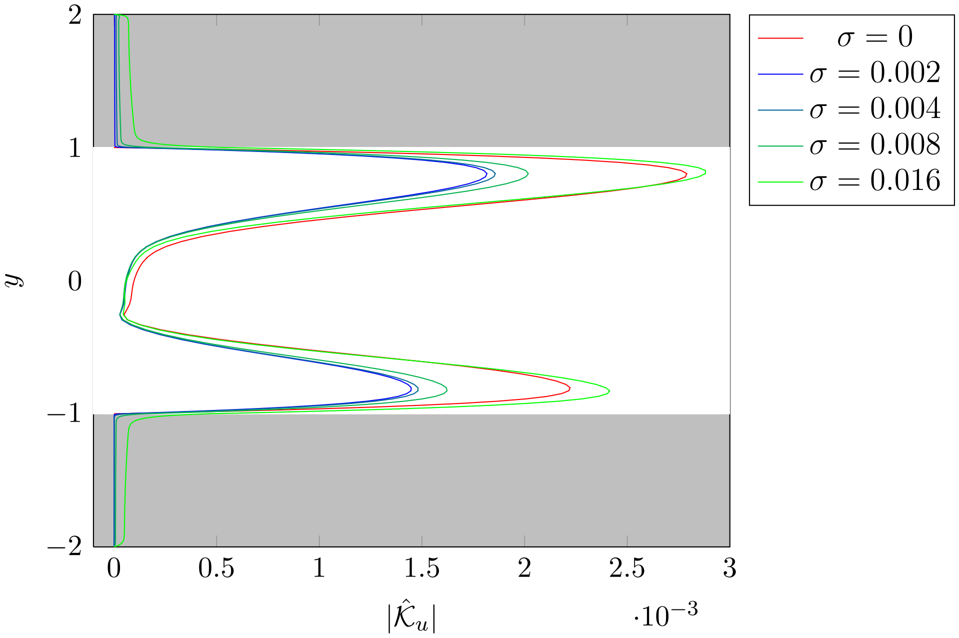

(a) Streamwise velocity gains ($h = 0.5$).

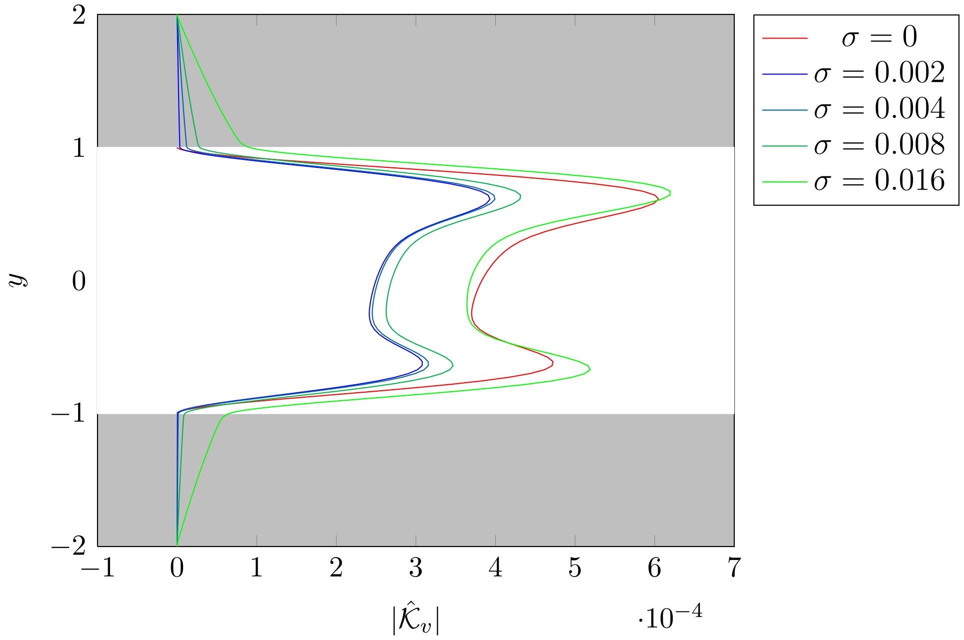

(b) Normal velocity gains ($h = 0.5$).

Figure 5.18: Adjoint of the direct-adjoint controller gains for control input on the upper wall. Top: Streamwise velocity gains. Bottom: Wall-normal velocity gains. Comparison for different values of permeability. Porous layers are symmetric; flow case is $Re_P = 600,\ \kappa_x = 1,\ \kappa_z = 0,\ \epsilon = 0.6,\ \tau = 0,\ h = 0.5,\ \rho = 1000$. Spanwise velocity gains are zero (not shown).

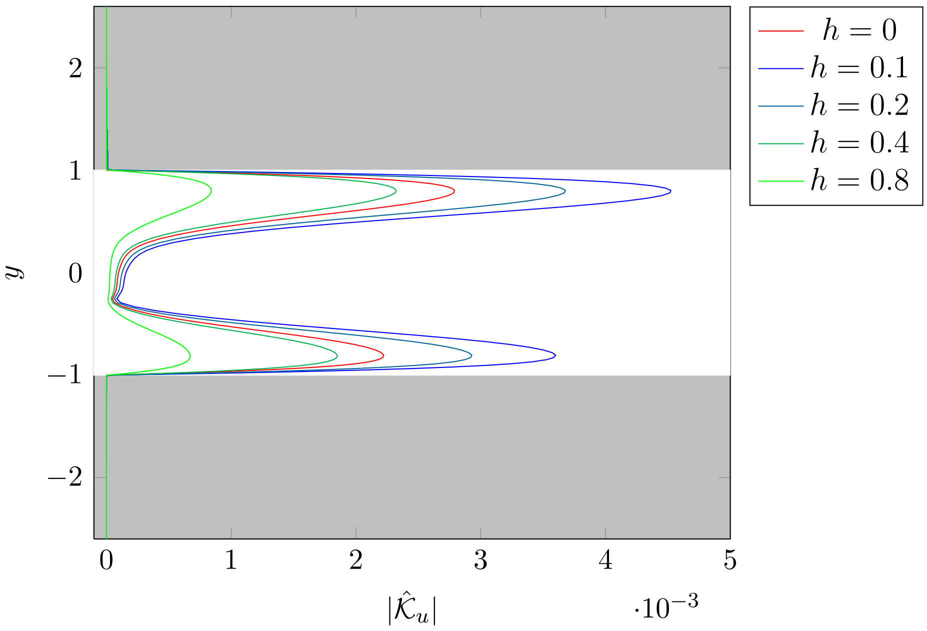

(a) Streamwise velocity gains ($\sigma = 0.002$).

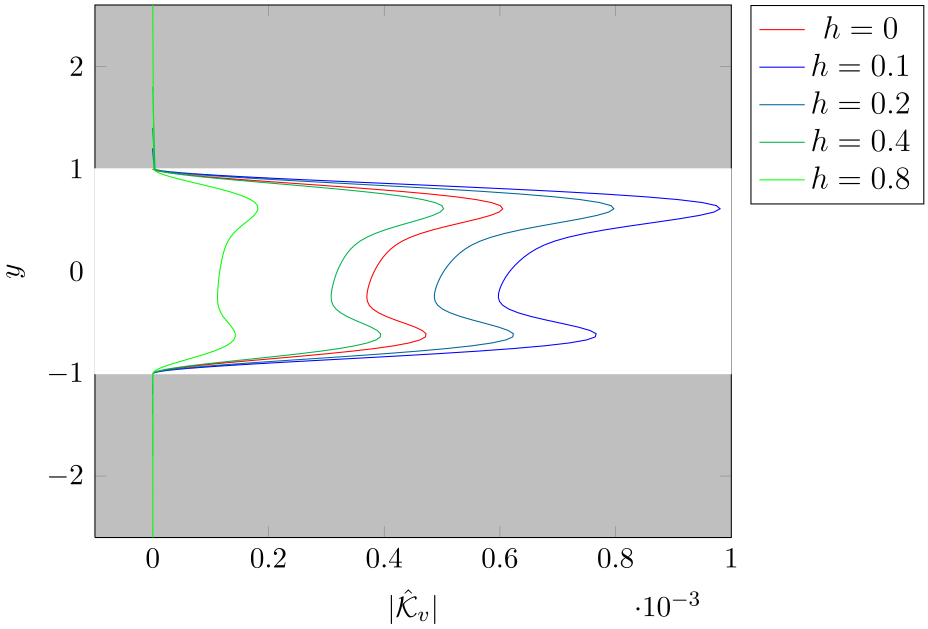

(b) Normal velocity gains ($\sigma = 0.002$).

Figure 5.19: Adjoint of the direct-adjoint controller gains for control input on the upper wall. Top: Streamwise velocity gains. Bottom: Wall-normal velocity gains. Comparison for different values of porous layers height. Porous layers are symmetric; flow case is $Re_P = 600$, $\kappa_x = 1$, $\kappa_z = 0$, $\epsilon = 0.6$, $\tau = 0$, $\sigma = 0.002$, $\rho = 1000$. Spanwise velocity gains are zero (not shown).

and phase margins of $\pm 60^\circ$ for each state variable [106, 109]. LQR robustness to model uncertainties guarantees that gains computed from a model system can be, at worst, half of the gains needed by the actual plant without destabilizing it.

Figures 5.20 and 5.21 try to condense some information about LQRs gain margins, using the L^2 norms of the velocity gains. It is shown how gain norms for the minimum energy controller increase with permeability and porous layer height, causing the gain norms for the impermeable case to be less than the gain reduction limit of the permeable cases. If the permeable model is assumed to better approximate the actual plant, then the application of LQR gains computed from an impermeable model on an actual plant would not have any stability guarantee. These considerations should be carefully revisited for higher values of controller authorities. Figures 5.22 and 5.23 show the same curves computed for the ADA controller at $\rho = 1000$ (still a relatively high value of control weight). As noted in the previous section, trends for increasing permeability and porous layers height are opposed. These two figures tell a different story: For moderate values of permeability and porous layers height, the impermeable case now falls into the stability margins of the permeable cases.

Surely, the range of values considered here is limited and should be extended to still higher degrees of controller authority to get more insight into the controller modifications brought by the porous model. Permeability parameters, control weight and the choice of the state norm could significantly influence the results. From these preliminary computations, it is impossible to get definitive conclusions about plane channel flow controllers robustness in a real experimental application; model uncertainties seem to be serious issues, to be investigated with both theoretical and experimental tools.

All the considerations about robustness should be further investigated after the development of an optimal observer and the implementation of a loop transfer recovery (LTR) procedure for the optimal compensator.

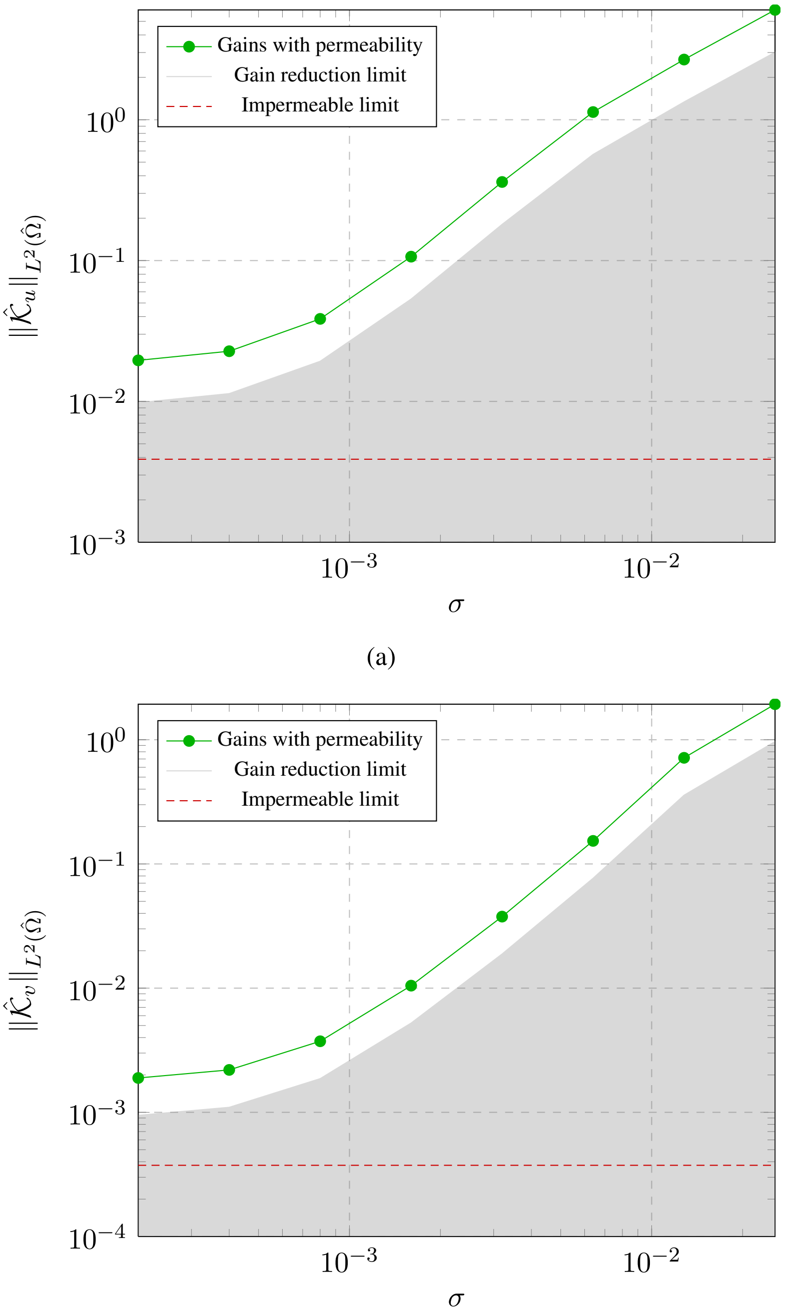

(a)

(b)

Figure 5.20: Minimum energy controller - Gains amplification with increasing permeability. Comparison between the gain reduction limit in the porous case and gains in the impermeable case.

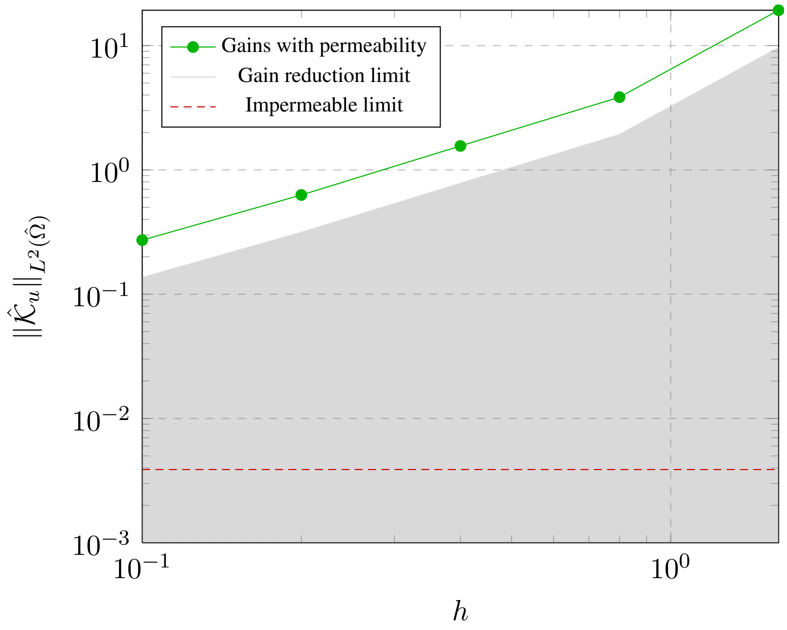

(a)

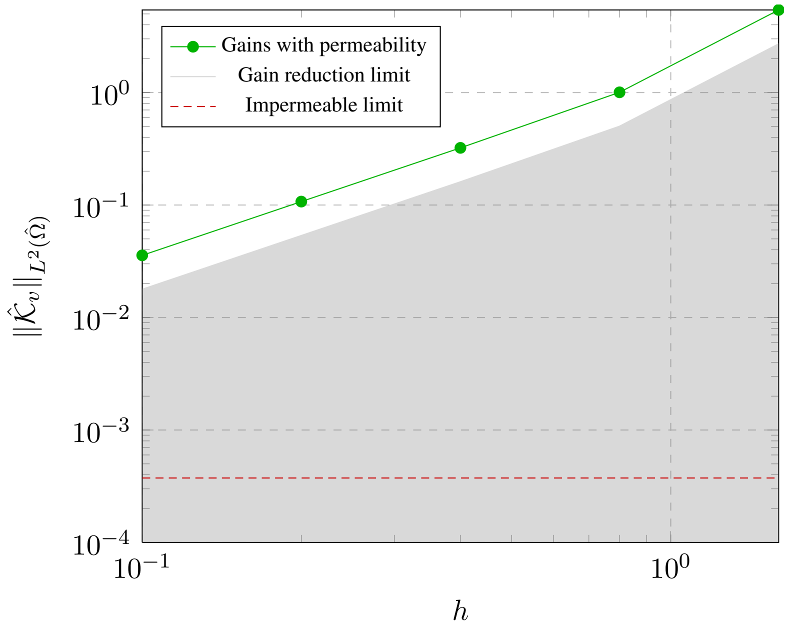

(b)

Figure 5.21: Minimum energy controller - Gains amplification with increasing porous layers height. Comparison between the gain reduction limit in the porous case and gains in the impermeable case.

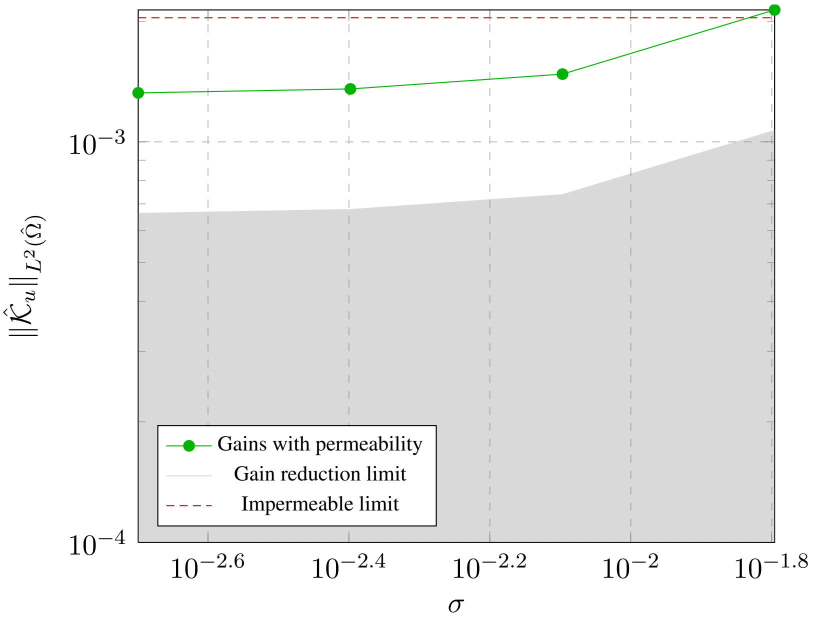

(a)

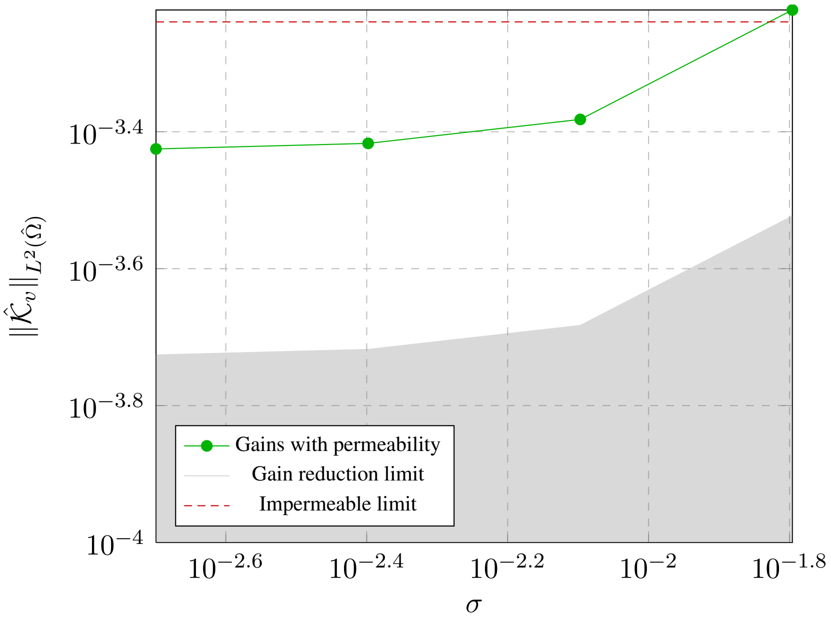

(b)

Figure 5.22: Adjoint of the direct-adjoint - Gains amplification with increasing permeability. Comparison between the gain reduction limit in the porous case and gains in the impermeable case.

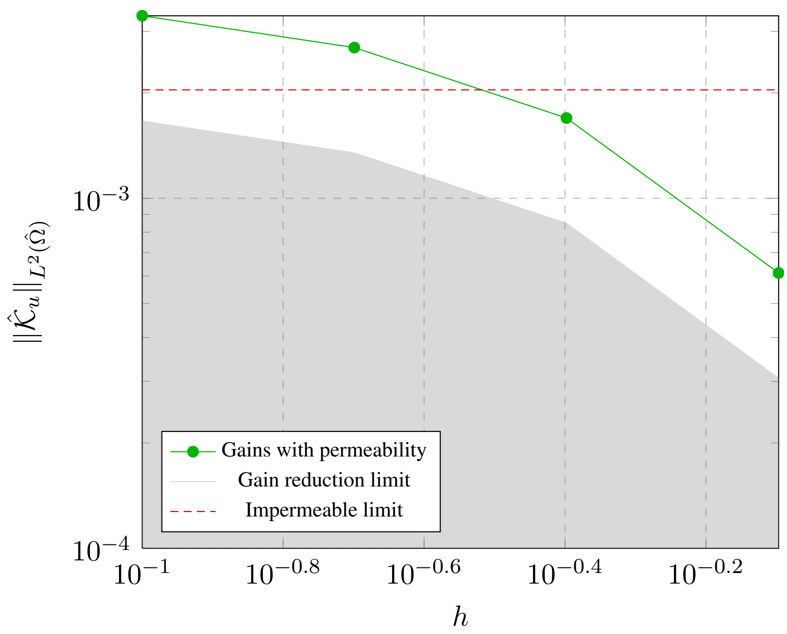

(a)

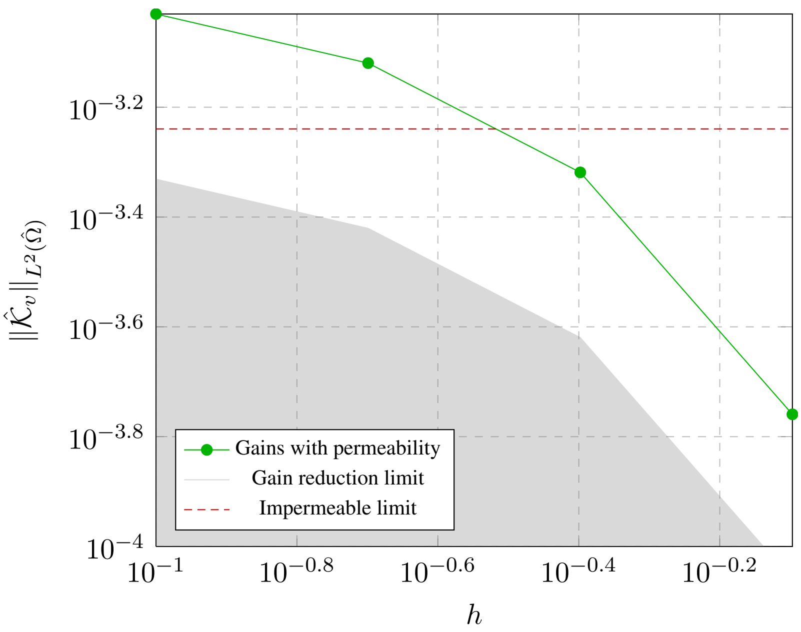

(b)

Figure 5.23: Adjoint of the direct-adjoint controller - Gains amplification with increasing porous layers height. Comparison between the gain reduction limit in the porous case and gains in the impermeable case.

6

Conclusions and future work

This work constitutes a first effort in including a more refined actuator model into the design procedure for plane channel flow optimal controllers.

In the design of the linear quadratic regulator, a continuous distribution of blowing and suction actuation at walls is usually assumed [62]. This is a computationally convenient (but highly idealized) assumption which completely neglects the effects of the finite-size actuators geometry, avoiding the difficulties related to the complete modeling and simulation of a large array of actuators, to be implemented through MEMS technology. Since the implementation of such distributed arrays modifies the channel geometry by covering the walls with a large number of small pores through which fluid transpiration occurs, the modeling of the macroscopic effects of wall-distributed actuators as a permeable layer offers an intermediate design approach.

The volume averaged Navier-Stokes equations (VANS) with the Ochoa-Tapia interface conditions have shown good agreement with experimental data on flow through porous walls [84]. In continuity with the previous works on linear stability [107], transient energy growth [100] and direct numerical simulation [97] of flow in a plane channel bounded by permeable layers, this work has applied the same numerical model to the synthesis of a linear feedback controller.

With respect to standard works on control of plane channel flow, additional mathematical difficulties have arisen with the introduction of permeable layers. The presence of non-trivial boundary and interface conditions makes the *discretize-then-optimize* approach unsuitable for the present case, unless a specific *adjoint consistent* numerical formulation is developed. In the *optimize-then-discretize* approach, standard tools of control systems design (such as the algebraic Riccati equation solution methods) cannot be used. New techniques for the computation of the feedback gains, such as the minimum energy controller [16] and the adjoint of the direct-adjoint controller [103] have to be implemented. The former technique is computationally efficient and allows the computation of feedback gains for all the wavenumber pairs considered in the discretization of the plane channel, while the latter technique requires an iterative optimization procedure which is delicate to automatize for all wavenumber pairs.

Optimal control of channel flow coupled with flow through porous layers poses many mathematical difficulties; the applicability of the minimum energy controller is limited, but the results allow to obtain a preliminary engineering goal. The effects of permeability and the importance of modeling actuator geometry can be assessed from the variations in feedback gains observed when permeability is considered. This work shows that gains magnitude is greatly increased by permeability; actuator geometry is likely to significantly perturb the flow control system, and linear quadratic regulators derived from an impermeable model may not be robust enough in a real application. The adjoint of the direct-adjoint controller gains show different trends when actuator authority is increased, but further investigations are needed to get definitive conclusions about the effects of porosity on feedback gains.

Since permeability is only a first step towards the modeling of a practical distribution of blowing-suction actuators, the effects of the finite-size actuator geometry on flow control can be even more dramatic. The importance of model uncertainties is one of the reasons why simpler feedback control techniques (based on system identification, optimized by means of genetic algorithms) have been preferred to model-based techniques for practical experimental setups [112, 60]. Permeability could provide a simple model to characterize the macroscopic effects of the distributed actuation and a flexible tool to be adjusted to the specific experimental application, while retaining the advantages of a precomputed feedback law. Only the synthesis and analysis of the full-state feedback controller have been targeted in this work; while an observer is in order for any practical application, theoretical investigation of the full-state controller alone could provide meaningful hints for the development of either improved observers or simpler feedback techniques.

This work could be extended to consider higher authority controllers by the adjoint of the direct-adjoint technique. Linearity allows to compute gains for each wavenumber pair in parallel with no communication among processes; to exploit this property, however, the iterative optimization algorithm should be made robust enough to be fully automatic.

The usage of the pressure integral boundary conditions [94] to algebraically eliminate pressure from the system, together with a lifting procedure in each channel layer and an index reduction procedure could be investigated in order to obtain a nonsingular state-space model system. The optimize-then-discretize approach would lead to a nonsymmetric algebraic Riccati equation, whose solution could be

tried using a modified Newton-Kleinman method with the solution of a Sylvester equation at each iteration [43].
Alternatively, a specific adjoint consistent numerical formulation could be studied, recovering the discretize-then-optimize approach and allowing to try standard (symmetric) algebraic Riccati equation numerical solvers once again. Standard direct and iterative methods for the Riccati equation, however, are limited to small systems. Large scale numerical solvers based on alternating direction implicit (ADI) methods [98] are appealing, but they are designed for real valued systems. For this reason, the discretization of the channel geometry in physical space (rather than in wavenumber space) could be considered, with an appropriate handling of periodic boundary conditions.
Simpler models for porous media, or new models for the wall-distributed actuators, could be considered as well.

A

Chebyshev polynomials and cardinal functions

The basic tools for the usage of Chebyshev polynomials are given in this appendix. For a detailed review about the theory and practice of Chebyshev polynomials and spectral methods, the reader is referred to the books of Boyd [18] and Canuto et al. [22, 23].

A.1 Chebyshev polynomials

Spectral methods were born as a generalization of the Fourier series expansion method for solving boundary value problems [18, 22]. The exponential order of convergence is the main appeal of trigonometric functions, but their usage is limited to periodic domains. Chebyshev polynomials can be interpreted as a "*Fourier series in disguise*" [18] which allows to extend it to nonperiodic domains by the mapping of a reference nonperiodic domain $(-1,\ 1)$ to the periodic domain $(0,\ \pi)$

$$y = \cos(\theta) \tag{A.1}$$

Then the Chebyshev polynomials $T_k(y)$ are defined as

$$T_k\left(\cos(\theta)\right) \equiv \cos(k\theta) \tag{A.2}$$

Due to the domain mapping, Chebyshev polynomials are orthogonal in $L_2(y)$ through the integration weight

$$\rho(y) \equiv \frac{1}{\sqrt{1-y^2}} \tag{A.3}$$

Thanks to separation of variables, an arbitrary function $f(y,t)$ defined on the spatial domain $(-1,\ 1)$ can thus be expanded in a series of $N+1$ Chebyshev polynomials as

$$f(y,t) = \sum_{k=0}^{N} T_k(y)\tilde{f}_k(t) \tag{A.4}$$

Spatial derivatives can be expressed in terms of new Chebyshev coefficients[1]

$$\frac{\partial^q f(y,t)}{\partial y^q} = \sum_{k=0}^{N} T_k(y)\tilde{f}_k^{(q)}(t) \tag{A.5}$$

or in terms of derivatives of the polynomials[2]

$$\frac{\partial^q f(y,t)}{\partial y^q} = \sum_{k=0}^{N} \frac{\mathrm{d}^q T_k}{\mathrm{d}y^q}\tilde{f}_k(t) \tag{A.6}$$

Collocation of the boundary value problem, using the last expression, allows to define the discretization matrices $\mathbf{D}^{(q)}$

$$D_{ij}^{(q)} \equiv \left.\frac{\mathrm{d}^q T_j}{\mathrm{d}y^q}\right|_{y_i} \tag{A.7}$$

A.2 Chebyshev cardinal functions

Cardinal functions are basis function which satisfy the property

$$C_j(y_i) = \delta_{ij} \tag{A.8}$$

They are useful whenever the series expansion (eq. A.4) has to be written in terms of the function nodal values

$$f(y,t) = \sum_{k=0}^{N} C_k(y) f(y_k,t) \tag{A.9}$$

Defining the Gauss - Lobatto grid[3]

$$y_k = \cos\left(\frac{\pi k}{N}\right), \qquad k = 0,\ldots,N \tag{A.10}$$

---

[1] As in the Chebyshev tau method (for example, see [87]). Coefficients $\tilde{f}_k^{(q)}$ are then expressed in terms of coefficients $\tilde{f}_k$.

[2] As in the collocation method described by Schmid and Henningson [101] and employed by Tilton [107] and Scarselli [100].

[3] In the context of spectral methods, grids are chosen as the optimal quadrature points which preserve the spectral accuracy of the method. Depending on the number of boundary points included, they are classified as Gauss (no endpoint included), Gauss - Radau (only one endpoint included) and Gauss - Lobatto (both endpoints included) grids.

the Chebyshev coefficients can be computed in terms of the function nodal values

$$\tilde{f}_k(t) = \frac{2b_k}{N} \sum_{k=0}^{N} b_k T_k(y) f(y_k, t) \tag{A.11}$$

with $b_0 = b_N = \frac{1}{2},\ b_k = 1$ for $k = 1, \ldots, N-1$.

The last expression allows to define the Chebyshev cardinal functions in terms of Chebyshev polynomials, as

$$C_k(y) \equiv \frac{2}{N} \sum_{m=0}^{N} \frac{1}{p_m} T_m(y_k) T_m(y) \tag{A.12}$$

with $p_0 = p_N = 2,\ p_j = 1$ for $j = 1, \ldots, N-1$.

Collocation on a Gauss - Lobatto grid leads to the definition of the discretization matrix $\mathbf{D}^{(0)}$

$$D_{ij}^{(0)} = C_j(y_i) = \delta_{ij} \quad i, j = 0, \ldots, N \tag{A.13}$$

and the explicit expression for the first order derivation matrix $\mathbf{D}^{(1)}$ entries (from [18, 22])

$$D_{ij}^{(1)} \equiv \left.\frac{\mathrm{d}C_j}{\mathrm{d}y}\right|_{y_i} = \begin{cases} \dfrac{1+2N^2}{6} & i = j = 0 \\ -\dfrac{1+2N^2}{6} & i = j = N \\ -\dfrac{y_j}{2\left(1-y_j^2\right)} & i = j,\ 0 < j < N \\ \dfrac{(-1)^{i+j} p_i}{p_j\left(y_i - y_j\right)} & i \neq j \end{cases} \tag{A.14}$$

Collocation with cardinal functions allows to define higher order derivatives in a recursive manner

$$\begin{aligned} \left.\frac{\partial^q f(y,t)}{\partial y^q}\right|_{y_i} &= \sum_{j=0}^{N} \left.\frac{\mathrm{d}^q C_j}{\mathrm{d}y^q}\right|_{y_i} f(y_j, t) \\ \left.\frac{\partial^q f(y,t)}{\partial y^q}\right|_{y_i} &= \sum_{j=0}^{N} \left.\frac{\mathrm{d}C_j}{\mathrm{d}y}\right|_{y_i} \left.\frac{\partial^{q-1} f(y,t)}{\partial y^{q-1}}\right|_{y_j} = \\ &= \sum_{j=0}^{N} \left.\frac{\mathrm{d}C_j}{\mathrm{d}y}\right|_{y_i} \sum_{k=0}^{N} \left.\frac{\mathrm{d}C_k}{\mathrm{d}y}\right|_{y_j} \left.\frac{\partial^{q-2} f(y,t)}{\partial y^{q-2}}\right|_{y_k} = \ldots \end{aligned} \tag{A.15}$$

Thus, higher order derivation matrices $\mathbf{D}^{(q)}$ can be obtained by matrix multiplication of the first order derivation matrix

$$\mathbf{D}^{(q)} \equiv \left(\mathbf{D}^{(1)}\right)^q \tag{A.16}$$

A.3 Integration weights

Spectrally accurate integration weights to be used with Chebyshev cardinal functions

$$\int_{-1}^{1} f(y)\,\mathrm{d}y \simeq \sum_{j=0}^{N} w_j f(y_j) \tag{A.17}$$

are derived in the appendix of [45] and successfully used in the same work and in [25]

$$w_k = \frac{b_k}{N}\left(2 + \sum_{n=2}^{N} 2b_n \frac{1+(-1)^n}{1-n^2}\cos\left(\frac{nk\pi}{N}\right)\right) \tag{A.18}$$

with $b_0 = b_N = \frac{1}{2}$, $b_k = 1$ for $k = 1, \ldots, N-1$.

A.4 Domain mapping for porous layers

In order to use standard Chebyshev polynomials and cardinal functions, each channel subdomain has to be mapped into the reference domain $(-1,\ 1)$. Thanks to the definition of the length scale $\mathcal{L} = h$, the central channel region is already defined in $(-1,\ 1)$.

Defining the shift δ_j of each porous layer centerline from the channel centerline and the layer half-height h_j, a new coordinate $\xi_j \in (-1,\ 1)$ can be defined in each porous layer through the mapping

$$\xi_j \equiv \frac{h}{h_j}\,(y - \delta_j) \tag{A.19}$$

Spatial derivatives and integration in the porous regions are then scaled according to the transformations

$$\begin{aligned}
\frac{\partial^q}{\partial y^q}(\ldots) &= \left(\frac{h}{h_j}\right)^q \frac{\partial^q}{\partial \xi_j^q}(\ldots) \\
\int_{\delta_j-h_j}^{\delta_j+h_j} (\ldots)\,\mathrm{d}y &= \frac{h_j}{h}\int_{-1}^{1}(\ldots)\,\mathrm{d}\xi_j
\end{aligned} \tag{A.20}$$

B

Adjoint operator

A short review of the adjoint operator theory and application is given in this appendix. First, the applications and the general derivation method for the adjoint operator are presented (section B.1). Then, the adjoint problem for the problem analyzed in this thesis is derived (section B.2).

B.1 Motivation and technique

Adjoint-based methods are widely used in physics and engineering fields involving optimization, since they allow to efficiently compute the sensitivity of an objective functional to the design parameters. Applications include, for example, sensitivity analysis, a posteriori error analysis for automatic grid adaptation, shape optimization and control system design.

To better understand the technique behind the adjoint operator, its historical development will be followed. In linear algebra, the *adjoint* of a matrix $\mathbf{A}$ simply is its conjugate-transpose $\mathbf{A}^H$. Given an arbitrary $m \times n$ linear system

$$\mathbf{A}\mathbf{u} = \mathbf{b} \tag{B.1}$$

the *adjoint* $n \times m$ system

$$\mathbf{A}^H\mathbf{v} = \mathbf{c} \tag{B.2}$$

plays an important role in its solvability. In fact, the necessary and sufficient condition for the solvability of an arbitrary $m \times n$ system is that the right side is orthogonal to all linearly independent solutions of the adjoint homogeneous system.

In the finite-dimensional setting, it is easy to see that the *bilinear identity* holds

$$\mathbf{v}^H\mathbf{A}\mathbf{u} = \mathbf{u}^H\mathbf{A}^H\mathbf{v} \tag{B.3}$$

Matrix $\mathbf{A}$ can be a numerical approximation of an infinite-dimensional operator $\mathcal{A}$, provided with its own boundary conditions. In the infinite-dimensional setting, the definition of the inner product needs to include a volume integral

$$\langle \mathbf{v},\ \mathbf{u} \rangle_{L^2(\Omega)} \equiv \int_\Omega \mathbf{v}^H \mathbf{u} \, \mathrm{d}\Omega \tag{B.4}$$

but we wish to define the adjoint operator $\mathcal{A}^\dagger$ by an extended bilinear (Green's) identity

$$\langle \mathbf{v},\ \mathcal{A}\mathbf{u} \rangle_{L^2(\Omega)} = \langle \mathbf{u},\ \mathcal{A}^\dagger \mathbf{v} \rangle_{L^2(\Omega)} \tag{B.5}$$

This is possible thanks to Riesz's representation theorem, which says that for each linear functional acting on a function $\mathbf{u}$ there exist a unique function $\mathbf{w}$ such as the functional can be represented as an inner product between $\mathbf{u}$ and $\mathbf{w}$

$$\mathcal{J}[\mathbf{u}] = \langle \mathbf{w},\ \mathbf{u} \rangle_{L^2(\Omega)} \tag{B.6}$$

Then, defining the functional

$$\mathcal{J}[\mathbf{u}] \equiv \langle \mathbf{v},\ \mathcal{A}\mathbf{u} \rangle_{L^2(\Omega)} \tag{B.7}$$

the Riesz's element can be identified as

$$\mathbf{w} \equiv \mathcal{A}^\dagger \mathbf{v} \tag{B.8}$$

and it is easy to see that the bilinear identity holds in the infinite-dimensional setting also.

The adjoint operator $\mathcal{A}^\dagger$ can thus be derived integrating by parts the inner product $\langle \mathbf{v},\ \mathcal{A}\mathbf{u} \rangle_{L^2(\Omega)}$ and moving the action of the differential operators onto the adjoint variable $\mathbf{v}$. Thanks to Riesz's theorem, all the boundary terms arising from the integration process must vanish: Imposition of this property allows to compute the adjoint boundary conditions.

The discussion has been presented for linear differential operators in *space*, but it can be readily extended to differential problems in both *time and space* by an appropriate redefinition of the inner product.

From the above discussion, it can be seen that the adjoint operator strongly depends on the choice of the functional from which it is derived. For stability analyses, the standard approach is to take the inner product of the direct problem $\mathcal{E}\frac{\partial \mathbf{u}}{\partial t} = \mathcal{A}\mathbf{u}$ with the adjoint variable $\mathbf{v}$, implicitly defining the linear functional

$$\mathcal{J}[\mathbf{u}] \equiv \int_0^T \langle \mathbf{v},\ \mathcal{E}\frac{\partial \mathbf{u}}{\partial t} - \mathcal{A}\mathbf{u} \rangle_{L^2(\Omega)} \, \mathrm{d}t \tag{B.9}$$

which allows to uniquely define the adjoint operators $\mathcal{E}^\dagger$ and $\mathcal{A}^\dagger$.

For optimal control problems, the constrained objective functional (see chapter 2) of the problem at hand leads to specific definitions of the adjoint operators.

A complete discussion about the adjoint operator is beyond the scope of the present appendix. For a clear presentation of the adjoint operator and its boundary conditions, the reader is strongly referred to chapter 4 of the book of Lanczos [65]; for an application-oriented viewpoint, the articles of Giles and Pierce [40, 39] and Luchini and Bottaro [72] give a review of adjoint-based methods in Computational Fluid Dynamics.

B.2 Adjoint problem for the incompressible flow in a plane channel with porous walls

Since the adjoint problem strongly depends on the choice of the linear functional and the form of the direct equations[1], here the adjoint equations are derived in wavenumber space (defining $\alpha = \kappa_x$ and $\beta = \kappa_z$ for convenience of notation) from the linearized Navier-Stokes momentum and continuity equations

$$\begin{aligned}\frac{\partial \hat{u}}{\partial t} - \frac{1}{Re}\left(\frac{\partial^2}{\partial y^2} - \kappa^2\right)\hat{u} + i\alpha U(y)\hat{u} + U'(y)\hat{v} + i\alpha\hat{p} &= 0\\ \frac{\partial \hat{v}}{\partial t} - \frac{1}{Re}\left(\frac{\partial^2}{\partial y^2} - \kappa^2\right)\hat{v} + i\alpha U(y)\hat{v} + \frac{\partial \hat{p}}{\partial y} &= 0\\ \frac{\partial \hat{w}}{\partial t} - \frac{1}{Re}\left(\frac{\partial^2}{\partial y^2} - \kappa^2\right)\hat{w} + i\alpha U(y)\hat{w} + i\beta\hat{p} &= 0\\ i\alpha\hat{u} + \frac{\partial \hat{v}}{\partial y} + i\beta\hat{w} &= 0\end{aligned} \tag{B.10}$$

and the Volume-Averaged Navier-Stokes momentum and continuity equations

$$\begin{aligned}\frac{1}{\epsilon_j}\frac{\partial\langle\hat{u}\rangle_j}{\partial t} + \frac{1}{\sigma_j^2 Re}\langle\hat{u}\rangle_j - \frac{1}{\epsilon_j Re}\left(\frac{\partial^2}{\partial y^2} - \kappa^2\right)\langle\hat{u}\rangle_j + i\alpha\langle\hat{p}\rangle_j^f &= 0\\ \frac{1}{\epsilon_j}\frac{\partial\langle\hat{v}\rangle_j}{\partial t} + \frac{1}{\sigma_j^2 Re}\langle\hat{v}\rangle_j - \frac{1}{\epsilon_j Re}\left(\frac{\partial^2}{\partial y^2} - \kappa^2\right)\langle\hat{v}\rangle_j + \frac{\partial\langle\hat{p}\rangle_j^f}{\partial y} &= 0\\ \frac{1}{\epsilon_j}\frac{\partial\langle\hat{w}\rangle_j}{\partial t} + \frac{1}{\sigma_j^2 Re}\langle\hat{w}\rangle_j - \frac{1}{\epsilon_j Re}\left(\frac{\partial^2}{\partial y^2} - \kappa^2\right)\langle\hat{w}\rangle_j + i\beta\langle\hat{p}\rangle_j^f &= 0\\ i\alpha\langle\hat{u}\rangle_j + \frac{\partial\langle\hat{v}\rangle_j}{\partial y} + i\beta\langle\hat{w}\rangle_j &= 0\end{aligned} \tag{B.11}$$

---

[1] For example, the simple scaling of a direct *equation* produces the scaling of an adjoint *variable*.

provided with the boundary and interface conditions defined in chapter 3. The Poisson and Laplace adjoint pressure equations are derived only *after* the derivation of the adjoint operator.

Using the functional in eq. B.9 and defining the adjoint variables $(\hat{\bar{\mathbf{u}}}, \hat{\bar{p}})$, $(\langle\hat{\bar{\mathbf{u}}}\rangle, \langle\hat{\bar{p}}\rangle)$, the extended Green's identity for channel layer reads

$$
\begin{aligned}
\int\limits_0^T \int\limits_{-h}^{h} \Bigg\{ \hat{\bar{u}}^* \left[\frac{\partial \hat{u}}{\partial t} - \frac{1}{Re}\left(\frac{\partial^2}{\partial y^2} - \kappa^2 \right) \hat{u} + i\alpha U(y)\hat{u} + U'(y)\hat{v} + i\alpha\hat{p} \right] + \\
\hat{\bar{v}}^* \left[\frac{\partial \hat{v}}{\partial t} - \frac{1}{Re}\left(\frac{\partial^2}{\partial y^2} - \kappa^2 \right) \hat{v} + i\alpha U(y)\hat{v} + \frac{\partial \hat{p}}{\partial y} \right] + \\
\hat{\bar{w}}^* \left[\frac{\partial \hat{w}}{\partial t} - \frac{1}{Re}\left(\frac{\partial^2}{\partial y^2} - \kappa^2 \right) \hat{w} + i\alpha U(y)\hat{w} + i\beta\hat{p} \right] + \\
\hat{\bar{p}}^* \left(i\alpha\hat{u} + \frac{\partial \hat{v}}{\partial y} + i\beta\hat{w} \right) \Bigg\} \,\mathrm{d}y\,\mathrm{d}t = \\
\int\limits_0^T \int\limits_{-h}^{h} \Bigg\{ \hat{u} \left[-\frac{\partial \hat{\bar{u}}^*}{\partial t} - \frac{1}{Re}\left(\frac{\partial^2}{\partial y^2} - \kappa^2 \right) \hat{\bar{u}}^* + i\alpha U(y)\hat{\bar{u}}^* + i\alpha\hat{\bar{p}}^* \right] + \\
\hat{v} \left[-\frac{\partial \hat{\bar{v}}^*}{\partial t} - \frac{1}{Re}\left(\frac{\partial^2}{\partial y^2} - \kappa^2 \right) \hat{\bar{v}}^* + i\alpha U(y)\hat{\bar{v}}^* + U'(y)\hat{\bar{v}}^* - \frac{\partial \hat{\bar{p}}^*}{\partial y} \right] + \\
\hat{w} \left[-\frac{\partial \hat{\bar{w}}^*}{\partial t} - \frac{1}{Re}\left(\frac{\partial^2}{\partial y^2} - \kappa^2 \right) \hat{\bar{w}}^* + i\alpha U(y)\hat{\bar{w}}^* + i\beta\hat{\bar{p}}^* \right] + \\
\hat{p} \left(i\alpha\hat{\bar{u}}^* - \frac{\partial \hat{\bar{v}}^*}{\partial y} + i\beta\hat{\bar{w}}^* \right) \Bigg\} \,\mathrm{d}y\,\mathrm{d}t + \\
\int\limits_{-h}^{h} \left[\hat{\bar{\mathbf{u}}}^* \cdot \hat{\mathbf{u}} \right]_0^T \mathrm{d}y + \int\limits_0^T \left\{ \frac{1}{Re} \left[\frac{\partial \hat{\bar{\mathbf{u}}}^*}{\partial y} \cdot \hat{\mathbf{u}} - \hat{\bar{\mathbf{u}}}^* \cdot \frac{\partial \hat{\mathbf{u}}}{\partial y} \right]_{-h}^{h} + \left[\hat{\bar{v}}^* \hat{p} + \hat{\bar{p}}^* \hat{v} \right]_{-h}^{h} \right\} \mathrm{d}t
\end{aligned}
\tag{B.12}
$$

Terms in green are the adjoint equations, while terms in red are the boundary terms, which vanish *together with* boundary terms arising from the derivation of the adjoint operator in the porous regions.

In the same way, the extended Green's identity in each porous layer reads

$$
\begin{aligned}
&\int_0^T \int_{\delta_j-h_j}^{\delta_j+h_j} \Bigg\{ \langle \hat{\bar{u}} \rangle_j^* \left[\frac{1}{\epsilon_j} \frac{\partial \langle \hat{u} \rangle_j}{\partial t} + \frac{1}{\sigma_j^2 Re} \langle \hat{u} \rangle_j - \frac{1}{\epsilon_j Re} \left(\frac{\partial^2}{\partial y^2} - \kappa^2 \right) \langle \hat{u} \rangle_j + i\alpha \langle \hat{p} \rangle_j^f \right] + \\
&\qquad \langle \hat{\bar{v}} \rangle_j^* \left[\frac{1}{\epsilon_j} \frac{\partial \langle \hat{v} \rangle_j}{\partial t} + \frac{1}{\sigma_j^2 Re} \langle \hat{v} \rangle_j - \frac{1}{\epsilon_j Re} \left(\frac{\partial^2}{\partial y^2} - \kappa^2 \right) \langle \hat{v} \rangle_j + \frac{\partial \langle \hat{p} \rangle_j^f}{\partial y} \right] + \\
&\qquad \langle \hat{\bar{w}} \rangle_j^* \left[\frac{1}{\epsilon_j} \frac{\partial \langle \hat{w} \rangle_j}{\partial t} + \frac{1}{\sigma_j^2 Re} \langle \hat{w} \rangle_j - \frac{1}{\epsilon_j Re} \left(\frac{\partial^2}{\partial y^2} - \kappa^2 \right) \langle \hat{w} \rangle_j + i\beta \langle \hat{p} \rangle_j^f \right] \\
&\qquad \langle \hat{\bar{p}} \rangle_j^{f*} \left[i\alpha \langle \hat{u} \rangle_j + \frac{\partial \langle \hat{v} \rangle_j}{\partial y} + i\beta \langle \hat{w} \rangle_j \right] \Bigg\} \, \mathrm{d}y \, \mathrm{d}t = \\
&\int_0^T \int_{\delta_j-h_j}^{\delta_j+h_j} \Bigg\{ \langle \hat{u} \rangle_j \left[-\frac{1}{\epsilon_j} \frac{\partial \langle \hat{\bar{u}} \rangle_j^*}{\partial t} + \frac{1}{\sigma_j^2 Re} \langle \hat{\bar{u}} \rangle_j^* - \frac{1}{\epsilon_j Re} \left(\frac{\partial^2}{\partial y^2} - \kappa^2 \right) \langle \hat{\bar{u}} \rangle_j^* + i\alpha \langle \hat{\bar{p}} \rangle_j^{f*} \right] + \\
&\qquad \langle \hat{v} \rangle_j \left[-\frac{1}{\epsilon_j} \frac{\partial \langle \hat{\bar{v}} \rangle_j^*}{\partial t} + \frac{1}{\sigma_j^2 Re} \langle \hat{\bar{v}} \rangle_j^* - \frac{1}{\epsilon_j Re} \left(\frac{\partial^2}{\partial y^2} - \kappa^2 \right) \langle \hat{\bar{v}} \rangle_j^* - \frac{\partial \langle \hat{\bar{p}} \rangle_j^{f*}}{\partial y} \right] + \\
&\qquad \langle \hat{w} \rangle_j \left[-\frac{1}{\epsilon_j} \frac{\partial \langle \hat{\bar{w}} \rangle_j^*}{\partial t} + \frac{1}{\sigma_j^2 Re} \langle \hat{\bar{w}} \rangle_j^* - \frac{1}{\epsilon_j Re} \left(\frac{\partial^2}{\partial y^2} - \kappa^2 \right) \langle \hat{\bar{w}} \rangle_j^* + i\beta \langle \hat{\bar{p}} \rangle_j^{f*} \right] \\
&\qquad \langle \hat{p} \rangle_j^f \left[i\alpha \langle \hat{\bar{u}} \rangle_j^* - \frac{\partial \langle \hat{\bar{v}} \rangle_j^*}{\partial y} + i\beta \langle \hat{\bar{w}} \rangle_j^* \right] \Bigg\} \, \mathrm{d}y \, \mathrm{d}t + \\
&\frac{1}{\epsilon_j} \int_{\delta_j-h_j}^{\delta_j+h_j} \left[\langle \hat{\bar{\mathbf{u}}} \rangle_j^* \cdot \langle \hat{\mathbf{u}} \rangle_j \right]_0^T \mathrm{d}y + \frac{1}{\epsilon_j Re} \int_0^T \left[\frac{\partial \langle \hat{\bar{\mathbf{u}}} \rangle_j^*}{\partial y} \cdot \langle \hat{\mathbf{u}} \rangle_j - \langle \hat{\bar{\mathbf{u}}} \rangle_j^* \cdot \frac{\partial \langle \mathbf{u} \rangle_j}{\partial y} \right]_{\delta_j-h_j}^{\delta_j+h_j} \mathrm{d}t + \\
&\qquad \int_0^T \left[\langle \hat{\bar{v}} \rangle_j^* \langle \hat{p} \rangle_j^f + \langle \hat{\bar{p}} \rangle_j^{f*} \langle \hat{v} \rangle_j \right]_{\delta_j-h_j}^{\delta_j+h_j} \mathrm{d}t
\end{aligned}
\tag{B.13}
$$

Evaluation of *all* the boundary terms at solid walls and interfaces allows to derive the adjoint boundary and interface conditions.

$$
\begin{aligned}
\langle \hat{\hat{\mathbf{u}}} \rangle_j &= \mathbf{0} \qquad \text{on} \quad \Gamma_{w,j} \\
\hat{\hat{\mathbf{u}}} &= \langle \hat{\hat{\mathbf{u}}} \rangle_j \\
\hat{\hat{p}} &= \langle \hat{\hat{p}} \rangle_j^f \\
\frac{\sigma_j}{\epsilon_j} \frac{\partial \langle \hat{\hat{u}} \rangle_j}{\partial y} - \sigma_j \frac{\partial \hat{\hat{u}}}{\partial y} &= \mp \tau_j \hat{\hat{u}} \\
\frac{\sigma_j}{\epsilon_j} \frac{\partial \langle \hat{\hat{w}} \rangle_j}{\partial y} - \sigma_j \frac{\partial \hat{\hat{w}}}{\partial y} &= \mp \tau_j \hat{\hat{w}} \qquad \text{on} \quad \Gamma_{i,j}
\end{aligned}
\tag{B.14}
$$

These conditions are found to be self-adjoint, and also the additional patching conditions on normal velocity are the same.

The adjoint Poisson pressure equations can be derived in the same way explained in section 3.4.4, for both the channel layer

$$
\begin{aligned}
&\frac{\partial}{\partial t} \left(i\alpha \hat{\hat{u}}^* + \frac{\partial}{\partial y} \hat{\hat{v}}^* + i\beta \hat{\hat{w}}^* \right) + + \left(\frac{\partial^2}{\partial y^2} - \kappa^2 \right) \hat{\hat{p}}^* + \\
&\qquad\qquad - U''(y) \hat{\hat{u}}^* - U'(y) \frac{\partial \hat{\hat{u}}^*}{\partial y} - i\alpha U'(y) \hat{\hat{v}}^* = 0
\end{aligned}
\tag{B.15}
$$

and the porous layers

$$
\frac{\partial}{\partial t} \left(i\alpha \langle \hat{\hat{u}} \rangle_j^* + \frac{\partial}{\partial y} \langle \hat{\hat{v}} \rangle_j^* + i\beta \langle \hat{\hat{w}} \rangle_j^* \right) + \left(\frac{\partial^2}{\partial y^2} - \kappa^2 \right) \langle \hat{\hat{p}} \rangle_j^{f*} = 0 \tag{B.16}
$$

C

Normal velocity - normal vorticity formulation

Using the same procedure usually followed for plane channel flow, eq. 3.10 can be reduced to a system of equations for the wall-normal component of velocity v and vorticity η defined as

$$\eta \equiv \frac{\partial u}{\partial z} - \frac{\partial w}{\partial x} \tag{C.1}$$

This is accomplished, in each layer, by writing the momentum equation for the cartesian components of velocity, taking the laplacian of the equation for v, and subtracting the x derivative of the equation for w from the z derivative of the equation for u. Pressure terms vanish from the equation for η, while the laplacian of pressure can be explicitated by taking the laplacian of the continuity equation. The resulting system reads

$$\begin{aligned}
\nabla^2 \frac{\partial}{\partial t} v &= \left(-U(y) \frac{\partial}{\partial x} \nabla^2 + U''(y) \frac{\partial}{\partial x} + \frac{1}{Re} \nabla^4 \right) v \\
\frac{\partial}{\partial t} \eta &= -U'(y) \frac{\partial}{\partial z} v + \left(-U(y) \frac{\partial}{\partial x} + \frac{1}{Re} \nabla^2 \right) \eta \\
\frac{1}{\epsilon_j} \nabla^2 \frac{\partial \langle v \rangle_j}{\partial t} &= \left(-\frac{1}{\sigma_j^2 Re} \nabla^2 + \frac{1}{\epsilon_j Re} \nabla^4 \right) \langle v \rangle_j \\
\frac{1}{\epsilon_j} \frac{\partial \langle \eta \rangle_j}{\partial t} &= \left(-\frac{1}{\sigma_j^2 Re} + \frac{1}{\epsilon_j Re} \nabla^2 \right) \langle \eta \rangle_j
\end{aligned} \tag{C.2}$$

and the streamwise and spanwise velocity components can be recovered from the continuity equation

$$\begin{aligned}
\frac{\partial u}{\partial x} + \frac{\partial w}{\partial z} &= -\frac{\partial v}{\partial y} \\
\frac{\partial u}{\partial z} - \frac{\partial w}{\partial x} &= \eta \\
\frac{\partial \langle u \rangle_j}{\partial x} + \frac{\partial \langle w \rangle_j}{\partial z} &= -\frac{\partial \langle v \rangle_j}{\partial y} \\
\frac{\partial \langle u \rangle_j}{\partial z} - \frac{\partial \langle w \rangle_j}{\partial x} &= \langle \eta \rangle_j
\end{aligned} \tag{C.3}$$

Velocity and vorticity are coupled in the channel layer only. Boundary and interface conditions (eq. B.14) have to be rewritten for normal velocity and normal vorticity; their development is presented after the introduction of the discretization of the streamwise and spanwise directions.

C.1 Boundary and interface conditions in wavenumber space

For the primitive variable formulation, the boundary and interface conditions are already linear and do not change after discretization. With normal velocity-normal vorticity variables, the periodicity assumption introduced by the Fourier series allows to simplify the derivation of the boundary and interface conditions in wavenumber space.

Dirichlet conditions on normal velocity

$$\begin{aligned} \langle \hat{v} \rangle_j &= 0 \qquad && \text{on} \quad \Gamma_{wj} \\ \hat{v} &= \langle \hat{v} \rangle_j \qquad && \text{on} \quad \Gamma_j \end{aligned} \tag{C.4}$$

are already available; Dirichlet conditions on normal vorticity are derived in the same way the governing equation has been obtained (subtracting the x derivative[1] of the Dirichlet conditions on $(\hat{w},\ \langle \hat{w} \rangle_j)$ from the z derivative of the Dirichlet conditions on $(\hat{u},\ \langle \hat{u} \rangle_j)$)

$$\begin{aligned} \langle \hat{\eta} \rangle_j &= 0 \qquad && \text{on} \quad \Gamma_{wj} \\ \hat{\eta} &= \langle \hat{\eta} \rangle_j \qquad && \text{on} \quad \Gamma_j \end{aligned} \tag{C.5}$$

Since the differential problem for $(\hat{v},\ \langle \hat{v} \rangle_j)$ is fourth order, it is necessary to derive further conditions on $(\hat{v},\ \langle \hat{v} \rangle_j)$. As it is done for plane channel flow, evaluation of the incompressibility constraint on the boundary and the interfaces

$$\begin{aligned} \left(\hat{\boldsymbol{\nabla}} \cdot \langle \hat{\mathbf{u}} \rangle_j \right) \Big|_{\Gamma_{wj}} &= 0 \\ \left(\hat{\boldsymbol{\nabla}} \cdot \langle \hat{\mathbf{u}} \rangle_j \right) \Big|_{\Gamma_j} &= 0 \\ \left(\hat{\boldsymbol{\nabla}} \cdot \hat{\mathbf{u}} \right) \Big|_{\Gamma_j} &= 0 \end{aligned} \tag{C.6}$$

---

[1] Differentiation of the boundary and interface conditions in the x and z directions is a legitimate operation, since these conditions are valid on all the wall-parallel plane and the boundary and interface values are still functions of the x and z coordinates.

combined with the Dirichlet conditions on $(\hat{u},\ \langle\hat{u}\rangle_j)$ and $(\hat{w},\ \langle\hat{w}\rangle_j)$, leads to the Neumann conditions on $(\hat{v},\ \langle\hat{w}\rangle_j)$

$$\begin{aligned} \frac{\partial\langle\hat{v}\rangle_j}{\partial y} &= 0 \qquad \text{on} \quad \Gamma_{wj} \\ \frac{\partial\hat{v}}{\partial y} &= \frac{\partial\langle\hat{v}\rangle_j}{\partial y} \qquad \text{on} \quad \Gamma_j \end{aligned} \tag{C.7}$$

A similar procedure is employed in primitive variables also (see sec. 3.4.4). Exploiting the Neumann conditions, the momentum jump interface conditions are expressed in terms of the normal velocity (summing the x derivative of the condition on $(\hat{u},\ \langle\hat{u}\rangle_j)$ with z derivative of the condition on $(\hat{w},\ \langle\hat{w}\rangle_j)$)

$$\sigma_j\frac{\partial^2\hat{v}}{\partial y^2} - \frac{\sigma_j}{\epsilon_j}\frac{\partial^2\langle\hat{v}\rangle_j}{\partial y^2} = \pm\tau_j\frac{\partial\hat{v}}{\partial y} \tag{C.8}$$

and in terms of the normal vorticity (again, subtracting the x derivative of the condition on $(\hat{w},\ \langle\hat{w}\rangle_j)$ from the z derivative of the condition on $(\hat{u},\ \langle\hat{u}\rangle_j)$)

$$\sigma_j\frac{\partial\hat{\eta}}{\partial y} - \frac{\sigma_j}{\epsilon_j}\frac{\partial\langle\hat{\eta}\rangle_j}{\partial y} = \pm\tau_j\hat{\eta} \tag{C.9}$$

The continuity of pressure at the interfaces is rewritten in normal velocity - normal vorticity variables thanks to the momentum equation. Pressure can be explicitated, in each channel layer, from the sum of the x momentum equation differentiated in x and the z momentum equation differentiated in z. Exploiting the Dirichlet and Neumann conditions on $\hat{v}$, it is possible to derive

$$\begin{aligned} \frac{1}{Re}\frac{\partial^3\hat{v}}{\partial y^3} = \left(\left(\frac{1}{\epsilon_j}-1\right)\left(-\frac{\partial}{\partial t}-\frac{\kappa^2}{Re}\right)-\frac{1}{\sigma_j^2 Re}+i\alpha U(y)\right)\frac{\partial\hat{v}}{\partial y}+ \\ +\frac{1}{\epsilon_j Re}\frac{\partial^3\langle\hat{v}\rangle_j}{\partial y^3}-i\alpha U'(y)\hat{v} \end{aligned} \tag{C.10}$$

Having used the momentum equation in the derivation, this new interface condition is time-varying.

The normal velocity-normal vorticity formulation is often referred as the projection of the Navier-Stokes momentum equation on a divergence-free manifold; to obtain this results, the incompressibility constraint has been explicitly enforced on the boundary of each channel layer in order to derive the Neumann conditions and the time-varying interface conditions.

Because of the presence of mixed derivatives in time and space ($\nabla^2 \frac{\partial}{\partial t}$ in the Orr-Sommerfeld equation and $\frac{\partial^2}{\partial y \partial t}$ in the interface condition derived from pressure continuity), the derivation of the adjoint operator is much more involved than for primitive variables (appendix B). Adjoint equations are easily derived, but integration by parts in time and space brings new time derivatives in the adjoint boundary and interface conditions; continuity of adjoint normal velocity and normal vorticity through interfaces is still required, together with continuity of velocity first derivatives in y and stress jump condition on vorticity, but the stress jump condition on velocity and the unsteady direct interface condition are replaced by adjoint conditions which are much more involved than the direct ones.
Thanks to the much clearer framework provided by direct and adjoint operators in primitive variables, the adjoint normal velocity-normal vorticity operator has not been used in this work.

D

Discretize-then-optimize (discrete adjoint) approach

This appendix presents the most widely used approach to optimization in the engineering community, which is alternative to the *optimize-then-discretize* approach introduced in section 2.1.1 together with overview of the modern approach to the solution of large scale and generalized algebric Riccati equation.

D.1 Derivation of the generalized algebraic Riccati equation

Numerical evaluations of the state (eq. 2.3) and control (eq. 2.4) norms lead to the definition of matrices $\mathbf{Q}$ and $\mathbf{R}$

$$||\mathcal{C}\mathbf{x}||^2_{L^2(\Omega)} = \int_\Omega (\mathcal{C}\mathbf{x})^2 \, \mathrm{d}\Omega \simeq \mathbf{x}^H \mathbf{C}^H \mathbf{M}_\Omega \mathbf{C}\mathbf{x} \equiv \mathbf{x}^H \mathbf{Q}\mathbf{x} \tag{D.1}$$

$$||\mathbf{D}\mathbf{u}||^2_{L^2(\Gamma)} = \int_\Gamma (\mathbf{D}\mathbf{u})^2 \, \mathrm{d}\Gamma \simeq \mathbf{u}^H \mathbf{D}^H \mathbf{M}_\Gamma \mathbf{D}\mathbf{u} \equiv \mathbf{u}^H \mathbf{R}\mathbf{u} \tag{D.2}$$

where M_Ω and M_Γ are integration weight matrices. Hence, the control problem can be expressed as the constrained minimization of the discretized objective functional

$$\mathcal{J} = \frac{1}{2} \int_0^T \left(\mathbf{x}^H \mathbf{Q}\mathbf{x} + \mathbf{u}^H \mathbf{R}\mathbf{u}\right) \mathrm{d}t \tag{D.3}$$

subject to the discretized system equations

$$\mathbf{E}\dot{\mathbf{x}} = \mathbf{A}\mathbf{x} + \mathbf{B}\mathbf{u} \tag{D.4}$$

whose matrices incorporate the boundary conditions in a suitable manner[1]. The Lagrange multiplier $\boldsymbol{\lambda}$ can be used to recast this problem into an unconstrained

---

[1] *Basis recombination* and *boundary bordering* are the most widely used techniques to in-

minimization problem by redefining the objective functional as

$$\mathcal{J} = \frac{1}{2}\int_0^T \left(\mathbf{x}^H\mathbf{Q}\mathbf{x} + \mathbf{u}^H\mathbf{R}\mathbf{u} - \boldsymbol{\lambda}^H\left(\mathbf{E}\dot{\mathbf{x}} - \mathbf{A}\mathbf{x} - \mathbf{B}\mathbf{u}\right)\right) \mathrm{d}t \tag{D.5}$$

Integration by parts in time[2] leads the optimality conditions (Hamiltonian system)

$$\begin{bmatrix}\mathbf{E} & \mathbf{0}\\ \mathbf{0} & \mathbf{E}^H\end{bmatrix}\begin{bmatrix}\dot{\mathbf{x}}\\ \dot{\boldsymbol{\lambda}}\end{bmatrix} = \begin{bmatrix}\mathbf{A} & \mathbf{0}\\ -\mathbf{Q} & -\mathbf{A}^H\end{bmatrix}\begin{bmatrix}\mathbf{x}\\ \boldsymbol{\lambda}\end{bmatrix} + \begin{bmatrix}\mathbf{B}\\ \mathbf{0}\end{bmatrix}\mathbf{u} \tag{D.6}$$

together with the transversality condition

$$\mathbf{R}\mathbf{u} + \mathbf{B}^H\boldsymbol{\lambda} = \mathbf{0} \tag{D.7}$$

A relation between Lagrange multipliers and state vector can be searched in the form [69, 10]

$$\boldsymbol{\lambda} = \mathbf{P}\mathbf{E}\mathbf{x} \tag{D.8}$$

Assuming $\mathbf{R}$ to be invertible, we get the generalized differential Riccati equation

$$-\mathbf{E}^H\dot{\mathbf{P}}\mathbf{E} = \mathbf{E}^H\mathbf{P}\mathbf{A} + \mathbf{A}^H\mathbf{P}\mathbf{E} - \mathbf{E}^H\mathbf{P}\mathbf{B}\mathbf{R}^{-1}\mathbf{B}^H\mathbf{P}\mathbf{E} + \mathbf{Q} \tag{D.9}$$

Letting the time horizon $T \to +\infty$, it can be shown [69] that $\mathbf{P}(t) \to \mathbf{P}$, so we get the generalized algebraic Riccati equation (GARE)

$$\mathbf{E}^H\mathbf{P}\mathbf{A} + \mathbf{A}^H\mathbf{P}\mathbf{E} - \mathbf{E}^H\mathbf{P}\mathbf{B}\mathbf{R}^{-1}\mathbf{B}^H\mathbf{P}\mathbf{E} + \mathbf{Q} = \mathbf{0} \tag{D.10}$$

with the feedback relation

$$\mathbf{u} = -\mathbf{R}^{-1}\mathbf{P}\mathbf{E}\mathbf{x} \equiv \mathbf{K}\mathbf{E}\mathbf{x} \tag{D.11}$$

Solution of this equation poses several difficulties in the case $\mathbf{E}$ is singular [10], while if $\mathbf{E}$ is nonsingular it is possible to *redefine*

$$\begin{aligned}\mathbf{x} &\equiv \mathbf{E}\mathbf{x}\\ \mathbf{A} &\equiv \mathbf{A}\mathbf{E}^{-1}\\ \mathbf{Q} &\equiv \mathbf{E}^{-H}\mathbf{Q}\mathbf{E}^{-1}\end{aligned} \tag{D.12}$$

---

corporate boundary conditions in the numerical discretization of a boundary value problem [18]. The former technique aims to the construction of a set of basis functions which implicitly satisfy boundary conditions, while the latter use a set of basis functions with unprescribed boundary values and incorporates boundary conditions through algebraic equations relating the evaluation of the solution on the boundary nodes (see sec. 3.4).

[2] Integration by parts leads to boundary terms relating the values of $\mathbf{x}$ and $\boldsymbol{\lambda}$ at the initial and final time. Since the boundary terms must vanish (see appendix B and [65]), the direct variable $\mathbf{x}$ is provided with an initial condition and evolves forward in time, while the adjoint variable $\boldsymbol{\lambda}$ is provided with a final condition and evolves backward in time.

to get the classical algebraic Riccati equation (ARE)

$$\mathbf{PA} + \mathbf{A}^H\mathbf{P} - \mathbf{PBR}^{-1}\mathbf{B}^H\mathbf{P} + \mathbf{Q} = \mathbf{0} \tag{D.13}$$

with the feedback relation

$$\mathbf{u} = -\mathbf{R}^{-1}\mathbf{Px} \equiv \mathbf{Kx} \tag{D.14}$$

D.2 Modern approach to the numerical solution of large scale algebraic Riccati equation

Approximation theory for operator Riccati equations arising in continuum systems has been formalized in [57]. Conditions for existence and uniqueness of solutions to the algebraic Riccati equations can be found in [114], while a review of numerical solution methods can be found in [29].

Direct solution methods use eigenvalue (or, more often, Schur [66]) decomposition to build a basis for the stable invariant subspace of the Hamiltonian system, and then assembly matrix $\mathbf{P}$. Iterative (Newton-Kleinman) methods apply Newton method to equation D.13 in order to build a succession of Lyapunov equations which exhibits quadratic convergence.

The Newton-Kleinman method often leads to more accurate results when the system matrices are ill-conditioned. However, the same distinction between direct and iterative methods apply to the numerical solution of the Lyapunov equation needed at each iteration of the Newton-Kleinman method. Direct methods (as the Bartels-Stewart algorithm) are based - again - on the Schur decomposition and may produce inaccurate results when the system matrices are ill-conditioned. Iterative methods for the Lyapunov equation are the Smith method [88] and the more general Alternating Direction Implicit (ADI) methods (see the manual for the MESS library [98]). Their usage in combination with the Newton-Kleinman method for the Riccati equation can be found in [6, 83] and in the MESS (Matrix Equation Sparse Solver) software library for large scale control problems developed at the Max Planck Institute for Dynamics of Complex Technical Systems of Magdeburg [98].

It must be noted that the continuous adjoint approach for nonsingular systems leads to the formulation of a nonsymmetric Riccati equation, whose solution can be attempted by means of a modified Newton-Kleinman method [43] with the numerical solution of a Sylvester equation at each iteration. To the best of our knowledge, this approach has not been tried yet on continuum systems.

D.3 Numerical solution of the generalized algebraic Riccati equation for singular descriptor systems

Many methods of solution of the generalized algebraic Riccati equation for descriptor linear systems are based on the reduction of the dynamical system to normal (state-space) form through algebraic transformations.

A first example can be found in [10], where singular value decomposition (SVD) of matrix $\mathbf{E}$ is used to separate the dynamics of the *slow* subsystem from those of the *fast* subsystem. Under certain conditions [61], an extended control vector can be defined to include the fast subsystem states also, getting a nonsingular generalized algebraic Riccati equation amenable to standard solution techniques [2].

In [32], standard decomposition is used to separate fast and slow subsystems. Gaussian elimination is then used to reduce the system to state-space form, allowing to solve the classical algebraic Riccati equation for the slow subsystem. Due to the numerical issues related to the computation of the standard decomposition form (which needs the computation of a Jordan form), this approach is limited to relatively small systems.

Much work is in progress to develop numerical techniques for the solution of large scale generalized algebraic Riccati equations for singular descriptor systems (mainly, the Navier-stokes momentum and continuity equations for incompressible flow); the reader is referred, for example, to the recent works of Bänsch and Benner [7], and Heiland [49].

Ringraziamenti

Questo lavoro è il frutto di un anno di lavoro solitario, spinto dalla voglia di imparare e di capire. Capire perché le cose funzionano; ancora di più, perché *non* funzionano. Se questo lavoro è giunto ad un termine, è grazie alla curiosità ed alla necessità di documentare, di far sì che l'esperienza non vada persa senza che possa essere d'aiuto a qualcuno.

Prima, un po' di ringraziamenti legati alla realizzazione di questo lavoro. Ringrazio il professor Quadrio ed il professor Cortelezzi per avermi dato l'opportunità di lavorare su questi argomenti. Grazie al professor Mantegazza per la collaborazione e le proficue conversazioni di dinamica, oltre che per la serietà e la passione che è in grado di trasmettere. Un ringraziamento speciale va a Marco Carini per il supporto, l'attenzione, la professionalità e la capacità di ascolto. Grazie ai professori Quaranta, Pralits ed Auteri per la cordialità e gli scambi di idee.

Grazie a Cristian, che dicendomi: "Ragioni da informatico, non da matematico" ha liberato un po' di idee bloccate nella mia mente; a Jack per le conversazioni in sala calcolo, in stazione, in treno e dal finestrino del treno; lavorare con te è stato un piacere. A Marta, per l'ascolto, il supporto, e perché questa tesi ha visto una fine grazie a te. Grazie a Davide, Martina e Codri per i suggerimenti sulla porosità e sui codici sorgenti, e a Marco per avermi permesso di utilizzare il suo programma.

Un ringraziamento infinito al personale della biblioteca del Dipartimento di Scienze e Tecnologie Aerospaziali, per la cordialità, la professionalità e l'efficienza sempre dimostrata. Per quanto sia facile fare ricerca nel 2013, con università e riviste a portata di clic, questo lavoro non sarebbe mai stato realizzabile senza la possibilità di reperire gli articoli più disparati e libri da biblioteche straniere fornitami dal servizio bibliotecario. La soluzione ai problemi di questa tesi è stata possibile solo grazie all'enorme mole di risorse che ho potuto consultare, leggere e confrontare con scopi diversi da quelli per cui erano state scritte.

E ora, viene il difficile. Grazie a chi conosco da sempre, che mi ha cresciuto e

che mi vorrà sempre bene. Grazie a chi, costruendosi tavole da skimboard nel forno della cucina, mi ha insegnato l'arte di arrangiarsi nel seguire i propri sogni. A chi mi parla di Navier-Stokes anche ad orari poco raccomandabili, ma emana sempre una passione profonda per ciò che fa. Alla ragazza più forte e determinata che conosca, *heel hartelijk bedankt*! Grazie, infine, alla saggezza inconsapevole di tutti i miei amici.

Aprile 2014
Luca Cirrottola

Bibliography

[1] L. Amodei and J.-M. Buchot. “A stabilization algorithm of the Navier-Stokes equations based on algebraic Bernoulli equation”. In: *Numerical Linear Algebra with Applications* 19 (2012), pp. 700–727 (cit. on p. 25).

[2] W. F. Arnold and A. J. Laub. “Generalized eigenproblem algorithms and software for algebraic Riccati equations”. In: *Proceedings of the IEEE*. Vol. 72. 2. 1984 (cit. on p. 116).

[3] A. Asan, B. Foss, and S. Sagatun. “Flow control of fluids through porous media”. In: *Applied Mathematics and Computation* 219 (2012), pp. 3323–3335 (cit. on p. 7).

[4] U. M. Ascher and L. R. Petzold. *Computer Methods for Ordinary Differential Equations and Differential-Algebraic Equations*. Society for Industrial and Applied Mathematics, 1998 (cit. on pp. 34, 45, 51).

[5] M. A. Dahleh B. Bamieh F. Paganini. “Distributed Control of Spatially Invariant Systems”. In: *IEEE Transactions on Automatic Control* 47 (2002) (cit. on pp. 4, 21, 72).

[6] H. T. Banks and K. Ito. “A Numerical Algorithm for Optimal Feedback Gains in High Dimensional Linear Quadratic Regulator Problems”. In: *SIAM Journal on Control and Optimization* 29.3 (1991), pp. 499–515 (cit. on p. 115).

[7] E. Bänsh and P. Benner. “Stabilization of incompressible flow problem by Riccati-based feedback”. In: *Constrained Optimization and Optimal Control for Partial Differential Equations International Series of Numerical Mathematics*. 2012, pp. 5–20 (cit. on p. 116).

[8] J. B. Barlow, W. H. Rae, and A. Pope. *Low-speed wind tunnel testing*. Wiley, 1999 (cit. on p. 7).

[9] G. S. Beavers and D. D. Joseph. “Boundary conditions at a naturally permeable wall”. In: *Journal of Fluid Mechanics* 30 (1967), pp. 197–207 (cit. on p. 11).

[10] D. J. Bender and A. J. Laub. “The Linear-Quadratic Optimal Regulator for Descriptor Systems”. In: *IEEE Transactions n Automatic Control* 8 (1987), pp. 672–688 (cit. on pp. 37, 114, 116).

[11] T. R. Bewley. “Linear control and estimation of nonlinear chaotic convection: Harnessing the butterfly effect”. In: *Physics of Fluids* 11 (1999), pp. 1169–1186 (cit. on p. 15).

[12] T. R. Bewley. “Flow control: new challenges for a new Renaissance”. In: *Progress in Aerospace Sciences* 37 (2001), pp. 21–58 (cit. on pp. 4, 8, 21).

[13] T. R. Bewley. “A fundamental limit on the balance of power in a transpiration-controlled channel flow”. In: *Journal of Fluid Mechanics* 632 (2009), pp. 443–446 (cit. on p. 6).

[14] T. R. Bewley and S. Liu. “Optimal and robust control and estimation of linear paths to transition”. In: *Journal of Fluid Mechanics* 365 (1998), pp. 305–349 (cit. on pp. 5, 19, 77).

[15] T. R. Bewley, P. Moin, and R. Temam. “DNS-based predictive control of turbulence: an optimal benchmark for feedback algorithms”. In: *Journal of Fluid Mechanics* 447 (2001), pp. 179–225 (cit. on p. 6).

[16] T. R. Bewley, J. O. Pralits, and P. Luchini. “Minimal-energy control feedback for stabilization of bluff-body wakes based on unstable open-loop eigenvalues and left eigenvectors”. In: *5th Conference on Bluff Body Wakes and Vortex-Induced Vibrations (BBVIV-5)*. Bahia, Brazil, 2007 (cit. on pp. viii, 25, 26, 95).

[17] G. Bornia. “Analysis of Optimal Control Problems for the Incompressible MHD Equations and Implementation in a Finite Element Multiphysics Code”. PhD thesis. Università di Bologna, 2012 (cit. on p. 17).

[18] J. P. Boyd. *Chebyshev and Fourier Spectral Methods*. Dover Publications, 2000 (cit. on pp. 34–39, 41, 45, 99, 101, 114).

[19] G. A. Brès, T. Colonius, and A. V. Fedorov. “Acoustic Properties of Porous Coatings for Hypersonic Boundary-Layer Control”. In: *AIAA Journal* 48 (2 2010), pp. 267–274 (cit. on p. 7).

[20] R. H. Cannon. *Dynamics of Physical Systems*. Dover, 1967 (cit. on p. 16).

[21] C. Canuto and G. Sacchi Landriani. “Analysis of the Kleiser-Schumann method”. In: *Numerische Mathematik* 50 (1986), pp. 217–243 (cit. on p. 46).

[22] C. Canuto et al. *Spectral Methods: Fundamentals in Single Domains*. Springer, 2006 (cit. on pp. 36, 99, 101).

[23] C. Canuto et al. *Spectral Methods: Evolution to Complex Geometries and Applications to Fluid Dynamics*. Springer, 2007 (cit. on pp. 34, 38, 41, 45–47, 99).

[24] M. Carini, J. O. Pralits, and P. Luchini. “Feedback control of vortex shedding using a full-order optimal compensator”. Submitted to Fluids and Structures. 2013 (cit. on p. 25).

[25] D. Cavaglieri. “Optimal Feedback Control of Turbulent Channel Flow through Wall-Based Sensors and Actuators”. MSc thesis (cit. on pp. 6, 78, 102).

[26] H. Choi, P. Moin, and J. Kim. “Active turbulence control for drag reduction in wall-bounded flows”. In: *Journal of Fluid Mechanics* 262 (1994), pp. 75–110 (cit. on pp. 6, 7).

[27] L. Cortelezzi and J. L. Speyer. “Robust reduced-order controller of laminar boundary layer transitions”. In: *Physical Review E* 58 (1998) (cit. on p. 5).

[28] H. Darcy. *Les Fountaines Publiques de la Ville de Dijon*. Ed. by Dalmont. Paris, 1856 (cit. on p. 9).

[29] B. N. Datta. *Numerical Methods for Linear Control Systems*. Elsevier, 2004 (cit. on p. 115).

[30] P. T. Dawkins, S. R. Dunbar, and R. W. Douglass. “The origin and nature of spurious eigenvalues in the spectral tau method”. In: *Journal of Computational Physics* 147 (1998), pp. 441–462 (cit. on p. 39).

[31] J. J. Dongarra, B. Straughan, and D. W. Walker. “Chebyshev Tau - QZ Algorithm Methods for Calculating Spectra of Hydrodynamic Stability Problems”. In: *Applied Numerical Mathematics* 22 (1996), pp. 399–434 (cit. on pp. 38, 39, 46).

[32] G.-R. Duan. *Analysis and Design of Descriptor Linear Systems*. Springer, 2009 (cit. on pp. 16, 38, 66, 116).

[33] M. Gad el Hak. *Flow Management - Passive, Active and Reactive Flow Management*. Cambridge University Press, 2000 (cit. on p. 1).

[34] P. W. Fick, E. H. van Brummelen, and K. G. van der Zee. “On the adjoint-consistent formulation of interface conditions in goal-oriented error estimation and adaptivity for fluid-structure interaction”. In: *Computer Methods in Applied Mechanics and Engineering* 199 (2010), pp. 3369–3385 (cit. on pp. 22, 24).

[35] B. Friedland. *Control System Design*. Dover Publications, 2005 (cit. on pp. 4, 15, 25).

[36] B. Frohnapfel et al. “Interpretation of the mechanism associated with turbulent drag reduction in terms of anisotropy invariants”. In: *Journal of Fluid Mechanics* 577 (2007), pp. 457–466 (cit. on p. 7).

[37] Q. Gallas et al. “Low dimensional modeling of zero-net mass-flux actuators”. In: *2nd AIAA Flow Control Conference*. 2004 (cit. on p. 8).

[38] R. Garcia-Mayoral and J. Jiménez. “Drag reduction by riblets”. In: *Phylosophical Transactions of the Royal Society* 177 (2011), pp. 133–166 (cit. on p. 3).

[39] M. B. Giles and N. A. Pierce. “Adjoint equations in CFD: Duality, boundary conditions and solution behaviour”. In: (1997). AIAA Paper 97-1850 (cit. on p. 105).

[40] M. B. Giles and N. A. Pierce. “An introduction to the adjoint approach to design”. In: *Flow, Turbulence and Combustion* 65 (2000), pp. 393–415 (cit. on pp. 22, 105).

[41] D. R. Graham and J. J. L. Higdon. “Oscillatory forcing of flow through porous media. Part 1. Steady flow”. In: *Journal of Fluid Mechanics* 465 (2002), pp. 213–235 (cit. on p. 8).

[42] D. R. Graham and J. J. L. Higdon. “Oscillatory forcing of flow through porous media. Part 2. Unsteady flow”. In: *Journal of Fluid Mechanics* 465 (2002), pp. 237–260 (cit. on p. 8).

[43] C.-H. Guo and N. Higham. “Iterative solution of a nonsymmetric algebraic Riccati equation”. In: *SIAM Journal on Matrix Analysis and Applications* 29.2 (2007), pp. 396–412 (cit. on pp. 97, 115).

[44] J. Hagan and J. Priede. “Capacitance matrix technique for avoiding spurious eigenmodes in the solution of hydrodynamic stability problems by Chebyshev collocation method”. In: (2012). arXiv:1207.0388 [physics.comp-ph] (cit. on p. 47).

[45] A. Hanifi, P. J. Schmid, and D. S. Henningson. "Transient growth in compressible boundary layer flow". In: *Physics of Fluids* 8 (1996), pp. 826–837 (cit. on p. 102).

[46] R. Hartmann. "Derivation of an adjoint consistent discontinuous Galerkin discretization of the compressible Euler equations". In: *International Conference on Boundary and Interior Layers*. Ed. by G. Lube and G. Rapin. 2006 (cit. on p. 22).

[47] R. Hartmann. "Adjoint consistency analysis of discontinuous Galerkin discretizations". In: *SIAM Journal on Numerical Analysis* 45 (2007), pp. 2671–2696 (cit. on p. 22).

[48] R. Hartmann. "Error estimation and adjoint based refinement for an adjoint consistent DG discretization of the compressible Euler equations". In: *International Journal of Computing Science and Mathematics* 1 (2007), pp. 207–220 (cit. on p. 22).

[49] J. Heiland. "Optimal control of linearized Navier-Stokes equations via a differential-algebraic Riccati decoupling". In: *Numerical Analysis and Scientific Computation with Applications*. Calais, 2013 (cit. on pp. 25, 116).

[50] J. Heiland and V. Mehrmann. "Numerical methods for PDAE constraint optimal control". In: *Jahrestagung der GAMM*. Darmstadt, 2012. URL: `http://janheiland.de/files/talks/gamm2012Heiland.pdf` (cit. on p. 25).

[51] J. E. Hicken and D. W. Zingg. "Dual consistency and functional accuracy: a finite-differenc perspective". Preprint submitted to Elsevier (cit. on p. 22).

[52] J. E. Hicken and D. W. Zingg. "The role of dual consistency in functional accuracy: Error estimation and superconvergence". In: *20th AIAA Computational Fluid Dynamics Conference*. Honolulu, Hawaii, 2011 (cit. on p. 22).

[53] M. Högberg and T. R. Bewley. "Spatially localized convolution kernels for feedback control of transitional flows". In: *39th IEEE Conference on Decision and Control*. Sidney, Australia, 2000 (cit. on p. 5).

[54] M. Högberg, T. R. Bewley, and D. S. Henningson. "Linear feedback control and estimation of transition in plane channel flow". In: *Journal of Fluid Mechanics* 481 (2003), pp. 149–175 (cit. on pp. 5, 6, 15, 21).

[55] M. Högberg, T. R. Bewley, and D. S. Henningson. “Relaminarization of $Re_\tau = 100$ turbulence using gain scheduling and linear state-feedback control”. In: *Physics of Fluids* 15 (2003), pp. 3572–3575 (cit. on pp. 6, 7).

[56] W. Huang and D. M. Sloan. “The Pseudospectral Method for Solving Differential Eigenvalue Problems”. In: *Journal of Computational Physics* 111 (1994), pp. 399–409 (cit. on pp. 38, 45).

[57] K. Ito and K. A. Morris. “An approximation theory of solutions to operator Riccati equations for H^∞ control”. In: *SIAM Journal on Control and Optimization* 36.1 (1998), pp. 82–99 (cit. on p. 115).

[58] R. D. Joslin. “Aircraft laminar flow control”. In: *Annual Review of Fluid Mechanics* 30 (1998), pp. 1–29 (cit. on p. 7).

[59] A. Karageorghis. “On the equivalence between basis recombination and boundary bordering formulations for spectral collocation methods in rectangular domains”. In: *Mathematics and Computers in Simulation* 35.6 (1993), pp. 513–524 (cit. on p. 36).

[60] N. Kasagi, Y. Suzuki, and K. Fukagata. “Microelectromechanical systems-based feedback control of turbulence for skin friction reduction”. In: *Annual Review of Fluid Mechanics* 41.231-251 (2009) (cit. on pp. 4, 96).

[61] A. Kawamoto, K. Takaba, and T. Katayama. “On the generalized algebraic Riccati equation for continuous-time descriptor systems”. In: *Linear Algebra and its Applications* 296 (1999), pp. 1–14 (cit. on p. 116).

[62] J. Kim and T. R. Bewley. “A linear systems approach to flow control”. In: *Annual Review of Fluid Mechanics* 39 (2007), pp. 383–417 (cit. on pp. 4, 5, 95).

[63] J. Kim and J. Lim. “A linear process in wall-bounded turbulent shear flows”. In: *Physics of Fluids* 12 (2000), pp. 1885–1888 (cit. on p. 6).

[64] J. Kim, P. Moin, and R. Moser. “Turbulence statistics in fully developed channel flow at low Reynolds number”. In: *Journal of Fluid Mechanics* 177 (1987), pp. 133–166 (cit. on p. 46).

[65] C. Lanczos. *Linear Differential Operators*. Martino Publishing, 2012 (cit. on pp. 16, 19, 105, 114).

[66] A. J. Laub. “A Schur method for solving algebraic Riccati equations”. In: *IEEE Transactions on Automatic Control* 24.6 (1979) (cit. on p. 115).

[67] R. Lehoucq et al. *ARPACK (ARnoldi PACKage)*. URL: `http://www.caam.rice.edu/software/ARPACK/` (cit. on p. 52).

[68] S. Li and L. Petzold. “Adjoint sensitivity analysis for time-dependent partial differential equations with adaptive mesh refinement”. In: *Journal of Computational Physics* 198 (2004), pp. 310–325 (cit. on pp. 22, 23, 41).

[69] J. L. Lions. *Optimal Control of Systems Governed by Partial Differential Equations*. Springer-Verlag, 1971 (cit. on pp. 15, 114).

[70] Q. Liu and A. Prosperetti. “Pressure-driven flow in a channel with porous walls”. In: *Journal of Fluid Mechanics* 679 (2011), pp. 77–100 (cit. on p. 8).

[71] J. C.-C. Lu. “An a posteriori error control framework for adaptive precision optimization using discontinuous Galerkin finite element method”. PhD thesis. Massachusetts Institute of Technology, 2005 (cit. on p. 22).

[72] P. Luchini and A. Bottaro. “Adjoint equations in stability analysis”. In: *Annual Review of Fluid Mechanics* 46 (2014) (cit. on p. 105).

[73] P. Luchini and M. Quadrio. “A low-cost parallel implementation of direct numerical simulation of wall turbulence”. In: *Journal of Computational Physics* 211 (2006), pp. 551–571 (cit. on pp. 54, 55, 73).

[74] S. V. Lukashevich et al. “Stabilization of High-Speed Boundary Layer Using Porous Coatings of Various Thicknesses”. In: *AIAA Journal* 50 (2012), pp. 1897–1904 (cit. on p. 7).

[75] M. L. Manning, B. Bamieh, and J. M. Carlson. “Descriptor approach for eliminating spurious eigenvalues in hydrodynamic equations”. In: (2007). Preprint submitted to Elsevier, arXiv:0705.1542 [physics.comp-ph] (cit. on p. 38).

[76] P. Mantegazza and P. Masarati. *Analysis of Systems of Differential-Algebraic Equations (DAE)*. 2012. URL: `http://www.aero.polimi.it/~masarati/mb/mb-dae-en.pdf` (cit. on pp. 48, 51).

[77] F. Martinelli. “Feedback Control of Turbulent Wall Flows”. PhD thesis (cit. on pp. 7, 15, 78).

[78] F. Martinelli, M. Quadrio, and P. Luchini. “Active control and drag reduction in turbulent wall flows”. In: *Convegno Calcolo ad Alte Prestazioni*. Milano, 2007 (cit. on p. 7).

[79] G. B. McFadden, B. T. Murray, and R. F. Boisvert. “Elimination of Spurious Eigenvalues in the Chebyshev Tau Spectral Methods”. In: *Journal of Computational Physics* 91 (1990), pp. 228–239 (cit. on pp. 38, 41).

[80] J. McKernan. “Control of Plane Poiseuille Flow: A Theorethical and Computational Investigation”. PhD thesis. Cranfield University, 2006 (cit. on p. 45).

[81] T. Min et al. “Sustained sub-laminar drag in a fully developed channel flow”. In: *Journal of Fluid Mechanics* 558 (2006), pp. 309–318 (cit. on p. 6).

[82] K. Morris. *Control of Systems Governed by Partial Differential Equations*. URL: `http://www.math.uwaterloo.ca/~kmorris/Preprints/Morris_controlhandbook.pdf` (cit. on pp. 15, 17).

[83] K. Morris and C. Nevasca. *Iterative Solution of Algebraic Riccati Equations using a Modified Newton-Kleinman Method*. 2004. URL: `ftp://ftp.math.ucla.edu/pub/camreport/cam05-15.pdf` (cit. on p. 115).

[84] J. A. Ochoa-Tapia and S. Whitaker. “Momentum transfer at the boundary between a porous medium and a homogeneous fluid I. Theoretical development”. In: *International Journal of Heat and Mass Transfer* 38 (1995), pp. 2635–2646 (cit. on pp. 10, 11, 95).

[85] J. A. Ochoa-Tapia and S. Whitaker. “Momentum transfer at the boundary between a porous medium and a homogeneous fluid II. Comparison with experiment”. In: *International Journal of Heat and Mass Transfer* 38 (1995), pp. 2647–2655 (cit. on pp. 10, 11).

[86] J. A. Ochoa-Tapia and S. Whitaker. “Momentum jump condition at a boundary between a porous medium and a homogeneous fluid: Inertial effects”. In: *Journal of Porous Media* 1 (1998), pp. 201–217 (cit. on pp. 10, 11).

[87] S. A. Orszag. “Accurate solution of the Orr-Sommerfeld stability equation”. In: *Journal of Fluid Mechanics* 50 (1971), pp. 689–709 (cit. on pp. 38, 40, 100).

[88] T. Penzl. “A cyclic low rank Smith method for large sparse Lyapunov equations with applications in model reduction and optimal control”. In: *SIAM Journal on Scientific Computing* 21.4 (1999) (cit. on p. 115).

[89] S. B. Pope. *Turbulent Flows*. Cambridge University Press, 2000 (cit. on p. 9).

[90] J. O. Pralits and P. Luchini. “Riccati-less optimal control of bluff-body wakes”. In: *Seventh IUTAM Symposium on Laminar-Turbulent Transition*. Vol. 18. Springer, 2010 (cit. on pp. viii, 27, 29).

[91] W. H. Press et al. *Numerical Recipes: The Art of Scientific Computing*. Cambridge University Press, 2007 (cit. on p. 54).

[92] J. Priede, S. Aleksandrova, and S. Molokov. “Linear stability of Hunt’s flow”. In: *Journal of Fluid Mechanics* 649.115-134 (2010) (cit. on p. 47).

[93] M. Quadrio, P. Ricco, and C. Viotti. “Streamwise-traveling waves of spanwise wall velocity for turbulent drag reduction”. In: *Journal of Fluid Mechanics* 177 (2009), pp. 133–166 (cit. on p. 3).

[94] L. Quartapelle. *Numerical Solution of the Incompressible Navier-Stokes Equations*. Birkhauser, 1993 (cit. on pp. 39, 46, 96).

[95] A. Quarteroni, R. Sacco, and F. Saleri. *Matematica numerica*. Springer, 2008 (cit. on p. 51).

[96] R. Raju et al. “Simple models of zero-net mass-flux jets for flow control simulations”. In: *International Journal of Flow Control* 1.3 (2009), pp. 179–198 (cit. on p. 8).

[97] M. Rosti. “Direct Numerical Simulation of Turbulent Channel Flow over Porous Walls”. MSc thesis (cit. on pp. 11, 12, 54, 73, 95).

[98] J. Saak, H. Mena, and P. Benner. *MESS (Matrix Equations Sparse Solver*. URL: `http://www2.mpi-magdeburg.mpg.de/mpcsc/software/mess.php` (cit. on pp. 97, 115).

[99] S. Salsa. *Partial Differential Equations in Action - From Modelling to Theory*. Springer, 2009 (cit. on p. 16).

[100] D. Scarselli. “Non-Modal Stability of Laminar Channel Flow over Porous Walls”. MSc thesis (cit. on pp. 11, 12, 39, 41, 95, 100).

[101] P. J. Schmid and D. S. Henningson. *Stability and Transition in Shear Flows*. Springer, 2000 (cit. on pp. 26, 35, 37, 39–41, 57, 72, 100).

[102] A. Sei and W. Symes. *A note on consistency and adjointness for numerical schemes*. Tech. rep. 1995 (cit. on p. 22).

[103] O. Semeraro et al. “Riccati-less approach for optimal control and estimation: an application to two-dimensional boundary layers”. In: *Journal of Fluid Mechanics* 731 (2013), pp. 394–417 (cit. on pp. 27, 29, 77, 95).

[104] A. N. Shiplyuk et al. “Effect of Porous Coatings on Stability of Hypersonic Boundary Layers”. In: *Journal of Applied Mechanics and Technical Physics* 45 (2 2004), pp. 286–291 (cit. on p. 7).

[105] Z. Sirkes and E. Tziperman. “Finite difference of adjoint or adjoint of finite difference?” In: *Monthly Weather Review* 125 (1997), pp. 3373–3378 (cit. on p. 22).

[106] S. Skogestad and I. Postlethwaite. *Multivariable Feedback Control*. Wiley, 2005 (cit. on pp. 4, 6, 64, 89).

[107] N. Tilton and L. Cortelezzi. “Linear stability analysis of pressure-driven flows in channels with porous walls”. In: *Journal of Fluid Mechanics* 604 (2008), pp. 411–445 (cit. on pp. 10–12, 33, 39, 41, 44, 57, 58, 65, 67–70, 95, 100).

[108] L. N. Trefethen et al. “Hydrodynamic stability without eigenvalues”. In: *Science* 261 (1993), pp. 578–584 (cit. on p. 6).

[109] M. S. Triantafyllou and F. S. Hover. *Maneuvering and Control of Marine Vehicles*. 2003. URL: `http://ocw.mit.edu/courses/mechanical-engineering/2-154-maneuvering-and-control-of-surface-and-underwater-vehicles-13-49-fall-2004/lecture-notes/` (cit. on p. 89).

[110] J. A. C. Weidermann and S. C. Reddy. “A Matlab Differentiation Matrix Suite”. In: *ACM Transactions on Mathematical Software* 26 (2000) (cit. on p. 45).

[111] S. Whitaker. “The Forchheimer equation: A theoretical development”. In: *Transport in porous media* 25 (1996), pp. 27–61 (cit. on pp. 9, 10).

[112] T. Yoshino, Y. Suzuki, and N. Kasagi. “Drag reduction of turbulence air channel flow with distributed micro sensors and actuators”. In: *Journal of Fluid Science and Technology* 3.1 (2008), pp. 137–148 (cit. on p. 96).

[113] Q. Zhang and A. Prosperetti. “Pressure-driven flow in two-dimensional channel with porous walls”. In: *Journal of Fluid Mechanics* 631 (2009), pp. 1–21 (cit. on p. 8).

[114] K. Zhou, J. C. Doyle, and K. Glover. *Robust and Optimal Control*. Prentice-Hall, 1996 (cit. on pp. 4, 115).